Mechanical Controls on Eruptions

by

Maxwell Lutman Rudolph

A dissertation submitted in partial satisfaction of the
requirements for the degree of
Doctor of Philosophy

in

Earth and Planetary Science

in the

Graduate Division

of the

University of California, Berkeley

Committee in charge:

Professor Michael Manga, Chair
Professor Chi-Yuen Wang
Associate Professor Jon Wilkening

Fall 2012

Mechanical Controls on Eruptions

Abstract

Mechanical Controls on Eruptions

by

Maxwell Lutman Rudolph

Doctor of Philosophy in Earth and Planetary Science

University of California, Berkeley

Professor Michael Manga, Chair

Processes that transport heat and mass govern the long-term evolution of planets and are responsible for surface geological features. This dissertation addresses the thermal and mechanical evolution of icy bodies and the mechanics of geyser and mud volcano eruptions.

Some surface features on Europa have been interpreted as cryovolcanic deposits, but conduits are required in order for water to erupt from a subsurface ocean. Results from a model of fracture penetration indicate that it is unlikely that downward propagating fractures can reach a subsurface ocean on Europa, but that Enceladus' ice shell may be completely cracked. The mechanics of ice shell fracture depend on the stress state in the ice shell, which in turn depends on the thermal history due to coupling between ocean pressure, ice shell thickening, and stresses in the overlying ice shell. Numerical calculations that account for the development of Crystallographic Preferred Orientation (CPO) in ice indicate that CPO-induced viscous anisotropy has first order effects on convective velocity and heat transport, but that the thickness of the stagnant lid precludes remote detection of CPO under conditions relevant to the Galilean Satellites.

Mud volcanoes near the Salton Sea, Southern California responded to the April, 2010 El Mayor-Cucapah earthquake and another smaller event. Analysis of the frequency and amplitude of shaking experienced during events that triggered eruptions as well as several events that did not trigger eruptions reveals that the triggering process is frequency dependent. The Lusi mud eruption in East Java, Indonesia provides an unprecedented opportunity to study a large mud eruption from start to end. An analysis of ground deformation during the first five years of Lusi's eruption indicates that progressive mobilization of mud occurred, supporting a new conceptual model for mud volcanism that is in some ways analogous to large caldera-forming silicic volcanic eruptions. Like mud volcanoes, geysers provide an opportunity to study an erupting system analogous to volcanoes. Ground deformation at Calistoga Geyser is cyclic and reflects the filling and draining of the geyser's plumbing system.

Contents

List of Figures

List of Tables

Acknowledgments

Completing a PhD is not entirely a solo undertaking and I have many people to thank for helping me along the way. Foremost, I thank Michael Manga for giving me the opportunity to come to Berkeley and join his group, for teaching me what research is, and for setting by example a high standard for scientific output and professionalism.

My parents Sarah and Rob and grandfather Byron have been supported me in everything that I've decided to do in life, academically and otherwise.

I would not have pursued graduate studies without the encouragement of my undergraduate advisers in physics and geology, Dan Stinebring and Bruce Simonson. In particular, Bruce lent me a copy of Richard Greenberg's *Europa - The Ocean Moon*, which was my introduction to the scientific study of icy moons. Dave Yuen gave me the opportunity as a freshman undergraduate to try my hand at research, as well as the opportunity to present my work at the 2003 AGU Fall meeting, and provided constant encouragement along the way.

Thanks are also due to the other students and postdocs in the Manga group, especially Alyssa, Chris, Edwin, Leif, Jim, Peter, and Tim, for engaging discussions and fruitful collaborations. I also thank my collaborators on the work presented in this thesis: Yo Fukushima, Shaul Hurwitz, Malcolm Johnston, Leif Karlstrom, Michael Manga, Manoochehr Shirzaei, and Chi Wang.

Part of my graduate education was supported in part by the Berkeley Fellowship for Graduate Study and a National Science Foundation Graduate Research Fellowship, which gave me the freedom to work on problems of my own choosing and provided the computational resources necessary for Chapter 3 of this thesis.

Chapter 1

Introduction

Processes involving heat and mass transport govern the differentiation and long-term evolution of planetary bodies, shaping their surfaces, delivering the chemical constituents of their atmospheres and oceans to their surfaces, and shaping the planetary surfaces that we explore in the field or observe remotely. In this thesis, I study processes of heat and mass transport in icy moons and in terrestrial geysers and mud volcanoes.

The icy moons of Saturn and Jupiter have attracted the attention of geophysicists because their surface features reveal past and ongoing geologic activity, because processes analogous to terrestrial volcanism and silicate mantle convection may occur, and because some moons have liquid water oceans in contact with silicate interiors, providing some of the essential ingredients thought to be necessary for life (e.g. *Chyba and Phillips*, 2001). Europa in particular has attracted considerable attention because of its relatively young surface age of 40-90 Ma (*Bierhaus et al.*, 2009), and liquid water ocean. However, in order to unravel Europa's geologic past we need to understand the geologic processes that form Europa's dominant surface features, broadly classified as linae, line-like structures including double-ridges, crack like features, and bands. Among linae, double-ridges are abundant and several models have been proposed to explain the formation of these features, some of which require propagating a crack through the ice shell to the subsurface ocean. Other surface features on Europa have been interpreted as cryovolcanic deposits (*Fagents*, 2003), the eruption of which requires a pathway from a subsurface reservoir to the surface.

In Chapter 2, I calculate the depth to which downward-propagating fractures can penetrate in a planetary ice shell. Fractures are unlikely to initiate from the base of a planetary ice shell because viscous relaxation of stresses is rapid in the warm ice deep within the ice shell. The results of Chapter 2 are applied to both Europa and Enceladus, concluding that for reasonable estimates of ice shell thickness, Europa's ice shell can not be penetrated by downward-penetrating cracks whereas cracks on Enceladus may reach a subsurface ocean. This result is in agreement with the observation of a South Polar eruption on Enceladus (*Porco et al.*, 2006) that may be sustained by a liquid water ocean (*Postberg et al.*, 2009). Europa's surface is tectonically young, but it is unknown whether Europa is at present tectonically active. We explore the idea that deep fractures in a planetary ice shell may emit detectable amounts of infrared radiation and provide limits on detectability by an hypothetical Europa orbiter. The work related to fracture penetration presented in Chapter 2 was published in the journal *Icarus* (*Rudolph and Manga*, 2009b).

Planetary ice shells may convect under some conditions, and the occurrence of convection is important because it affects the long-term thermal evolution of an icy body, including the stability of a subsurface ocean, because convection may produce some of the surface features observed on icy moons (as it does on Earth), and because convection provides a mechanism for mass transport between a subsurface ocean and the surface, with implications for astrobiology. Past studies of convection in icy mantles have focused on long-term thermal evolution, the effects of changes in grain size (which in turn affect the effective viscosity of ice deforming by diffusion creep), and on the amount and distribution of internal heating by tidal dissipation. In Chapter 3, I consider for the first time the effect of development of Crystallographic Preferred Orientation (CPO) in ice. CPO develops when ice deformation

is accommodated by dislocation creep, and results in macroscopically anisotropic viscosity and dielectric properties, with potential implications for surface features and electromagnetic observations (*Barr and Stillman*, 2011). The work presented in Chapter 3 is currently under review in *Journal of Geophysical Research - Planets*.

Earthquakes can induce geologic processes including other earthquakes (*Hill et al.*, 1993), rockfall and landslides (e.g. *Keeper*, 1984; *Plafker et al.*, 1971), and volcanic eruptions (*Manga and Brodsky*, 2006), as well as a variety of hydrological phenomena including liquefaction (*Lee and Seed*, 1967; *Holzer et al.*, 1989), water level changes in wells, changes in stream flow (*Muir-Wood and King*, 1993), geyser eruptions (*Silver and Valette-Silver*, 1992), and mud volcano eruptions (*Mellors et al.*, 2007). Although mud volcano responses to earthquakes have been documented as early as 79 A.D. (in Pliny the Elder's *Naturalis Historæ*), the mechanism(s) by which responses occur are not well understood. In Chapters 4-5, I document multiple responses and non-responses of a group of mud volcanoes near the Salton Sea, Southern California to several earthquakes. In Chapter 4, I rule out an hypothesis that seismic waves mobilize bubbles trapped *by the rheological properties of mud* by combining field observations of gas discharge and eruptive activity with laboratory rheological measurements and an analytical treatment of bubble ascent in mud volcano systems. In Chapter 5, I argue that mud volcanoes respond more readily to seismic waves of lower frequency and that this observation is consistent with the mobilization of bubbles trapped *by constrictions* in water-saturated porous media. The work presented in Chapters 4-5 was published in *Journal of Geophysical Research - Solid Earth* and *Geophysical Research Letters* (*Rudolph and Manga*, 2010, 2012).

Mud volcanoes are geologically important because they play an important role in the transport of sediment and fluids in accretionary wedge settings and because they are analogous in many ways to magmatic systems (*Kopf*, 2002). Mud volcanism or mud eruption can also have significant socioeconomic consequences, as demonstrated by the ongoing eruption of Lusi, a large mud eruption in East Java, Indonesia that began on May 29, 2006. Chapters 6-7 focus on two questions related to Lusi 1) what processes control the mobilization and transport of material to the surface and 2) how long is this eruption likely to continue? In Chapter 6, I develop a new mechanical model for mud volcanism in which the eruption is driven by a combination of overpressure and gas expansion and pressure in a mud reservoir at depth is buffered by progressive mobilization. The process of progressive mobilization is of interest because it redefines the mud source region based on a rheological transition from a solid to a fluid, a process that may be analogous to syn-eruptive mobilization of crystal-rich magmas in large silicic caldera-forming eruptions (*Karlstrom et al.*, 2012). Using all available geologic constraints, I use the Monte Carlo approach to predict the eruption's longevity. In Chapter 7, I revise the predictions made in Chapter 6 by incorporating new observations of ground deformation derived from synthetic aperture radar observations. Ground deformation indicates that the eruption is coming to an end much more quickly than previously anticipated. The work presented in Chapter 6 was published in *Earth and Planetary Science Letters* (*Rudolph et al.*, 2011) and the work presented in Chapter 7 is currently under review in *Nature*.

In Chapter 7, I showed that ground deformation can be used to study the source processes in mud volcano systems. Like most mud and magmatic volcanoes, geysers erupt cyclically, and their eruptions are accompanied by pressure changes in a source region. The similarity of eruptive and source processes makes geysers potential analogs to volcanic systems for which we do not have long observational records (*Hurwitz et al.*, 2007; *Kieffer*, 1984). In Chapter 8, I present measurements of ground deformation near Old Faithful Geyser of Calistoga, CA. The borehole tiltmeter measurements of ground deformation reveal cyclic changes in tilt, which I interpret as being caused by the filling of the geyser's conduit. I present a physical model linking subsurface dynamics to ground deformation. The model predicts that recharge between geyser eruptions is controlled by the material properties of the region surrounding an inlet to the geyser's vertical conduit and provides a mechanism for seasonal changes in eruption interval.

Chapter 2

Fracture Penetration in Planetary Ice Shells and Thermal Emissions from Fractures

2.1 Abstract

The proposed past eruption of liquid water on Europa and ongoing eruption of water vapor and ice on Enceladus have led to discussion about the feasibility of cracking a planetary ice shell. We use a boundary element method to model crack penetration in an ice shell subjected to tension and hydrostatic compression. We consider the presence of a region at the base of the ice shell in which the far-field extensional stresses vanish due to viscoelastic relaxation, impeding the penetration of fractures towards a subsurface ocean. The maximum extent of fracture penetration can be limited by hydrostatic pressure or by the presence of the unstressed basal layer, depending on its thickness. Our results indicate that Europa's ice shell is likely to be cracked under 1-3 MPa tension only if it is $\leq$2.5 km thick. Enceladus' ice shell may be completely cracked if it is capable of supporting $\sim$1-3 MPa tension and is less than 25 km thick.

2.2 Introduction

Liquid water may erupt on icy satellites of Saturn and Jupiter. The presence of topographic features on Europa such as smooth regions filling topographic lows and often bounded by ridges suggests that liquid water has erupted onto the ice-covered moon's surface (e.g. *Fagents*, 2003; *Miyamoto et al.*, 2005; *Prockter and Schenk*, 2005). On Enceladus, a mixture of water vapor and ice is currently erupting from the "Tiger Stripe" fissures in the south polar region (*Hansen et al.*, 2006). Although the requirement of liquid water is hotly debated (e.g. *Kieffer and Jakosky*, 2008), some models favor the eruption of liquid, rather than sublimation of a solid, on Enceladus (*Porco et al.*, 2006). The ongoing eruption at Enceladus' South Pole appears to occur through tensile fractures (*Hurford et al.*, 2007a).

Water confined to a subsurface ocean faces two mechanical impediments in reaching the surface. First, it is negatively buoyant with respect to ice and second, it needs a conduit through which to flow. If tensile stresses generated in an ice shell exceed the tensile strength of ice, a fracture will form and may provide the necessary conduit. Downward penetration of tensile fractures initiated at the surface is opposed by lithostatic pressure and by the absence of tensile stresses in the lower part of the shell, which become relaxed over long time scales (*Nimmo*, 2004; *Manga and Wang*, 2007). We use a numerical model to test the feasibility of fracturing an ice shell whose lower region does not support far-field tensile stresses.

Lee et al. (2005) and *Qin et al.* (2007) studied fracture penetration in an elastic medium with finite thickness and variable porosity. Their results indicate that the presence of a lower free-surface enables fractures to penetrate further than they would under otherwise identical conditions in a halfspace. Neither study accounts for the presence of a basal layer in which deviatoric stresses are relaxed, which is the focus of our study.

2.3 Background

Estimates of the thickness of Europa's ice shell lie within the range of about 1 km to at least 32 km (*Billings and Kattenhorn*, 2005). The maximum thickness of Europa's ice shell is constrained by the vertical extent of its ice+water shell, between 105 and 160 km depending on the composition and structure of the underlying rocky layers (*Kuskov and Kronrod*, 2005; *Cammarano et al.*, 2006). Enceladus has a mean radius of 252.1 ± 0.2 km and may be partially- to fully-differentiated (*Porco et al.*, 2006). In the latter case, the thickness of the ice+water shell is ~ 90 km, with an ice-only thickness of 10-90 km (*Schubert et al.*, 2007).

In order to fracture an ice shell, there must be a physical mechanism capable of producing stresses in excess of the tensile strength of the material. Europa's shell is exposed to a diurnally varying tidal stress of magnitude 0.1 MPa (*Hurford et al.*, 2007b). *Nimmo* (2004) calculated the stresses due to cooling and freezing at the base of an ice shell and found that extensional stresses exceed 10 MPa for shells that thicken to more than 10 km. When the compressibility of the underlying ocean is taken into account, stresses in the shell are reduced but still large, ∼1-3 MPa (*Manga and Wang*, 2007). The maximum stress due to non-synchronous rotation or true polar wander is of order 1-10 MPa (*Leith and McKinnon*, 1996). *Schenk et al.* (2008) have suggested that surface features present on Europa indicate the occurrence of true polar wander. In combination, these stresses are sufficient to overcome the tensile strength of ice on Europa. Enceladus orbits Saturn with an eccentricity of 0.0047, producing tidal stresses on the order of 0.1 MPa (*Hurford et al.*, 2007a). *Nimmo and Pappalardo* (2006) have proposed that Enceladus underwent diapir-induced re-orientation, which would produce tectonic stresses on the order of 10 MPa. Ocean pressurization due to ice shell thickening, should a subsurface ocean exist, could also produce stresses of 1-10 MPa for plausible changes in shell thickness (*Manga and Wang*, 2007).

2.4 Model

Physical Model

We model the ice shell as a single homogenous and isotropic linear elastic layer (Fig. 2.1). The entire shell deforms elastically on the time scale of crack propagation. Prior to fracturing, the upper region of the ice shell is stressed, and the stress, σ_T is assumed to be equal to the tensile strength of ice. Meanwhile, the lower, warmer part of the shell undergoes viscous deformation and tensile stresses will have relaxed. The depth at which viscous deformation dominates depends on the time scale over which stresses are applied. The upper boundary is a free-surface. The lower boundary does not support shear tractions and the normal component of stress must be continuous across this water-ice interface. The crack walls are prescribed to be free of shear tractions. Cracks are initiated at the upper surface because the applied tension is uniform across the elastic layer and hydrostatic pressure is zero at the

surface. Once a fracture forms at the upper surface, the normal tractions exerted on its walls are the superposition of overburden and extensional stresses in the upper region of the ice shell, but only overburden stresses act in the lower, unstressed region. We assume that the acceleration due to gravity remains constant with depth, a reasonable assumption since the (highly uncertain) tensile strength of ice has a greater effect on our results.

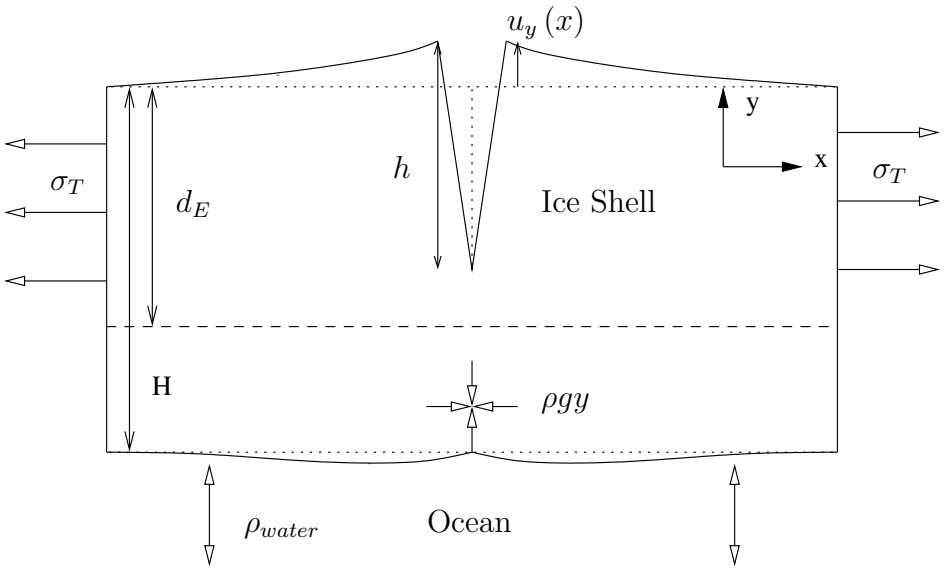

Figure 1. Rudolph and Manga, Fracture Penetration

Figure 2.1: Schematic illustration of our model geometry as described in Section 2.4. The dashed line at depth d_E represents the depth below which tensile stresses do not exist. The quantity $\Delta\rho$ is the difference in densities of water and ice, 90 kg/m^3.

In all cases, we let the Young's modulus $E = 5 \times 10^9$ Pa (*Nimmo*, 2004) and Poisson's ratio $\nu = 0.33$ (*Schulson*, 2001). A summary of the physical quantities used in our modeling is provided in Table 2.1.

The relevant thickness of the stressed upper layer depends on the time scale over which stresses are applied. The time scale governing viscous relaxation is the Maxwell time $\tau_M = \mu/E$. *Nimmo* (2004) assumed that viscous deformation dominates after O(10) Maxwell times and defined the temperature at which the elastic-viscous transition occurs as $T = 180$K. This corresponds to an effective viscosity (assuming exponential dependence of viscosity on temperature) of $\sim 10^{18}$ Pa-s and a Maxwell time $\tau_m \approx 50$ years. The temperature profile in an ice shell depends on whether or not the viscous part of the ice shell convects. Based on this choice of τ_M, if heat transfer occurs only through conduction, Europa's stressed layer has a fractional thickness (d_E/H) of about 0.5 and Enceladus' stressed layer comprises about 0.6 of its total ice shell thickness. *Manga and Wang* (2007) suggested time scales of $\tau_P = 10^5$

	Europa	Enceladus
g	1.3 m s^{-2}	0.13 m s^{-2}
H	1-35 km	10-90 km
d_E/H	0.2-0.5	0.2-0.6
ρ_{ice}	910 kg m^{-3}	
σ_T	1-3 MPa	
E	5 GPa	
ν	0.33	

Table 2.1: Physical quantities used in the model.

and 10^8 years for changes in stress due to ice shell thickening on Europa and Enceadus, respectively. By setting $10\tau_M = \tau_P$, we obtain corresponding temperatures of 140K and 123K and fractional stressed thicknesses of 0.2 for both satellites. We therefore primarily consider fractional stressed thicknesses of 0.2-0.5 for Europa and 0.2-0.6 for Enceladus.

In linear elastic fracture mechanics, the stress intensity factor describes the concentration of stresses at the tip of a crack (*Irwin*, 1957). There is a singularity in stress at the tip of a crack in a linear elastic material, which in nature is accomodated through plastic deformation. Here, we consider Mode-I fracture, in which crack walls undergo only normal displacement. A Mode-I fracture will grow if the crack-tip stress intensity factor, K_I, exceeds a critical value K_{IC} that is material-dependent. Stresses near a crack tip decay with $r^{-1/2}$ where r is distance from the crack tip, and K_I may be calculated by evaluating the normal traction acting on a crack-coplanar surface very close to the crack tip (*Crouch and Starfield*, 1983).

The tensile strength of ice on either satellite is the most poorly constrained physical property in our model. Fracture-free, avesicular ice Ih with a grain size of 1 mm has a measured tensile strength of 1.5 MPa at -10°C, while ice with finer grains may fail at 17 MPa (*Schulson*, 2001, 2006). Relevant temperatures on Europa and Enceladus are colder than those at which tensile strengths have been measured. Europa's low-latitude surface temperature is between 86 and 132 K (*Spencer et al.*, 1999). The mean surface temperature on Enceladus is 75 ± 3 K and also varies with latitude (*Grundy et al.*, 1999). The temperature increase across Europa's ice shell is about 170 K (*Nimmo*, 2004), resulting in laboratory-like conditions at the base of the shell. Both the compressive and tensile strengths of ice increase as temperature decreases, although the effect is less pronounced under tension (*Schulson*, 2001). Fractured or porous ice may be significantly weaker (e.g. *Lee et al.*, 2005) and tensile strength may be scale-dependent; the in-situ tensile strength of sea ice is $\sim 10^5$ Pa on length scales of hundreds of meters (e.g. *Dempsey et al.*, 1999). We assume tensile strengths in the range of 1-3 MPa for consistency with previous studies (*Manga and Wang*, 2007; *Leith and McKinnon*, 1996).

Numerical Method

We use an indirect boundary element method modified from the program TWODD (*Crouch and Starfield*, 1983) to calculate the displacements along fractures in a two dimensional linear elastic medium. Our first modification is the addition of a crack tip element that facilitates the calculation of crack-tip stress intensity factors. We also account for gravity and buoyancy at the upper and lower boundaries. Rather than describing these forces as a body force acting throughout the shell, we approximate them by imposing normal tractions $t_y = \rho_i g u_y$ and $t_y = (\rho_w - \rho_i)\, g u_y$ on the upper and lower boundaries, respectively. Here, t_y is the (normal) boundary traction, u_y is vertical displacement, ρ is density, g is acceleration due to gravity, and the subscripts w and i denote water and ice. Because we treat the problem using linear elasticity and strains are small, this is a good approximation. Note that Fig. 2.1 reflects the boundary conditions described in Section 3.1 whereas in our numerical model, we have modified the boundary conditions to account for gravity. The upper and lower boundaries are both free of shear tractions. Each of these boundaries is prescribed to be 50 times greater in width than the shell thickness and element size varies linearly with distance from the crack, consistent with *Qin et al.* (2007). We begin each calculation by initiating a fracture with length l_0 at the upper boundary along the y-axis. The crack-tip stress intensity factor is computed by evaluating σ_{xx} a distance $r = 10^{-6} l_0$ from the crack tip (*Crouch and Starfield*, 1983). If the stress intensity factor is positive, we increase the length of the crack in 50 meter increments until K_I is no longer positive, consistent with the procedure used by *Qin et al.* (2007). Because the stress intensity factor decreases very rapidly near $K_I = 0$ as crack length increases in a hydrostatic stress field, this criterion for propagation produces the same results as using $K_I > K_{IC}$ to within our 50-m crack length increment (*Lee et al.*, 2007). By adopting this propagation criterion, the fractional penetrations that we obtain are upper bounds on what should be expected in a medium with nonzero fracture toughness.

Lachenbruch (1961) studied the propagation of cracks in an elastic halfspace subjected to the same horizontal loading conditions that we impose. Because his semi-analytic solution is not for the case of an elastic layer with a lower boundary, it does not adequately describe all of the cases that we analyzed. In order to validate our numerical model, we compared our predictions of fracture penetration depth to those predicted by the Lachenbruch solution. For the case $K_{IC} = 0$, we compared Lachenbruch's solution and our numerical solution for a typical crack on Enceladus where the stressed layer thickness $d_E = 6$km and $\sigma_T = 3$MPa. For consistency with the Lachenbruch solution, we removed the lower boundary from our model. The solution given by *Lachenbruch* (1961) for this case is $h = 0.36\sigma_T / (0.68\rho g)$. This solution yields $h = 13426$m, whereas our numerical result is $h = 13400$m. The two solutions agree to within our spatial resolution of 50m. We also validated our code against analytic solutions for uniformly pressurized spherical cavities and cracks in infinite media (*Crouch and Starfield*, 1983).

2.5 Results and Discussion

Figures 2.2 and 2.3 show the fractional penetration depth (h/H) of cracks on Europa and Enceladus, respectively, as a function of tensile strength and stressed layer thickness. Throughout our analysis, we presume that the tensile strength is equal to the applied tensile stress in the upper layer. If the tensile strength is 1 MPa and the fractional thickness of Europa's stressed layer (d_E/H) is 1/3, none of the shells that we considered can be completely cracked. If d_E/H is 0.9, Europan shells up to 5 km thick may be cracked under 3 MPa tension, but if the tensile strength of ice is 1 MPa, only very thin ($\leq$1 km) shells may be cracked, despite this improbably large value of d_E/H. Figure 2.4 (top) shows contours of minimum tensile stress necessary to completely fracture Europa's ice shell as a function of shell thickness and d_E/H. The shaded region in this figure illustrates the region of parameter space that we consider most reasonable. The thickest shell that may be completely cracked is about 2.5 km, consistent with only the smallest observationally-inferred thicknesses (*Billings and Kattenhorn*, 2005). Even if the tensile strength of ice is 10-20 MPa, about an order of magnitude greater than our preferred values, Europan ice shells thicker than about 9 km cannot be cracked (Fig. 2.4).

If the tensile strength of Enceladus' ice is 1 MPa, even a 2/3-stressed, 10-km shell (the thinnest shell we considered) cannot be cracked. If the tensile strength is 3 MPa, a 2/3-stressed 30 km shell may be cracked as may a 1/2-stressed 20 km shell. When the stressed layer comprises only 1/3 of the total thickness, none of the model shells can be cracked. The shaded region in Fig. 2.4 (bottom) indicates our preferred range of parameters for which tensile fractures may completely penetrate Enceladus' shell. Given our assumed range for the tensile strength of ice and d_E/H between 0.2 and 0.6, ice shells up to 25 km in thickness may be completely cracked. Thus, it is possible that tensile fractures initiated at Enceladus' surface penetrate its ice shell and reach a subsurface ocean. If the low-temperature tensile strength of ice is an order of magnitude higher than we have assumed, the comparatively low gravitational acceleration on Encaladus will allow a large increase in crackable shell thickness; Shells up to and exceeding 60 km in thickness may be cracked under 10 MPa tension with d_E/H within our preferred range (Fig. 2.4).

The dashed violet curves in Figs. 2.2 and 2.3 indicate the depth at which hydrostatic compression negates the applied tension. Extension and hydrostatic compression balance at a depth $d_0 = \sigma_T/(\rho g)$. When $\sigma_T = 1$ MPa, $d_0 = 8.5$ km on Enceladus and $d_0 = 0.85$ km on Europa. In general, the fractures propagate past the depth at which horizontal stresses become compressive. Once a fracture has propagated past this depth, its tip is supported by stresses resulting from opening in the upper region (which experiences extensional stresses) and by the concentration of tensile stresses between the crack tip and the lower boundary. The latter effect is responsible for the large fractional penetrations seen clearly in Fig. 2.2 (bottom). This effect was also previously reported by *Lee et al.* (2005). If the stressed thickness is smaller than d_0, crack penetration is limited by the extent of the stressed layer. When the stressed layer extends below d_0, crack penetration is limited solely by hydrostatic

compressive stress. The former limiting scenario applies to thin shells and counteracts the stress concentration due to the presence of a lower boundary. *Lee et al.* (2005) predicted that thin Europan shells could be easily cracked under tension but neglected the effect of the unstressed lower region on crack penetration.

As in *Manga and Wang* (2007), we assume that the ice shell is unfractured and is capable of supporting tensile stresses of up to the tensile strength over the characteristic time scale of stress increase. We have also assumed that tensile strength does not vary significantly with depth. The effect of temperature on tensile strength within the ice shell may be negligible (*Schulson*, 2001), but porosity may substantially reduce tensile strength in the upper region of the shell (*Lee et al.*, 2005). In this case, the upper shell would be easily fractured (possibly by the diurnal tidal stress), while the lower shell could only be cracked by the larger stresses due to ice shell thickening (*Manga and Wang*, 2007), non-synchronous rotation (e.g. *Leith and McKinnon*, 1996), or polar wander (e.g. *Ojakangas and Stevenson*, 1989a).

2.6 Conclusion

It is unlikely that tensile fractures initiated at Europa's surface can propagate all the way to a subsurface ocean unless its ice shell is less than 2.5 km thick. When the tensile strength of ice is taken as 3 MPa, no shell whose thickness is greater than $\sim$5 km may be fractured. If the unstressed part of the ice shell is 2/3 the total thickness, only a $\leq$1 km shell may be fractured. Because gravitational acceleration is an order of magnitude smaller on Enceladus than on Europa, it is much more likely that Enceladus' ice shell may be cracked, and if cracking occurs, water is more likely to erupt (*Manga and Wang*, 2007). Considerably larger fractional penetrations may be achieved if tensile cracks on either satellite can become filled with fluid (e.g. *Crawford and Stevenson*, 1988), which is beyond the scope of this paper.

2.7 Acknowledgments

Stephen Crouch provided helpful correspondence regarding the displacement discontinuity method. Edwin Kite and Eric Gaidos provided useful comments and discussion. We thank Roger Buck and John Dempsey for helpful reviews that enhanced the clarity of our manuscript. This work has been supported in part by NASA grants NNX08AL26G and NNA04CC02A.

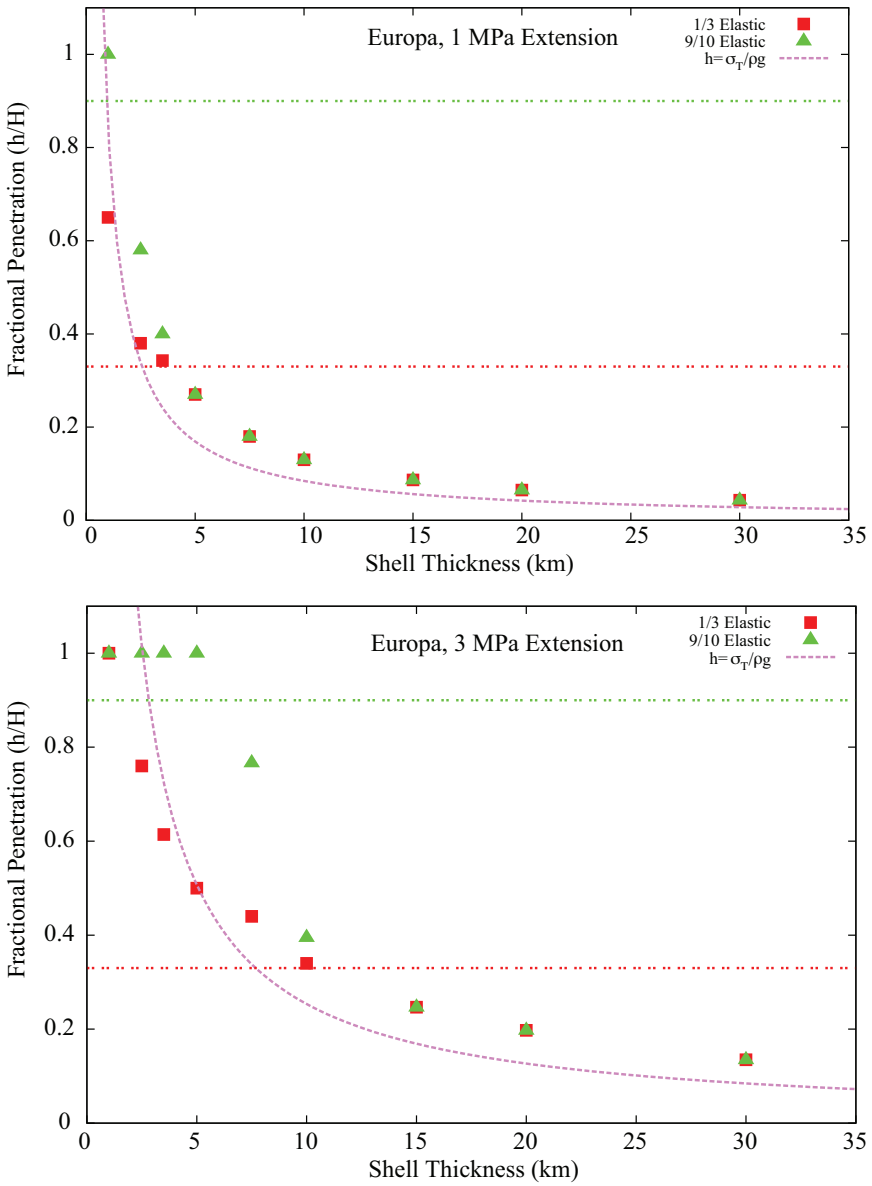

Figure 2.2: Fractional penetration of fractures on Europa taking σ_T to be 1 MPa (top) and 3 MPa (bottom). The red and green horizontal dashed lines indicate the fractional stressed thicknesses of 1/3 and 2/3. The violet curve indicates the depth at which extension is balanced by hydrostatic compression in a completely-stressed halfspace.

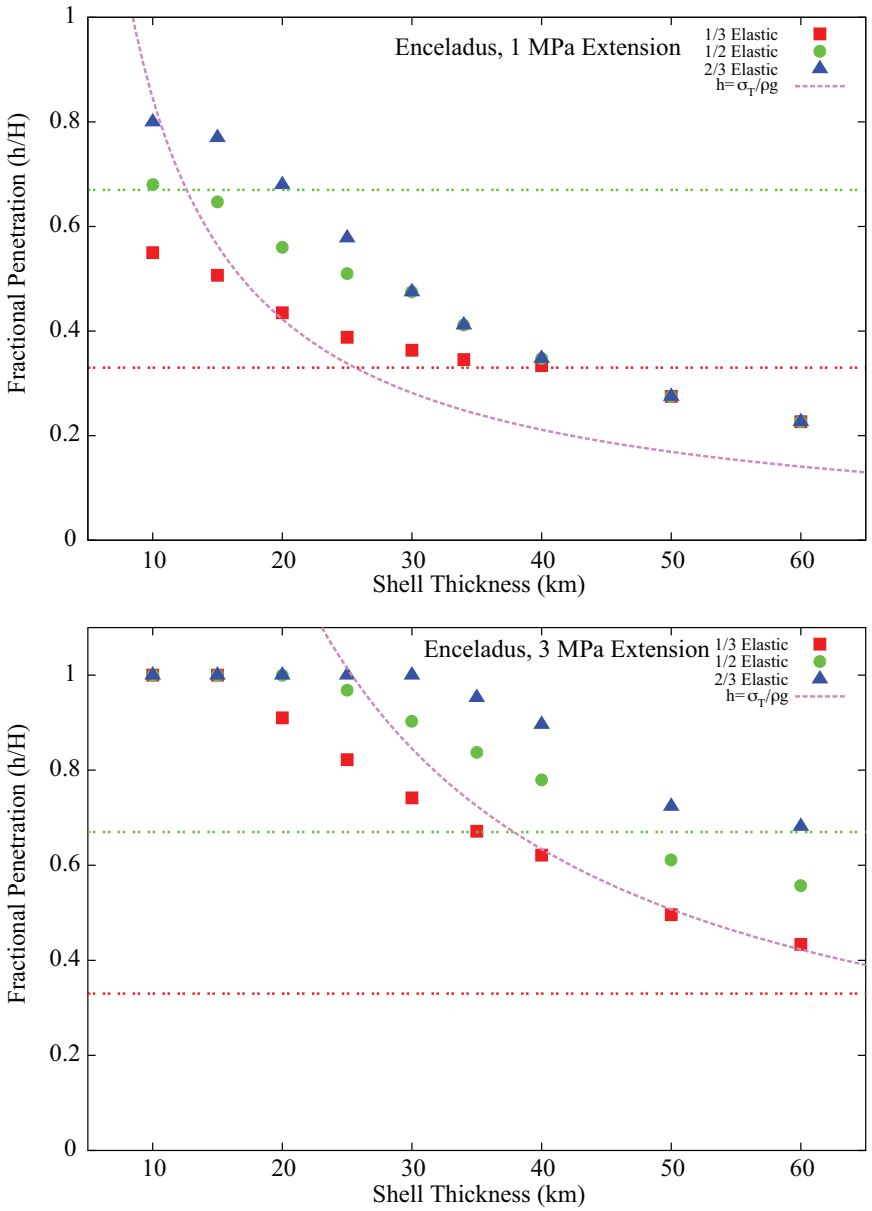

Figure 2.3: Fractional penetration of fractures on Enceladus taking σ_T to be 1 MPa (top) and 3 MPa (bottom). The violet curve indicates the depth at which extension is balanced by hydrostatic compression in a completely-stressed halfspace.

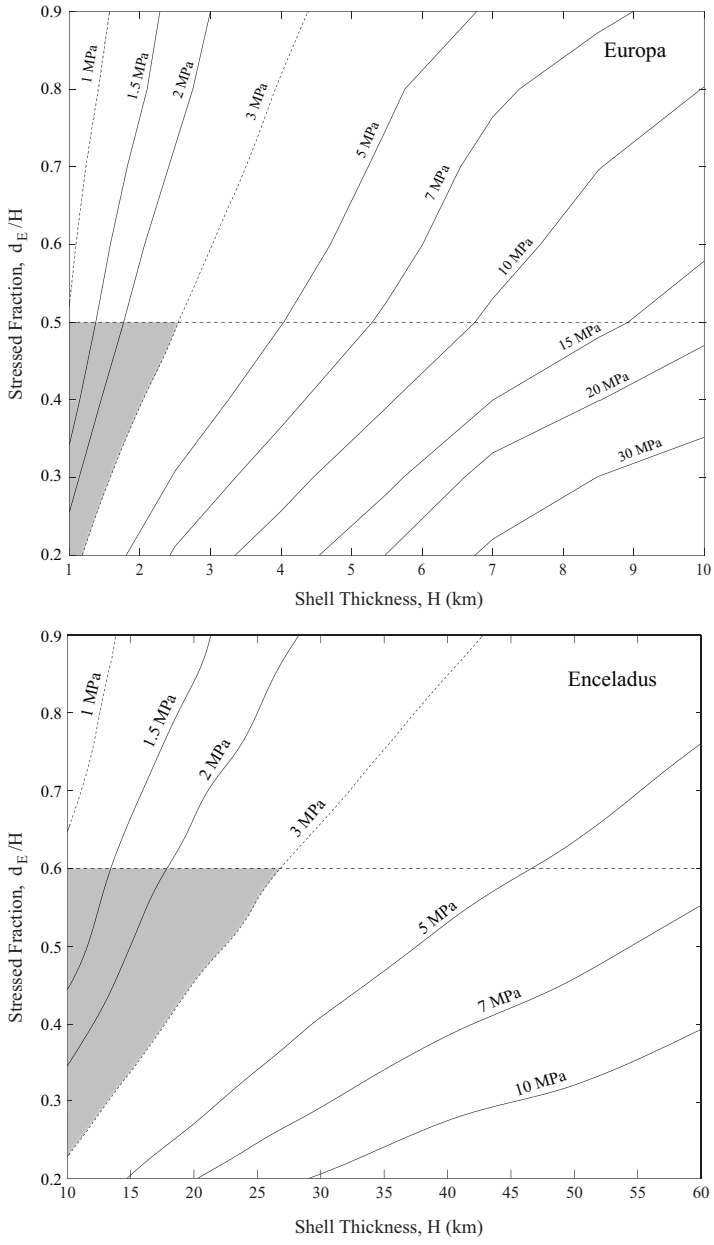

Figure 2.4: Contour plots of σ_T necessary to completely fracture an ice shell on Europa (top) and Enceladus (bottom). Horizontal dashed lines indicate our preferred upper bounds on d_E/H. Dotted curves indicate contours of 1 and 3 MPa. The shaded regions represent the range of parameters using which shells may be completely cracked. These results are consistent with a modified form of the force balance used in *Qin et al.* (2007), which predicts that $d_E/H = (\rho g H)/(2\sigma_T)$ (W.R. Buck, private communication). Contours were generated using linear and spline interpolating functions on originally non-grid data.

2.8 Remote Detection of Active Tectonics from Thermal Emissions

The surface of Europa is both geologically young and extensively fractured. However, it remains unclear whether the tectonic features formed during a geologically recent epoch of tectonic activity or whether Europa is at present tectonically active. *Phillips et al.* (2000) looked for evidence of active tectonics on Europa at large spatial scales by searching for active plumes and young plume deposits using data returned from Voyager and also by comparing images returned from Voyager to those returned 20 years later from Galileo. One of *Phillips et al.* (2000)'s conclusions is that if Europa is tectonically active, evidence of activity must be manifest at smaller length scales than their 4km^2 resolution.

Crack formation is the dominant tectonic process on Europa and the one that we are most likely to witness. Fracture formation has been attributed to stresses induced by orbital parameters including eccentricity, non-synchronous rotation, and obliquity (e.g. *Hurford et al.*, 2007b) as well as internal processes such as ocean solidification (*Nimmo*, 2004; *Manga and Wang*, 2007) and the upward propagation of water filled dikes (*Crawford and Stevenson*, 1988). These features are also abundant and active on other icy satellites; Enceladus' ongoing south polar eruption emanates from tensile fractures. The opening of even very deep tensile fractures in an ice shell results in horizontal opening displacements of just a few meters and produces vertical surface displacements of similar magnitude (*Rudolph and Manga*, 2009a).

The proposed return to Europa by the Jupiter Europa Orbiter (JEO) would afford us a new opportunity to search for evidence of active tectonics. On Earth, we are fortunate to have a variety of tools that can be used to detect active tectonic processes. The most obvious of these is modern seismic instrumentation. Seismometers would be the best tool for detecting active tectonic processes on icy moons (*Lee et al.*, 2005), but there are no seismic instruments on icy moons nor are there any planned, since they require a prohibitively expensive lander. *Sandwell et al.* (2004) studied the ability of InSAR to resolve surface deformations associated with cracking, but no SAR instrument is planned for JEO (*Clark et al.*, 2009). One instrument that is planned for JEO is a thermal instrument (TI), which maps effective temperature at a spatial resolution of about 250m. In a previous paper (*Rudolph and Manga*, 2009b), we established the depth to which tensile fractures may penetrate a planetary ice shell. One consequence of opening a deep fracture is that some thermal infrared radiation emitted deep within the ice shell may escape to space. If detectable, this effect could be used to distinguish between active and inactive features. We place bounds on the size of fracture and thermal state of the ice shell required to make this effect observable using the planned Thermal Instrument (TI) on the Jupiter Europa Orbiter (JEO). Our primary objective in doing so is to assess the feasibility of detecting active tectonic processes on Europa using instruments likely to be part of a future mission to Europa.

2.9 Model

We use a mathematical model to predict the thermal emissions from fractures. We prescribe a crack's geometry and initial temperature distribution and calculate the total power radiated to space. The crack is assumed to extend infinitely in the out-of-plane direction, allowing us to treat the problem in two dimensions. We assume that there is no scattering and reemission of infrared radiation, and that the surface luminance is isotropic. The power emitted by the crack is expected to depend in some way on the imposed initial temperature distribution along the crack's walls and also on the geometry (width, depth) of the feature. In order to simplify our model, we assume that the initial temperature distribution is conductive and we adopt idealized fracture geometries.

Model Parameters

The model requires us to specify several physical parameters. The most important of these are the geothermal gradient and the dimensions of the crack. In general, the temperature distribution in an ice shell is influenced by the freezing temperature at the ice-water interface, the surface temperature, which is related to the radiative balance at the surface, the transport properties of the ice, the amount and distribution of internal heating, and whether and how vigorously the ice shell convects (*Ojakangas and Stevenson*, 1989b). In any case, the near-surface temperature profile is very close to conductive and the geotherm in our calculations should be taken as the geotherm at the surface. *Hussmann et al.* (2002) studied equilibrium thermal states of Europa's ice shell and estimated heat flow of $\sim$ 20 mW/m^2. However, if the thermal state is not steady, higher fluxes of up to $\sim$ 300 mW/m^2 are possible (*Hussmann et al.*, 2002), and a convecting ice shell could feasibly supply heat fluxes of $\sim$ 100 mW/m^2 (*Ruiz and Tejero*, 2003). The most extreme near-surface temperature profile suggested for Europa occurs in the presence of an insulating near-surface regolith ($k \approx 10^{-2}\ W\ m^{-1}K^{-1}$), which implies a temperature increase of 150 K over the uppermost *60 m* of the ice shell (*Seiferlin et al.*, 1996; *Hussmann et al.*, 2002). The existence of such a regolith is physically justifiable; *Eluszkiewicz* (2004) estimated regolith thickness by balancing regolith production and compaction and obtained conservative estimates of 160-1600 m. The thickness of the ice shell, along with the thermal conductivity, surface temperature, and basal temperature, places a lower bound on the geotherm. The relevant thickness to this work is the total thickness, estimates of which range from about 2 to more than 30 km (*Billings and Kattenhorn*, 2005). Accordingly, we test geotherms between 20 K/km and 200 K/km, which correspond to steady-state conductive temperature gradients for thin and thick ice shells, respectively in the absence of any internal heating or regolith layer.

The geometry of the fractures in the model is idealized (Figure 2.5). We test rectangular fractures with vertical walls and widths ranging from 1-10 m and triangular fractures with surface openings ranging from 1-10 m. For each fracture geometry, we test a variety of lengths from 200 m to 5 km. Our choice of fracture dimensions is informed by previous work in which we found that tensile fractures on Europa may penetrate at least 1 and possibly 5

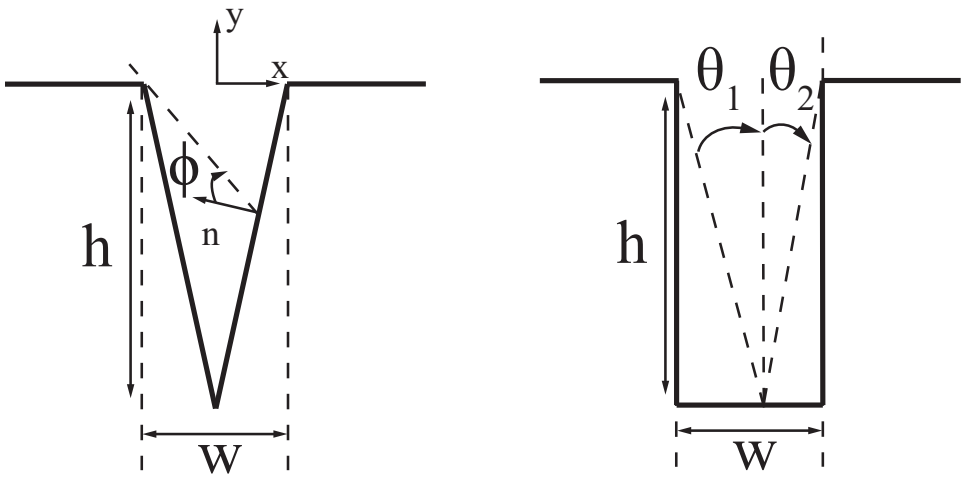

Figure 2.5: Schematic of geometry used in analytic treatment for wedge shape (left) and box shape (right).

Parameter	Value	Source
Thermal conductivity (k)	2.76 W/m/K	*Paterson* (1994)*
Thermal diffusivuty (κ)	$1.73 \cdot 10^{-6}$ m^2 s^{-1}	*Paterson* (1994)
Density of ice (ρ)	917 kg m^{-3}	*Paterson* (1994)
Surface Temperature	50-100 K	*Ojakangas and Stevenson* (1989b)
Infrared Emissivity	0.95	(1−albedo)
Infrared Albedo	0.05	
Geotherm	20-200 K/km	Section 2.9

Table 2.2: Values of parameters used in calculations. *Value given at -50^{o}C. *Hussmann et al.* (2002) imply the upper bound k $< 3\ Wm^{-1}K^{-1}$ if a subsurface ocean exists.

km through the icy shell given reasonable assumptions about the tensile strength of intact ice and the loading conditions (*Rudolph and Manga*, 2009b). The other parameters entering our model are summarized in Table 2.2.

Analytic Model

Here we derive the expression for a box-shaped crack and direct the reader to Section 2.11 for the wedge-shaped crack. If we consider an infinitessimal patch of crack wall dl, the power emitted is $dP = \sigma\epsilon T^4 dl$. The assumption of isotropic luminance in two dimensions results in the expression $i = P/2$ for the radiant intensity i, measured in W m^{-2} rad^{-1}. Note

that this differs slightly from the 3-dimensional case where $i = P/\pi$, where i is measured in W m^{-2} steradian^{-1}. We are interested in computing the power delivered to the region $x \in [-w/2, w/2],\ y = 0$ from all angles of incidence inside the crack. The power delivered from a parcel of crack wall dA to an infinitessmal patch is given by:

$$dP = i\ \cos\phi\ d\omega \tag{2.1}$$

where ϕ is the angle illustrated in Figure 2.5. We can also write the intensity i:

$$i(y) = \frac{\sigma}{2}\left(T_S - G\ y\right)^4 \tag{2.2}$$

where T_S is the surface temperature, G is the geotherm (K/km) and y is vertical position (positive upward). The total power radiated by the crack can be found by evaluating the double integral:

$$P = \int\int \left[i\left(y\right)\ \cos\left(\phi(x,y)\right)\right]\ d\omega\ dl \tag{2.3}$$

where ω is the emission angle and l represents the crack's walls. The box shaped crack is broken down into two subsections (wall and floor).

We construct the integrals over emitting surfaces and the top of the crack:

$$P_{wall} = \int_{-h}^{0}\int_{\phi_{wall}(y)}^{\pi/2} i(y_2)\cos(\omega)d\omega\ dy \tag{2.4}$$

$$P_{floor} = 2\ \int_0^{w/2}\int_{\theta_1(x)}^{\theta_2(x)} i(-h)\ cos(\omega)\ d\omega\ dx \tag{2.5}$$

$$P_{total} = 2P_{wall} + P_{floor} \tag{2.6}$$

The angles that set the limits of the inner integrands are shown schematically in Figure 2.5 and are given by:

$$\phi_{wall}(y) = \pi/2 - \arctan\left(w/-y\right) \tag{2.7}$$

$$\theta_1(x) = \pi/2 + \arctan\left(\frac{w+2x}{2h}\right) \tag{2.8}$$

$$\theta_2(x) = \pi/2 - \arctan\left(\frac{w-2x}{2h}\right) \tag{2.9}$$

The integrals for the box shaped crack can be evaluated analytically, yielding:

$$P_{rect} = \sigma\left(Gh - T_S\right)^4\left(w - 2\sqrt{h^2+w^2} + \sqrt{4h^2+w^2}\right) \tag{2.10}$$

This expression can be evaluated for various choices of G, w, h, and T_S. The wedge-shaped crack is addressed in Section 2.11. This analytic solution is valid immediately after the crack opens. Subsequently, the fracture's walls will lose heat by radiation, decreasing their temperature.

2.10 Discussion

The Thermal Instrument planned for the JEO mission is expected to have a 250 m pixel footprint once JEO is in orbit at 100km and the instrument will have 2K temperature accuracy and 10% radiometric accuracy (*Clark et al.*, 2009). The instrument is a radiometer, not a spectrometer, so detection of active features must be based on changes in radiometric intensity, not changes in wavelength of spectral peaks. This instrument may be able to observe the radiant power emitted by fractures in some cases when cracks penetrate very deep (several km) or probe a steep geotherm (e.g. 150-200 K/km).

To determine the detection limits for an hypothetical thermal instrument (TI), we idealize the footprint of the TI as a square pixel and assume that there is one crack running across the entire pixel with a random orientation. The expected length of crack visible is $l = 1.122\ d$ where d is the pixel size. The fraction of the pixel's area occupied by the crack is therefore $(w\ l)/d^2 = 1.122\ w/d$. If a fracture opens on a previously pristine piece of crust, therefore, the change in radiosity is given by:

$$\Delta = \frac{P_{bkg}(d^2 - w\ l) + l\ P_{crack}}{P_{bkg}\ d^2} = \frac{P_{bkg}(d^2 - 1.122d\ w) + (1/1.122)d\ P_{crack}}{P_{bkg}d^2} \tag{2.11}$$

where P_{crack} is the power emitted from the crack per unit length and P_{bkg} is the background radiosity of the surface. We solve this to obtain P_{crack} for $\Delta = 1.02$. The resulting detection limit as a function of surface temperature and crack width are shown in Figure 2.6. The surface temperature on Europa varies by more than a factor of two, from about 50K near the poles to more than 135K near the equator (e.g. *Ojakangas and Stevenson*, 1989a). Because the opening of a crack appears as a change in total radiometric intensity, it is easier to detect active tectonics on colder parts of the surface for a given TI pixel size and radiometric accuracy.

In Figure 2.7, we show contours of radiated power from cracks with wedge and box shapes for different values of crack length, geotherm G, and opening displacement. With the notional TI planned for the Jupiter Europa Orbiter, prospects of detecting thermal emissions from fractures are dim but not nonexistent. The best prospect for detecting thermal emissions related to fracture opening is in regions that have both a low surface temperature and a large geothermal temperature gradient. The thermal emissions from cracks in ice with a small geotherm must be extremely deep and occur in cold regions to be detectable. Fractures probably become filled with icy debris owing to diurnal tidal deformation and the thermal emissions would be inhibited. In obtaining these results, we made several assumptions, the most important of which are that ice is Lambertian, the albedo is constant (though very small) in the thermal infrared, the cracks are evacuated, and no sublimation is occurring from the crack walls. We also considered briefly the idea from *Hussmann et al.* (2002) that an insulating regolith causes a temperature rise of about 150K over 60 m near the surface (G=2500 K/km). Such a regolith might have some cohesive strength, allowing it to crack as opposed to flow. The opening of a 60m crack would be observable at the 10% level for any crack width greater than 2.5 m. It may be possible to constrain the thickness and

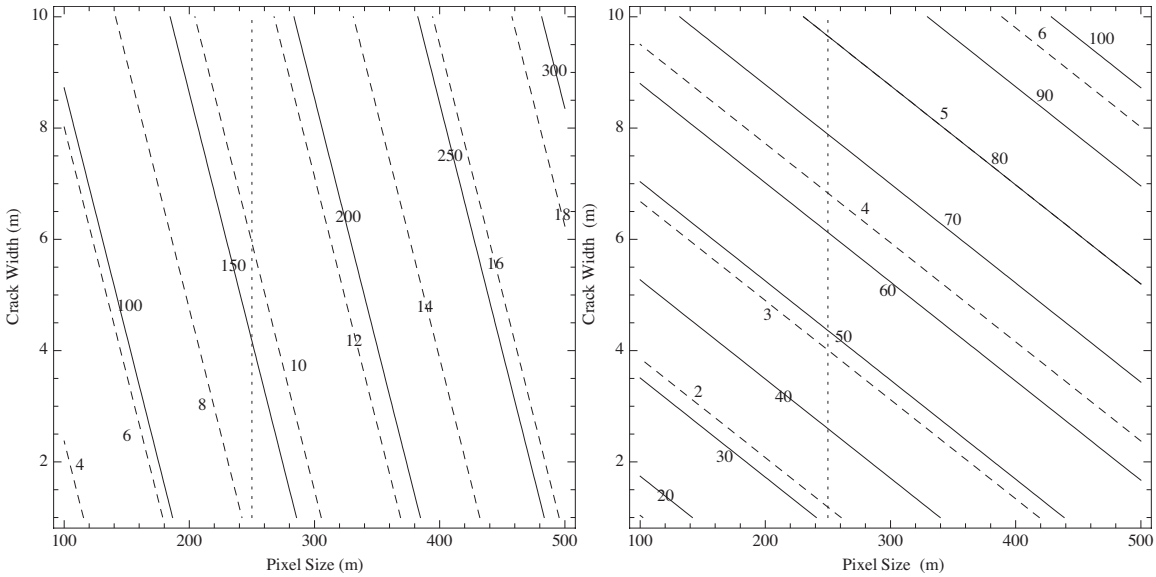

Figure 2.6: Minimum radiant power (W/m) required for detection at 10% level (left) and 2% level (right). Dashed lines indicate $T_{\rm surf} = 50$ K, solid lines indicate $T_{\rm surf} = 100$ K. Vertical dotted line indicates proposed JEO TI spatial resolution.

thermal conductivity of the regolith layer based solely on the detection or lack thereof of thermal emissions associated with crack opening. This technique would be especially viable in combination with images of the fracture before and after formation.

2.11 Wedge-shaped crack

We showed the analytic expression for total power emitted from a box-shaped crack in section 2.9. Here we present the salient modifications to that theory for a wedge-shaped crack with geometry as shown in Figure 2.5. In order to simplify the integral for radiative flux, we perform a change of variables:

$$L = \sqrt{(w/2)^2 + h^2} \tag{2.12}$$

$$x(l) = h(l/L - 1) \tag{2.13}$$

$$y(l) = (wl)/(2L) \tag{2.14}$$

The total power radiated by the crack can be found by evaluating the double integral:

$$P_{tot} = 2 \int_0^L \int_{\phi(l)}^{\pi/2} i\,(y)\ \cos\,(\omega)\ \ d\omega\ dl \tag{2.15}$$

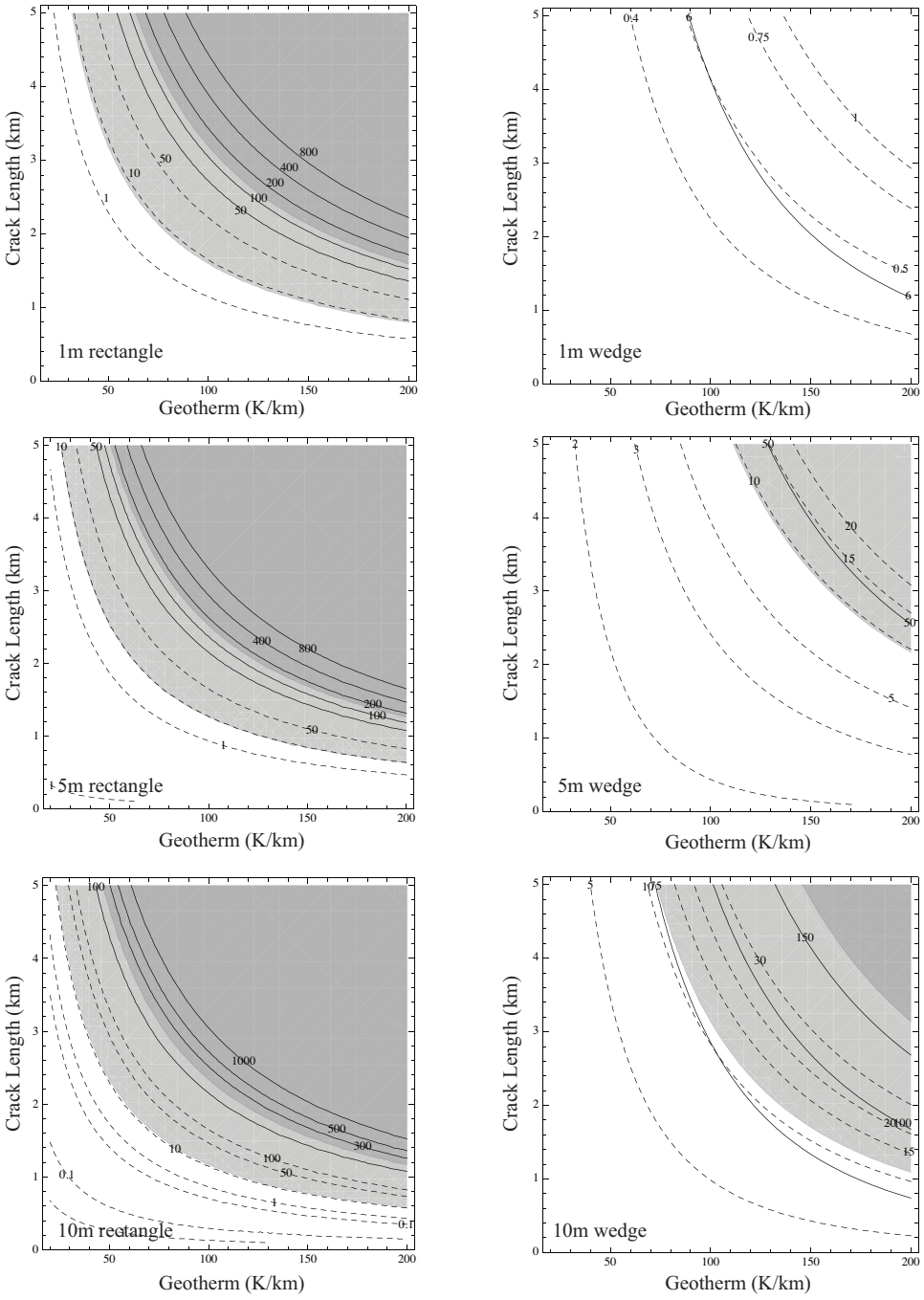

Figure 2.7: Contour plots of radiated power (W/m) as a function of geothermal temperature gradient and crack length for rectangle geometry (left column) and wedge geometry (right column). Dashed lines correspond to surface temperature $T_{\rm surf}$ of 50 K, solid lines correspond to $T_{\rm surf}$ = 100 K. The shaded region indicates detectable region (at 10% level) of parameter space for $T_{\rm surf}$=50K (light grey) and $T_{\rm surf}$=100K (dark grey).

Where the inner integral lower limit of integration is given by:

$$\phi\left(x,y\right)=\frac{\pi}{2}-\arctan\left(\frac{w}{2h}\right)-\arctan\left(\frac{(w/2)+(wl)/(2L)}{h(l/L-1)}\right) \tag{2.16}$$

This integral does not to the best of our knowledge admit a simple analytic solution but may be evaluated numerically for various choices of w, h, G, and T_S. Contours of the numerical solution are shown in Figure 2.7.

Chapter 3

Effects of Texture Development on Convection in Ice Ih Mantles

3.1 Abstract

Convection may occur in the ice shells of moons in the outer solar system. The style of convection, rate of heat transport, and resulting surface features depend on the rheology of ice, which in turn depends on temperature, grain size, stress, and crystallographic preferred orientation (CPO). Here we study the effect of CPO development and anisotropic viscosity on convection by coupling a model of polycrystalline ice deformation with a macroscopic flow model. Despite having a first order effect on velocities and heat transport in a convecting ice shell, fabric development is unlikely to be observable either directly by spacecraft-based radar or indirectly based on changes in the wavelength or amplitude of dynamic topography.

3.2 Introduction

The ice mantles of moons in the outer solar system may transport heat by solid-state convection. The occurrence and style of convection depend on rheology. Below pressures of 2×10^8 Pa and above $\sim$ 72K, ice Ih is the stable phase of water ice. Under some temperature and stress conditions, ice Ih crystals deform most easily by basal slip (occurring on planes perpendicular to the crystal's c-axis - the axis of six-fold symmetry). The resolved shear stress on the basal planes depends on the orientation of the ice crystal, and hence the single crystal has anisotropic viscosity. When polycrystalline ice develops crystallographic preferred orientation (CPO), the ice has anisotropic viscosity (e.g. *Cuffey and Paterson*, 2010).

Understanding and identifying current or past convection is important for three reasons. First, convection affects the overall rate of heat transport and governs thermal evolution (*Consolmagno and Lewis*, 1978; *McKinnon*, 1999; *Ruiz and Tejero*, 2003; *Barr et al.*, 2004; *Mitri and Showman*, 2005; *Freeman et al.*, 2006; *Barr and McKinnon*, 2007; *Roberts and Nimmo*, 2008; *Ruiz*, 2010; *Travis et al.*, 2012) and, consequently, the rheological properties of an icy body. In turn, temperature and rheology affect the location and amount of tidal dissipation (*Hussmann et al.*, 2002; *Sotin et al.*, 2002; *Tobie et al.*, 2003; *Moore*, 2006; *Mitri and Showman*, 2008; *Běhounková et al.*, 2010; *Han and Showman*, 2010). Second, convection may produce some of the surface features observed on icy bodies. For instance, Europa's ridges (*Han and Showman*, 2008), pits (*Showman and Han*, 2004) and domes (*Rathbun et al.*, 1998; *Pappalardo et al.*, 1998; *Nimmo and Manga*, 2002; *Pappalardo and Barr*, 2004; *Han and Showman*, 2005; *Ruiz et al.*, 2007), and chaos features (*Schenk and Pappalardo*, 2004; *Showman and Han*, 2005) have been linked to convective processes. Third, convection transports mass vertically and may carry material from a subsurface ocean to the near-surface or create conditions that allow other processes to transport this material to the surface (*Fagents et al.*, 2000; *Manga and Wang*, 2007).

Here, we study the effects of the development of crystallographic preferred orientation (CPO) and the resulting viscous anisotropy on convection in ice. We describe an anisotropic viscoplastic model linking single-crystal deformation to polycrystal deformation. Next, we present a method to include the polycrystal deformation model within geodynamic models

and present the results of numerical simulations. We discuss the implications of these simulations in the context of whether the resulting features might be detectable and whether fabric development affects topographic features and thermal evolution of icy moons.

3.3 Methods

In order to model the deformation of textured polycrystalline ice, we first describe a model linking grain-scale deformation to macroscopic stress and strain. We then include the micro-scale model in a macroscopic convection calculation in which we employ Lagrangian tracer particles to track texture. The constitutive laws typically used in ice-sheet modeling take the form (*Paterson*, 1994)

$$\dot{\epsilon}_{ij} = A\tau^{n-1}\sigma^D_{ij} \ , \tag{3.1}$$

where the effective stress $\tau = \sqrt{\frac{1}{2}\mathrm{II}_{\sigma^D}}$ and II_{σ^D} is the second deviatoric stress invariant, $\underline{\sigma}^D$ is the deviatoric stress tensor, and $\underline{\dot{\epsilon}}$ is the strain-rate tensor. The term A depends foremost on temperature, as well as pressure, melt fraction, the presence of impurities, and grain size for some creep mechanisms. The key features of Equation (3.1) are that if $n \neq 1$ a nonlinear relationship exists between stress and strain-rate and that if τ is known, $\dot{\epsilon}_{ij}$ depends only on σ^D_{ij} and not any other components of the stress tensor. Fluids with anisotropic viscosity have constitutive equations of the form

$$\dot{\epsilon}_{ij} = M_{ijkl}\sigma^D_{kl} \ , \tag{3.2}$$

where $\underline{\underline{M}}$ is a fourth rank tensor that is, in general, a non-linear function of stress, temperature, grain size, and fabric.

Model for polycrystal deformation and texture development

We write the single-crystal stress and strain rate tensors $\underline{s}$ and $\underline{d}$ and the polycrystal stress and strain rate tensors $\underline{S}$ and $\underline{D}$ following the notation of *Castelnau et al.* (1996). The rate of deformation on a slip system s is:

$$\dot{\gamma}^s = \dot{\gamma_0}\left|\frac{\underline{r}^s : \underline{s}}{\tau^s_0}\right|^{n^s-1}\frac{\underline{r}^s : \underline{s}}{\tau^s_0} \ , \tag{3.3}$$

where $\underline{r}^s = \underline{b} \otimes \underline{n}$ is the Schmid tensor for slip system s, $\underline{b}$ is the Burgers vector and $\underline{n}$ the unit normal to slip system s, n^s is the power law exponent (Equation 3.1) for slip system s, $\otimes$ denotes the tensor product (e.g. *Chadwick*, 1999), $\dot{\gamma_0}^s$ and τ^s_0 are reference slip rate and stress, and : denotes the tensor inner product ($\underline{a} : \underline{b} = a_{ij}b_{ij}$). Temperature dependence enters through the term $\dot{\gamma}_0$, which we modify to take the form $\dot{\gamma}^s_0/(\tau^s_0)^{n^s} = \beta A(T)$, where $A(T) = A_0 \exp(-Q/RT)$ (*Thorsteinsson*, 2002). The single-crystal velocity gradient tensor $\underline{l}$ is computed from $\dot{\gamma}$ (Eqn. 3.3) by summation over all slip systems:

$$\underline{l} = \dot{\gamma}_0 \sum_s \underline{r}^s \left| \frac{\underline{r}^s : \underline{s}}{\tau_0^s} \right|^{n^s - 1} \frac{\underline{r}^s : \underline{s}}{\tau_0^s} \ . \tag{3.4}$$

In order to relate single-crystal stress and strain to macroscopic stress and strain, we must make assumptions about how stress is distributed within the polycrystal, and in particular, whether and how much each grain affects its neighbors. Some closure relationships ignore neighbor interactions entirely (e.g. *Castelnau et al.*, 1996) while others explicitly account for this effect (*Thorsteinsson*, 2002), which requires tracking the spatial distribution of individual crystals in addition to their orientation and shape. The *Thorsteinsson* (2002) model is attractive for our purposes because it captures the essential features of texture development through grain re-orientation and compares favorably with viscoplastic self-consistent (VPSC) models (*Lebensohn and Tome*, 1993) with significantly reduced computational expense. *Thorsteinsson* (2002) introduces a relationship between single crystal and macroscopic stress tensors of the form

$$\underline{s} = \mathcal{E}^c \underline{S} \ . \tag{3.5}$$

The polycrystal is represented as a three-dimensional grid of crystals and $\mathcal{E}^c$ is a neighbor-interaction term defined as

$$\mathcal{E}^c = \frac{1}{\zeta + 6\xi} \left(\zeta + \xi \sum_{i=1}^{6} \frac{\mathcal{T}^i}{\mathcal{T}^c} \right) \ . \tag{3.6}$$

Here, ζ and ξ are tuning parameters that control the strength of the neighbor interactions. Note that when $\zeta = 1$ and $\xi = 0$, $\underline{s} = \underline{S}$, recovering the uniform stress approximation (*Taylor*, 1938). The superscript ^{c} denotes the crystal for which $\underline{s}$ is being computed and the summation index i denotes the six neighboring crystals (left, right, up, down, front, back) in the three-dimensional grid. The term $\mathcal{T}^i$ is a measure of the total resolved shear stress on all active slip systems in crystal i:

$$\mathcal{T}^i = \left| \sum_s \tau^s \hat{\underline{b}}^s \right| , \tag{3.7}$$

and $\hat{\underline{b}}^s$ is the Burgers vector for slip system s.

Substituting Equation (3.5) into Equation (3.4), we obtain an expression for the single crystal velocity gradient:

$$\underline{l} = \dot{\gamma}_0 \sum_s \underline{r}^s \mathcal{E}^c \left| \frac{\underline{r}^s : \underline{S}}{\tau_0^s} \right|^{n^s - 1} \frac{\underline{r}^s : \underline{S}}{\tau_0^s} \ . \tag{3.8}$$

By assumption, the macroscopic velocity gradient is the volumetric average of the microscopic velocity gradients over N single crystals:

$$\underline{\underline{L}} = \frac{1}{N}\sum_{c=1}^{N} \underline{\underline{l}} \ . \tag{3.9}$$

To obtain a numerically useful constitutive equation, we first combine Equations (3.8) and (3.9):

$$\underline{\underline{L}} = \frac{1}{N}\sum_{c=1}^{N} \dot{\gamma}_0 \sum_s \underline{r}^s \mathcal{E}^c \left| \frac{\underline{r}^s : \underline{S}}{\tau_0^s} \right|^{n^s-1} \frac{\underline{r}^s : \underline{S}}{\tau_0^s} \ . \tag{3.10}$$

Noting that $\underline{r}(\underline{r} : \underline{S}) = (\underline{r} \otimes \underline{r}) : \underline{S}$,

$$\underline{\underline{L}} = \left[\frac{1}{N}\sum_{c=1}^{N} \dot{\gamma}_0 \sum_s \frac{(\underline{r}^s \otimes \underline{r}^s)}{\tau_0^s} \mathcal{E}^c \left| \frac{\underline{r}^s : \underline{S}}{\tau_0^s} \right|^{n^s-1} \right] : \underline{S} = \underline{\underline{M}}(\underline{S}) : \underline{S} \ , \tag{3.11}$$

where $\underline{\underline{M}}(\underline{S})$ is a fourth rank tensor, conceptually identical to the elasticity tensor $\underline{\underline{C}}$, but which is in this case a non-linear function of the macroscopic stress tensor $\underline{S}$. The tensor inner product between mixed-rank tensors here is defined $(\underline{\underline{A}} : \underline{B})_{ij} = A_{ijkl}B_{kl}$. The velocity gradient tensor $\underline{L}$ is related to strain rate $\underline{D} = \frac{1}{2}\left(\underline{L} + \underline{L}^T\right)$. Substitution of $\underline{\underline{M}}$ yields in index notation:

$$D_{ij} = \frac{1}{2}\left(M_{ijkl} + M_{jikl}\right) S_{kl} = M^S_{ijkl} S_{kl} \ . \tag{3.12}$$

In order to express stress in terms of strain-rate, we take the common approach of vectorizing $\underline{S}$ and $\underline{D}$ and denote the vectorized stress and strain-rate $\hat{S}$ and $\hat{D}$. The corresponding second order equivalent of $\underline{\underline{M}}^S$ is $\hat{\underline{\underline{M}}}^S$, numerically a square matrix that can be inverted to yield $\hat{\underline{\underline{N}}} = \hat{\underline{\underline{M}}}^{S^{-1}}$, and $\hat{S} = \hat{\underline{\underline{N}}} \cdot \hat{D}$, which can be used in the macroscopic numerical model.

Finally, we introduce the time evolution of the crystal fabric. We express the rate of change in c-axis orientation ($\underline{c}$) as

$$\dot{\mathbf{c}} = \underline{w}\mathbf{c} \ , \tag{3.13}$$

where $\underline{w} = \frac{1}{2}(\underline{l} - \underline{l}^T)$ is the single-crystal rate of spin tensor. We also account for the rotation of the polycrystal by macroscopic flow.

Composite Rheology

Goldsby and Kohlstedt (2001) proposed a composite rheology for ice of the form

$$D = D_{\text{disl}} + \left(D_{\text{gbs}}^{-1} + D_{\text{bs}}^{-1}\right)^{-1} + D_{\text{diff}} \ . \tag{3.14}$$

The first term, D_{disl}, the strain-rate due to dislocation creep not occurring by basal slip, is negligible for the temperatures, stresses, and grain sizes considered here. One key feature

of this proposed composite rheology is that the reciprocal grouping of strain rates due to grain boundary sliding (D_{gbs}) and basal slip (D_{bs}) allows either mechanism to limit the effectiveness of the other deformation mechanism. The final term D_{diff} is the strain rate due to diffusion creep, discussed below. We introduce a scalar creep inhibition factor α to capture the effect of the reciprocal term in Equation (3.14):

$$\alpha = \frac{\sqrt{\underline{D}_{\mathrm{gbs}} : \underline{D}_{\mathrm{gbs}}}}{\sqrt{\underline{D}_{\mathrm{bs}} : \underline{D}_{\mathrm{bs}}}} \ , \tag{3.15}$$

where D_{bs} encompasses all of the deformation accounted for by our micro-scale model. The total strain rate is given by:

$$\underline{D} = \left(\frac{\alpha}{1+\alpha} \underline{D}_{\mathrm{bs}} \right) + \underline{D}_{\mathrm{diff}} \ . \tag{3.16}$$

Recalling that $\underline{D}_{\mathrm{bs}} = \underline{\underline{M}} \cdot \underline{S}$, we introduce a modified viscoplasticity tensor $\underline{\underline{M}}'$ that accounts for all deformation mechnisms

$$M'_{ijkl} = \frac{\alpha}{1+\alpha} M_{ijkl} + 2\delta_{ik}\delta_{jl}\eta_{\mathrm{diff}} \ , \tag{3.17}$$

where η_{diff} is the effective viscosity for diffusion creep. Because we model two-dimensional convection but the anisotropic viscous response is three dimensional, we impose a constraint on the polycrystal to prohibit out of plane deformation. Three dimensional simulations, which are currently prohibitively computationally expensive, will be needed to quantify the effect of the plane-strain constraint.

We calibrate the micro-macro model against the basal slip component of the *Goldsby and Kohlstedt* (2001) model. We assume temperature dependence of the form

$$\dot{\gamma}_0 = A_0 \exp\left(-Q/(RT)\right) (\tau_0^s)^n \ . \tag{3.18}$$

For basal slip, $n = 2$ is favored by *Castelnau et al.* (1997). We choose $Q = 60\mathrm{kJ\ mol^{-1}}$ (*Goldsby and Kohlstedt*, 2001). We impose an isotropic initial fabric on a grid of 20x20x20 crystals at a temperature of -10°C and find a best-fit value of $A_0 = 7.35 \times 10^{-4}\mathrm{Pa^{-2}s^{-1}}$. The effective viscosity for diffusion creep is chosen to be identical to that used by *Barr and Stillman* (2011)

$$\eta_{diff} = \frac{1}{2} \frac{3 R_G T_b d^2}{42 V_m D_{0,v}} \exp\left(Q_V^*/(R_G T)\right) \ . \tag{3.19}$$

Here $V_m = 1.97 \times 10^{-5}\mathrm{m^{-3}}$, $D_{0,v} = 9.10 \times 10^{-4}\mathrm{m^2 s^{-1}}$, $Q_v^* = 59.4\mathrm{kJ/mol}$.

Symbol	Name	Case 1	Case 2
H	Layer Thickness	15 km	75 km
d	Grain Size	0.1 mm	1 mm
$Ra_{1,\text{diff}}$	Basal Rayleigh Number[a]	2.2×10^7	2.6×10^7
ρ	Density	930 kg/m^3	
k	Thermal Conductivity	3.3 W/m/K	
C_p	Specific Heat Capacity	3548 J/kg/K	
α	Thermal expansivity	$10^{-4}/K$	
g	Gravitational Acceleration	1.3 m/s^2	
δT	Initial Temperature Perturbation	15K	

Table 3.1: Summary of model parameters. ([a] *Solomatov*, 1995)

Macroscopic Flow Model

We solve equations for the balance of momentum and mass conservation:

$$\begin{aligned} \rho \frac{\mathrm{D}\mathbf{u}}{\mathrm{D}t} &= -\nabla p + \nabla \cdot \underline{S}^D + \rho \mathbf{g} \ , \\ \nabla \cdot \mathbf{u} &= 0 \ , \end{aligned} \tag{3.20}$$

and advection and diffusion of heat:

$$\rho C_p \frac{DT}{Dt} = \nabla \cdot (k \nabla T) \ , \tag{3.21}$$

with parameters defined in Table 3.1, using a conservative finite difference technique combined with a marker-in-cell approach (*Gerya and Yuen*, 2003) in two spatial dimensions. Each Lagrangian marker carries information about the local fabric (c-axis orientations). The momentum equation is expressed in terms of velocity u:

$$\rho \frac{\mathrm{D}u_i}{\mathrm{D}t} = -\frac{\partial p}{\partial x_i} + \frac{\partial N_{ijkl} D_{kl}}{\partial x_j} + \rho g_i \ , \tag{3.22}$$

where p is pressure, ρ is density, and g_i are the components of gravitation acceleration. Parallelization was necessary even for 2D problems because calculating the polycrystal response for each Lagrangian tracer increases runtime by a factor of 100. The macroscopic flow model uses PETSc (*Balay et al.*, 2012) for domain decomposition and parallel communication. We solved the resulting linear system of equations using the parallel direct solver MUMPS (*Amestoy et al.*, 2001, 2006). After performing resolution tests, we determined that the calculations could be performed on a 41x41 Eulerian grid with 25 Lagrangian markers per cell initially. We eliminated markers if more than 64 were present in one cell using the method described by *Leng and Zhong* (2011) and added markers (using nearest-neighbor interpolation) to any cell containing fewer than 10 markers.

Model Parameters

We ran two-dimensional convection simulations in boxes twice as wide as they are deep. The top and bottom mechanical boundary conditions are free-slip and the lateral boundaries are periodic. The top and bottom are prescribed temperature (Dirichlet) with $T = 100$K and $T = 260$K. In each run, we run the model with the *Goldsby and Kohlstedt* (2001) rheology from an initial sinusoidal perturbation with amplitude $\delta T = 15$K and wavelength equal to the domain width until a steady state, defined by constant Nusselt number (Nu) and root mean square velocity V_{rms} (*Blankenbach et al.*, 1989) and steady flow field, is reached. We then continue the simulation using the micro-macro rheology and an initially uniform isotropic fabric. All of the simulations considered feature a thick stagnant lid overlying a convecting subregion. The two cases that we discuss here are a 75 km-thick layer with a grain size of 1 mm and a 15 km-thick layer with a grain size of 0.1 mm. Other model parameters are listed in Table 3.1.

3.4 Discussion

Depth at which CPO develops

We illustrate the grain-size dependence of fabric strength (deviation from isotropy) in Figure 3.1a. We performed numerical polycrystal deformation experiments with $\sigma_{xx} = -\sigma_{yy} = 10^4$ Pa (all other stress components zero) and $T = 250$K (representative of the warm convecting interior of an ice shell) until a strain of 1.0 was achieved. Next, we characterized the strength of the c-axis fabric using the texture strength $S = \sqrt{< f^2 >}$ (e.g. *Bunge*, 1982) where $f(\theta, \phi)$ is the probability density function of c-axis orientations in the simulated polycrystal. A value of $S = 1.0$ indicates an isotropic fabric while higher values indicate development of CPO. For grain sizes smaller than about 0.1 mm, S is close to 1.0. S increases rapidly between grain sizes of 0.1 and 0.5 mm. In convection problems, Lagrangian tracers experience changing stresses as they are advected through a convection cell, and if macroscopic stress changes faster than crystals within the polycrystal can rotate in response to the applied stress, fabric formation can be limited (e.g. *Castelnau et al.*, 2009).

In order to develop CPO, ice must deform by dislocation creep through strains of at least $\sim 10^{-1}$, with stronger fabrics requiring strains of $O(1)$. Strains of this magnitude are certainly attainable in the convecting interior of an ice shell but are not achieved in the stagnant lid. Figure 3.1b-c shows how stagnant lid thickness varies as a function of $Ra_{1,\mathrm{diff}}$, or equivalently layer thickness (H), based on numerical simulations run to steady-state with the isotropic *Goldsby and Kohlstedt* (2001) rheology. The diffusion creep Rayleigh number is defined as $Ra_{1,\mathrm{diff}} = \rho g \alpha \Delta T H^3/(\kappa \eta_{1,\mathrm{diff}})$ where $\kappa = k/(\rho C_p)$ is thermal diffusivity and $\eta_{1,\mathrm{diff}}$ is the effective viscosity for the diffusion creep deformation mechanism for the temperature and grain size at the base of the ice shell (*Solomatov*, 1995; *Barr et al.*, 2004). We indicate the minimum layer thickness for which convection is possible for our model geometry and amplitude of initial temperature perturbation δT with vertical dashed lines

in Figure 3.1b-c. The thickness δ_0 of the stagnant lid can be viewed as a lower bound on the depth at which texture will develop in our simulations. Figure 3.2 shows fabrics that develop in our simulations at several depths beneath the surface. When grain size is small (0.1 mm), diffusion creep allows relatively thin ice shells to convect, but because deformation is not accommodated by dislocation creep, CPO does not develop anywhere in the ice shell, illustrated in Figure 3.3. If grain size is larger (1.0 mm) diffusion creep is sluggish, allowing CPO to form in the convecting interior of the ice shell (Figure 3.3).

Effects on flow field and heat transfer

The anisotropic viscosity resulting from texture development has a first order effect on the velocity in upwellings and downwellings (Figure 3.4). The more rapid flow is in agreement with studies of the effects of anisotropic viscosity on ice sheets (*Mangeney et al.*, 1996). We calculated dynamic topography using the normal stress exerted on the upper boundary of the domain with and without texture development (Figure 3.4). There is negligible difference between the two simulations because, despite differences in velocity in the convecting interior, the stresses driving convection are very similar.

Because it affects the velocities in upwellings and downwellings, it is expected that viscous anisotropy will affect heat transport. The steady-state Nusselt number achieved using the *Goldsby and Kohlstedt* (2001) rheology for Case 2 (75 km thickness) was 1.77. After enabling texture development and anisotropy, we ran the simulation for 6 Ma, at which time the Nusselt number had reached 1.94. The Nusselt number between the activation of texture development and the end of the simulation can be well-approximated ($R^2 = 0.9999$) as an exponential function of time with the form $Nu(t) = a\exp(-bt) + c$. The term $c = 1.949 \pm 0.001$ is the expected steady-state value of Nu (with 95% confidence bounds). Thus, the state achieved during our run had Nusselt number within 0.5% of the steady-state value predicted by exponential extrapolation, and the anisotropic model transports 10% more heat by convection than the isotropic model. We computed a steady Nu for anisotropic Case 1 of 1.746 ± 0.001, an increase of 5% relative to the value of 1.67 computed for the isotropic case. We expect enhanced heat transport for larger grain sizes because dislocation creep is more rapid at the smaller grain size used in Case 1. Although convective heat transport is significantly enhanced in our model, the general uncertainty in grain size and amount of internal heating leads to much larger variations in heat transport (e.g. *Ruiz et al.*, 2007).

Detectability

Fabric development in an ice mantle would most interesting if it produced an observable signature. Detection of CPO would imply past or ongoing deformation accommodated by specific creep mechanisms, which would in turn provide insight into thermal and tectonic evolution, including constraints on grain size, stress magnitude and orientation, and strain history. A spacecraft carrying ice-penetrating radar can in principle measure preferred orientation remotely (*Barr and Stillman*, 2011). The radar planned for ESA's JUICE spacecraft,

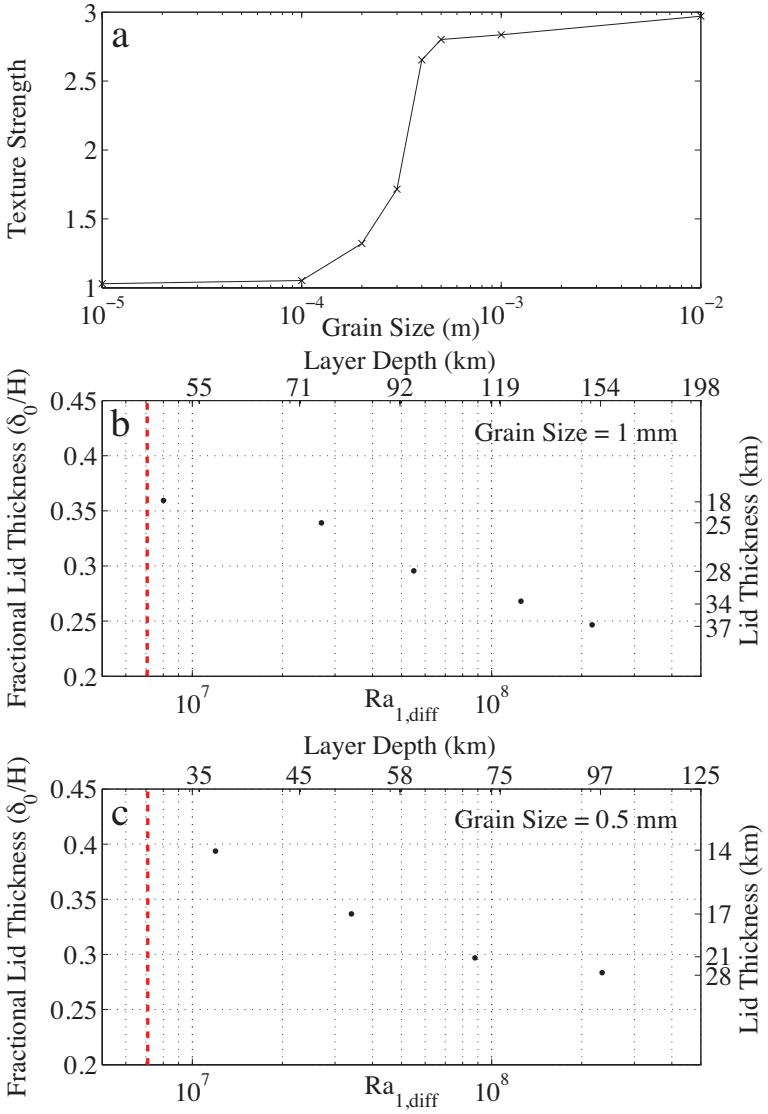

Figure 3.1: (a) Texture Strength (S, defined in text) increases rapidly between grain sizes of 10^{-4} and 10^{-3} m. (b) Stagnant lid thickness calculated from numerical experiments vs. $Ra_{1,\mathrm{diff}}$ (or equivalently layer thickness) for a grain size of 1.0 mm and (c) for a grain size of 0.5 mm. Vertical red line indicates the critical layer thickness for convection to occur, calculated using a bisection method.

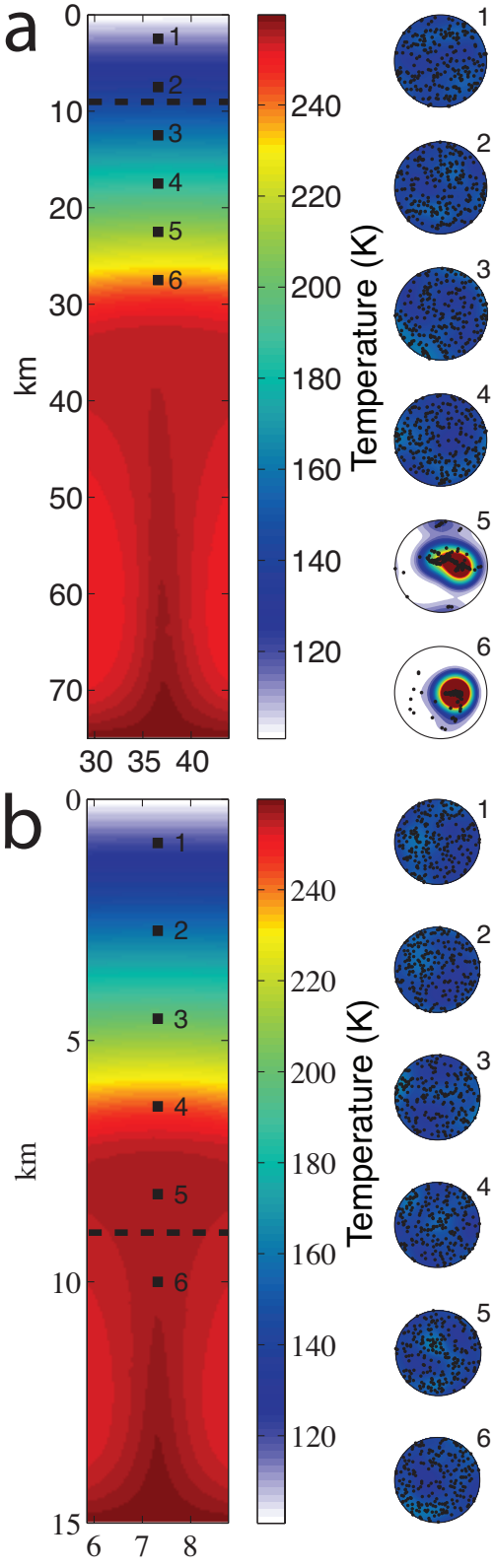

Figure 3.2: CPO fabrics calculated for locations marked by numbered squares, corresponding to numbered pole figures (right). Warmer colors in the pole figures indicate higher concentrations of c-axes. Horizontal dashed lines indicate the maximum depth (9 km) to which the proposed ice-penetrating radar on the ESA Juice spacecraft may penetrate. (a) Layer thickness of 75 km, grain size 1.0 mm (b) Layer thickness 15 km, grain size 0.1 mm.

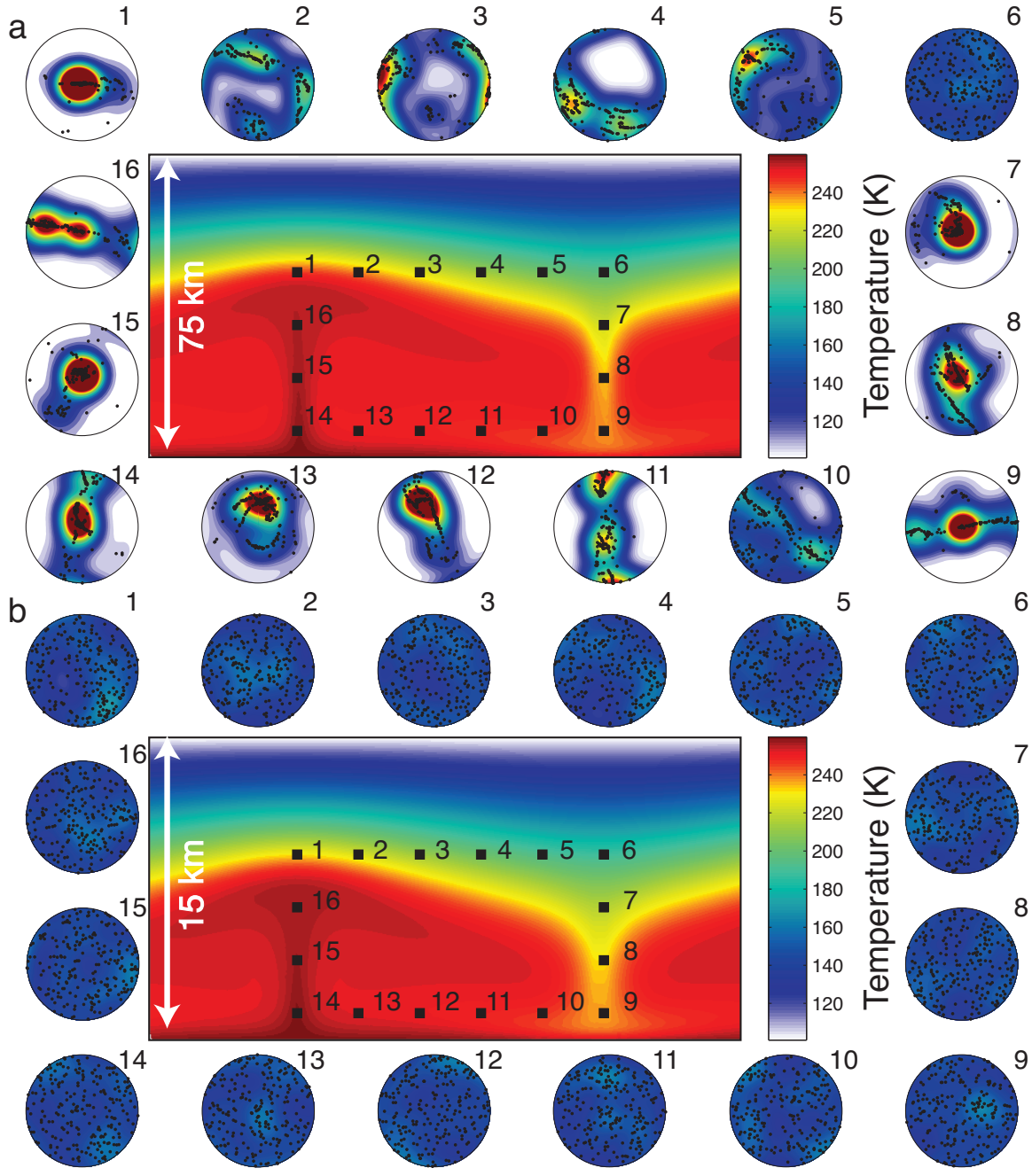

Figure 3.3: CPO fabrics calculated for locations marked by numbered squares in the convecting interior of the ice layer. (a) Layer thickness of 75 km, grain size 1.0 mm (b) Layer thickness 15 km, grain size 0.1 mm.

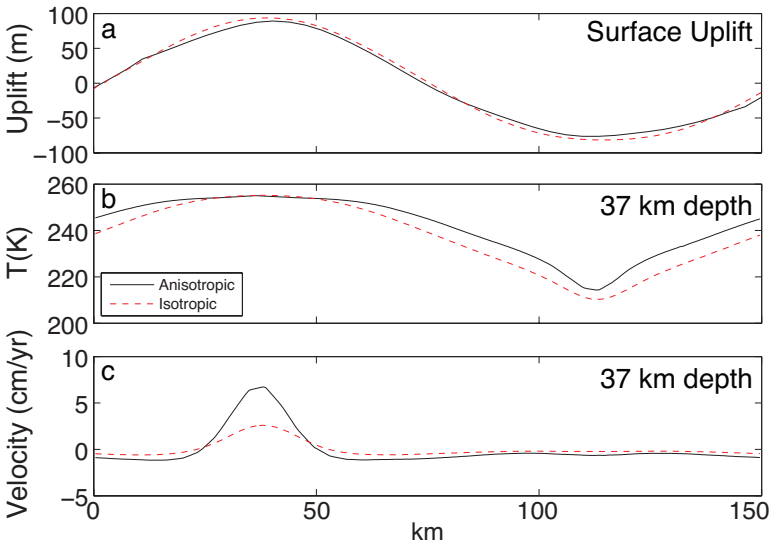

Figure 3.4: (a) Profiles of surface uplift (dynamic topography) for case with layer thickness 75km and grain size $d = 1.0$mm with (black line) and without (dashed red line) anisotropy. (b) Temperature profiles at a depth of 37 km. (c) Velocity profiles at a depth of 37 km.

likely the next mission to the Jovian system, is expected to be able to probe depths 100m to 6-9 km below the surface. With a grain size of 1.0 mm, the minimum stagnant lid thickness in our isotropic simulations was 18 km (Figure 3.1b). With somewhat smaller grain size (0.5 mm), some CPO development may be possible (though lower texture strength is expected) and stagnant lids as thin as 14 km may develop (Figure 3.1c). The stagnant lid in Case 2 (75km thickness, 1.0 mm grain size) and each of the simulations shown in Figure 3.1b-c are sufficiently thick to preclude radar detection of CPO in the convecting interior. JUICE is expected to perform flybys of Europa and Callisto before entering orbit around Ganymede. Our calculations were performed with Europa-like $g = 1.3\text{m/s}^2$, but Ganymede and Callisto both have g within 10% of Europa. Because Ra is linearly proportional to g, we expect our results to be applicable to all three bodies. However, other processes not accounted for in this study could affect stagnant lid thickness, allowing texture to develop at depths where it could be detectable. In particular, plastic yielding can lead to episodic overturn of the stagnant lid (*Showman and Han*, 2005). During overturn events, ice with CPO could be exhumed and the depth at which CPO develops could be reduced. Frictional heating on faults could lead to local temperature variations and hence localized CPO development at shallow depths (*Nimmo*, 2002; *Nimmo et al.*, 2007). Internal heating by tidal dissipation could thin the stagnant lid globally, bringing CPO development nearer to the surface [*Solomatov and Moresi* 2000, Figure 2 of *Nimmo and Manga* 2002]. Regardless of depth of formation, Figure 3.1a shows that deformation of polycrystalline ice with grain size >0.5 mm through strains $O(1)$ should produce CPO, and if this does occur within a few km of the surface of an icy moon, CPO may be remotely detected.

Acknowledgments

Computational resources were provided through the Texas Advanced Computing Center under Teragrid allocation EAR-100032 to M.L.R., by David A. Yuen through the Minnesota Supercomputing Institute, and by Bruce Buffett. We thank the editor, Francis Nimmo, and Allen McNamara, and an anonymous reviewer for their comments which improved the quality of the manuscript. We thank T. Becker, K. Cuffey, G. Hirth, and D. Kohlstedt for helpful discussions.

Chapter 4

Response of Mud Volcanoes to the April 4, 2010 El Mayor-Cucapah Earthquake

4.1 Abstract

Mud volcanoes sometimes respond to earthquakes, but the mechanisms by which earthquakes trigger changes in ongoing eruptions or initiate new eruptions are not completely understood. We measured gas discharge at a field of mud volcanoes near the Salton Sea, Southern California before and after the April 4, 2010 El Mayor-Cucapah Earthquake and observed an increase in gas flux immediately following the earthquake and a subsequent recovery to pre-earthquake values. This earthquake-eruption pair is of particular interest because the earthquake produced large strains, up to 1.2%, near the mud volcano location, allowing us to test two competing triggering mechanisms: (1) shaking-induced bubble mobilization, and (2) permeability enhancement. We measured the rheology of erupted mud from the mud volcanoes to quantify the importance of mechanism (1) and found that this mechanism is unlikely to be important. We therefore favor the explanation that the increased gas flux was caused by a transient increase in permeability.

4.2 Introduction

Earthquakes induce a wide range of hydrologic responses including water level changes in wells, changes in spring discharge and stream flow (e.g. *Muir-Wood and King*, 1993), changes in permeability (e.g. *Elkhoury et al.*, 2006), and changes in the interval between eruptions of geysers (e.g. *Husen et al.*, 2004). Mud volcanoes also respond to earthquakes (e.g *Mellors et al.*, 2007), and their responses may have hydrologic origins. Although hydrologic responses to earthquakes have been documented for thousands of years, the mechanisms responsible for the responses and their possible relationship to triggering processes remain, in general, not well understood.

Lynch and Hudnut (2008) describe a system of mud volcanoes, mound springs, and mud pots in the Imperial Valley, California, which are the focus of this study. The Imperial Valley mud volcanoes, located at the intersection of Davis and Schrimpf roads near Niland, CA, are particularly interesting in that they lie on the southeastern extension of the San Andreas Fault (Figure 4.1) and thus their behavior might provide some insight into fault-zone permeability. The response of the small Imperial Valley mud volcanoes to earthquakes may also provide some insight into the response of larger mud volcanoes that have responded to earthquakes in the past (e.g. *Chigira and Tanaka*, 1997; *Mellors et al.*, 2007; *Bonini*, 2009a; *Manga and Brodsky*, 2006).

We carried out field work in the Imperial Valley on March 13, 2010, March 21, 2010, April 6, 2010, and May 12, 2010. The timing of the April 4, 2010 M_W 7.2 El Mayor-Cucapah event was serendipitous in that we were able to make measurements in a short period of time both before and after the event. During each field campaign, we measured temperature in mud volcanoes and surrounding springs and gas seeps, measured gas discharge where possible, documented the presence of fresh eruptive deposits, and sampled mud for rheological measurements. Our field observations indicate that there was a post-seismic

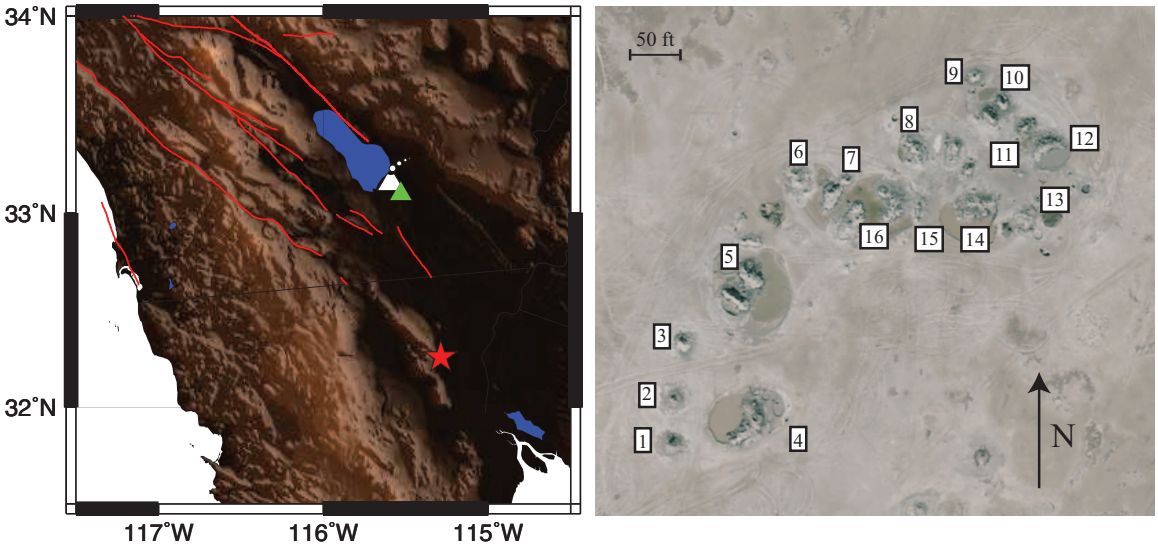

Figure 4.1: Map of study location, showing major faults in red (left). Red star (left) indicates epicenter of El Mayor-Cucapah event. Green triangle indicates location of Wildlife Liquefaction Array (WLA). White triangle (left) indicates location of mud volcanoes, seen in an aerial photograph (right) at intersection of Davis and Schrimpf roads near Niland, CA.

increase in gas discharge and eruptive activity at the mud volcanoes. Theory, laboratory measurements of mud rheology, and field observations indicate that transient permeability enhancement is the most plausible mechanism to explain the changes in eruptive activity.

4.3 Background

Davis-Schrimpf mud volcanoes

Kopf (2002) defines a mud volcano as a surface expression of mud that originated at depth. The Davis-Schrimpf mud volcanoes are pictured in Figure 4.2. The small stature of the mud volcanoes in the Imperial Valley (less then 5 m) categorizes them as "mud lumps" (*Kopf*, 2002) and *Svensen et al.* (2009) have labeled them "hydrothermal seeps," in part because there is very little net exhumation of mud from the subsurface. We will nevertheless continue to refer to these constructional, steep-flanked features as mud volcanoes, and note that *Bonini* (2009b) used the same terminology to describe morphologically similar features in the Northern Apennines.

The Davis-Schrimpf mud volcanoes considered here are surface expressions of the Salton Sea Geothermal System (SSGS), an area of active geothermal power production (*Bertani*, 2005) and past commercial CO_2 extraction (*Muffler and White*, 1969). The near-surface geotherm in the SSGS is exceptionally steep. *Helgeson* (1968) reported temperatures as

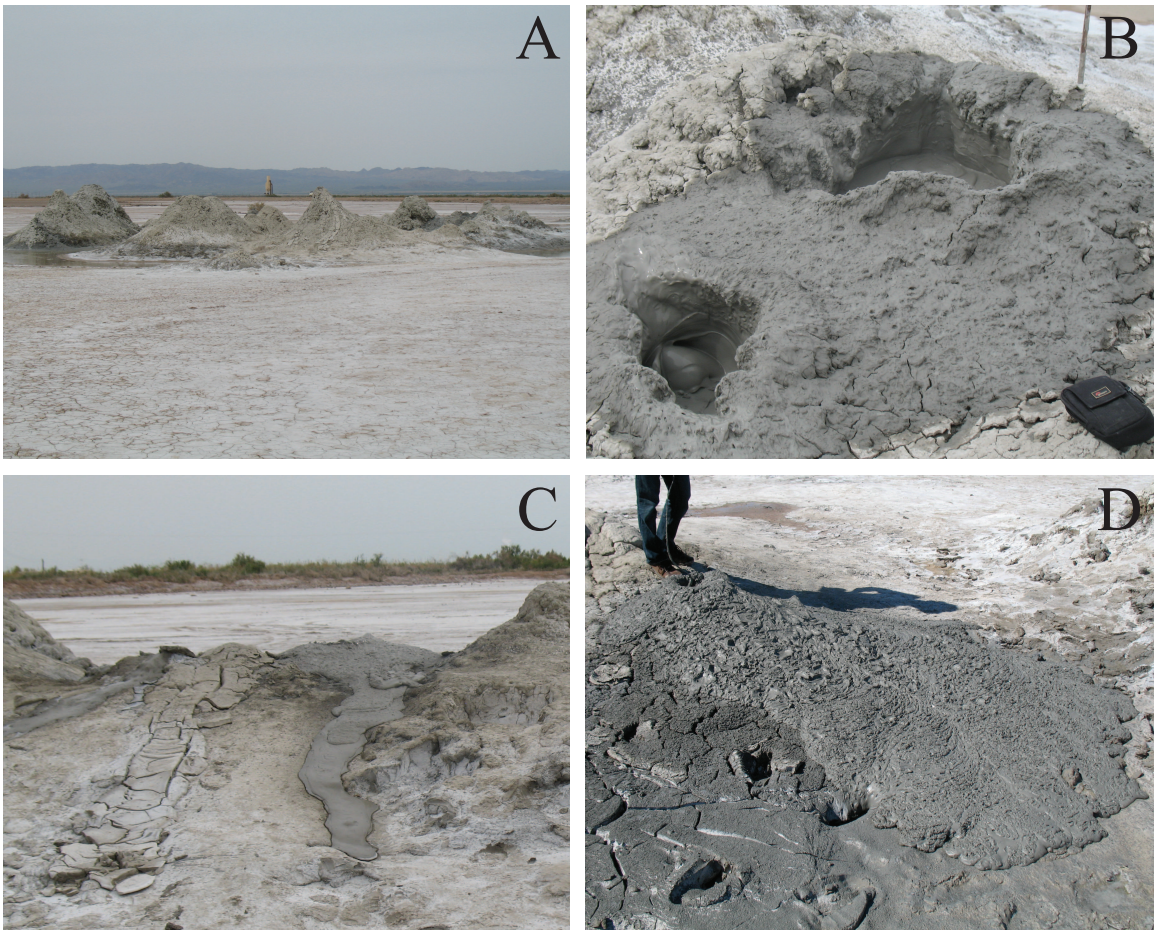

Figure 4.2: (A) Field of mud volcanoes at the Davis-Schrimpf location. (B) Some of the mud volcanoes have craters filled with bubbling mud, as seen in this picture. (C) The dry mud flow on the left was active on 3/13/2010 but completely dry by 3/20/2010, the date of this photo. The flow to the right was active at the time of the photograph. (D) Very large, fresh flow seen on 4/6/2010. Thermistor probe is in the vent at upper left, where we measured a gas flux of 22 LPM.

high as 300°C at 3000 ft (914 m), and heat flow in the area can reach 1200 mW m^{-2} (*Elders and Sass*, 1988). The temperature profile through the SSGS reservoir is isothermal, owing to convection. *Williams and McKibben* (1989) suggest that the intersection between near-surface conductive and deeper convective geotherms results from a stably stratified brine interface rather than a lithologic (permeability) contrast, the interpretation favored by previous authors (e.g. *Helgeson*, 1968; *Younker et al.*, 1982; *Randall*, 1974). The SSGS is contained within a 6000 m-thick sequence of sedimentary rocks, the uppermost ∼200m of which is composed of unconsolidated lacustrine and Colorado River deltaic sediments (*Younker et al.*, 1982). These sediments are underlain by evaporite deposits. The near-surface strata appear to be the source of the erupting mud, whereas the CO_2 is believed to come from greater depths (*Robinson et al.*, 1976; *Svensen et al.*, 2007), where it is produced through metamorphic decarbonation reactions at temperatures of at least 125°C (*Muffler and White*, 1969). The details of the subsurface gas and mud plumbing system are not fully understood, but two possible configurations based on *Svensen et al.* (2009) are depicted in Figure 4.3. Regardless of its depth of production, CO_2 is present at shallower depths; *Kelley and Soske* (1936) note that CO_2 extraction wells were drilled in the late 1920s to a producing horizon between 400 and 500 ft (123 and 152 m) where pressures were between 200 and 300 psi (1.4-2.1 MPa), somewhat in excess of hydrostatic pressure at these depths.

Sturz et al. (1992) visited the Davis-Schrimpf mud volcanoes in 1985, 1991, and 1992 and measured mud temperatures between 18 and 32°C and mud composition (45-70% smectite, 20-35% illite, 10-20% kaolinite). *Svensen et al.* (2009) deployed temperature probes in two of the Davis-Schrimpf mud volcanoes and two pools adjoining the volcanoes between December 18, 2006 and March 19, 2007. This deployment helped establish the recent natural temperature variability inside the mud volcanoes and demonstrated that there is no correlation between temperature changes and tidal forcing. The minimum temperature recorded by *Svensen et al.* (2009) was 37.3°C, the highest recorded temperature was 69.7 °C, and the standard deviations were 4.0 and 6.4 °C for the two features instrumented. There were no earthquakes of sufficient size during the deployment of *Svensen et al.* (2009) to produce changes in temperature at the mud volcanoes. Although the temperatures measured by *Sturz et al.* (1992) are remarkably lower than those measured by *Svensen et al.* (2009), we cannot speculate as to whether there was a general trend in the mud volcanoes' temperature between 1992 and 2006.

Response to earthquakes

Like other hydrologic features, mud volcanoes sometimes respond to earthquakes. *Mellors et al.* (2007) found that large mud volcano eruptions in Azerbaijan occur in the two days following a major earthquake more often than would be expected by chance. *Bonini* (2009a) identified several earthquake-eruption pairs among documented eruptions of Sicilian mud volcanoes. Mud volcanoes (*solfataras*) very similar in appearance to the Davis-Schrimpf mud volcanoes near Volcano Lake, Mexico and associated with the Cerro Prieto geothermal field (*Randall*, 1974) responded to the 1915 Imperial Valley Earthquake (*Beal*, 1915) and to

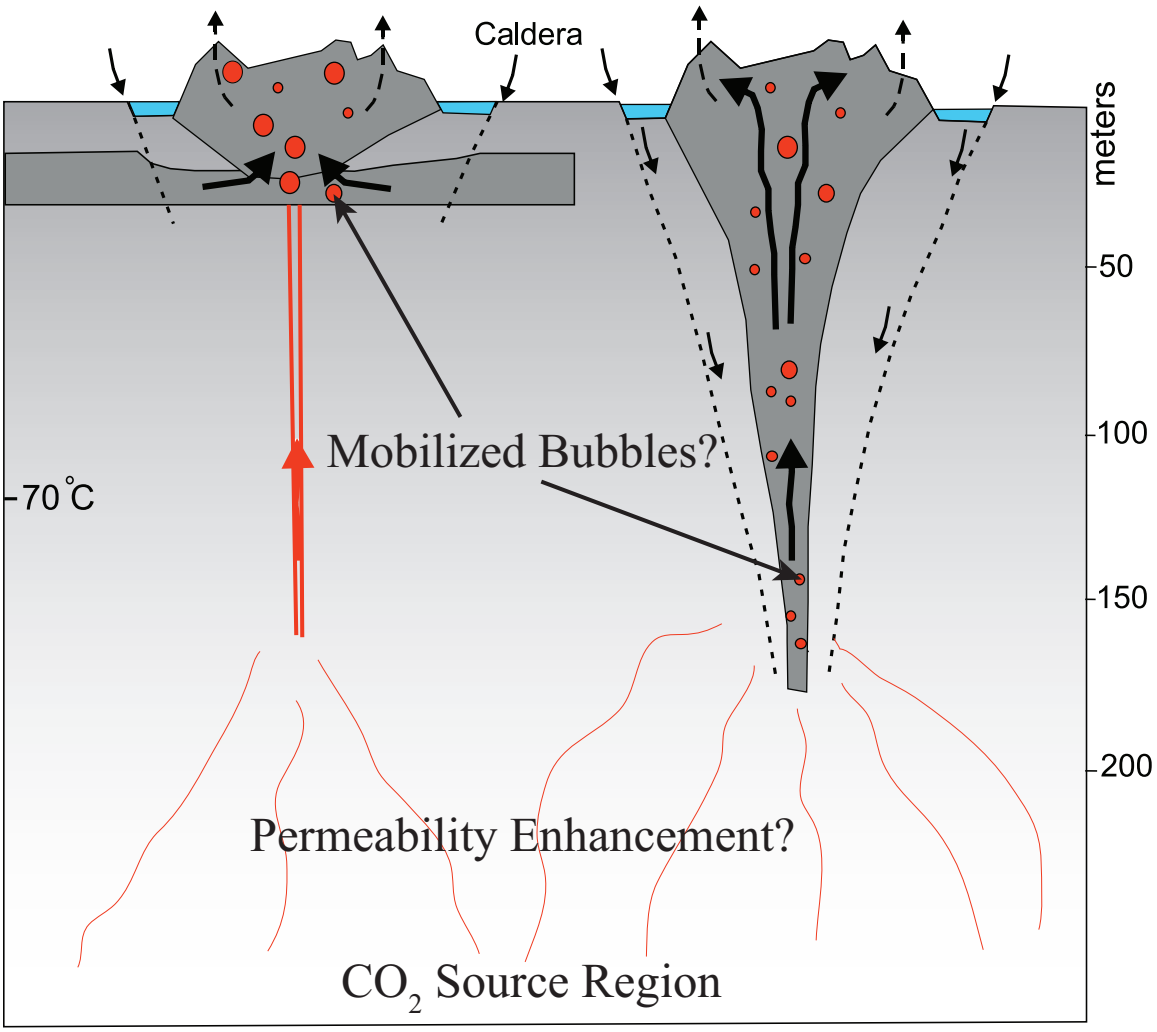

Figure 4.3: Schematic of two possible mud volcano plumbing systems, modified from *Svensen et al.* (2009). CO_2 (red bubbles and pathways) is produced at depth in the Salton Sea Geothermal System (SSGS) and travels upward through a porous reservoir. The uppermost 200m of the system consist of Colorado River deltaic and lacustrine deposits, the source of the erupting mud. The dark arrows indicate the path travelled by mud as it is recycled during mud volcano construction and collapse. Of the two scenarios depicted, *Svensen et al.* (2009) favored the model on the right.

the November 29, 1852 Fort Yuma event (*Townley and Allen*, 1939). The response of these mud volcanoes to shaking was accompanied by other dramatic hydrologic responses. The 1852 Fort Yuma event triggered the eruption of a geyser near Volcano Lake whose plume reached an elevation of 800-1000 ft (244-205 m) (*Balderman et al.*, 1978).

El Mayor-Cucapah Earthquake

The April 4, 2010 El Mayor-Cucapah earthquake occurred on the Laguna Salada fault system in Northern Mexico. Rupture propagated unilaterally northeastward to a terminus near the Mexico-California border, producing enhanced shaking in the Salton Trough (*Hudnut et al.*, 2010). The event accommodated both east-down and right-lateral slip along the Pacific-North American plate boundary. The earthquake was accompanied by extensive surface rupture and liquefaction was widespread in the near field (*King et al.*, 2010; *Pridmore et al.*, 2010). Well-level responses were common throughout the Western United States (Figure 4.4).

4.4 Methods

We measured temperature at each of the mud volcanoes using a thermistor and gas discharge using a funnel (22 cm diameter) connected to Cole-Parmer gas flowmeters. The stated accuracy of the flowmeters is $\pm 5\%$ and repeatability is $\pm 0.5\%$. We used the same equipment and employed the same division of labor (placing funnel, taking measurements) on each field trip. Our best estimate of the human error associated with reading the gas flow meters is ± 0.5 LPM for measured fluxes less than or equal to 10 LPM and ± 5 LPM for fluxes greater than 10 LPM.

We used a Haake Rheoscope-1 cone-plate rheometer to characterize the material properties of mud collected from the vents of four of the Davis-Schrimpf mud volcanoes. The cone has a diameter of 60 mm with a bevel angle of 4° and a minimum gap thickness of 139 μm, larger than the particle size of the mud (Figure 4.5). The mud was stored in two layers of gas-impermeable plastic bag between sample collection and analysis to minimize desiccation and refrigerated to retard any chemical reactions. We measured the response of mud under steady shear and oscillatory shear. In the steady shear experiments, we loaded the mud samples, measured yield strength and measured the applied stress as a function of strain rate. We measured yield strength using a method suggested by *Dubash and Frigaard* (2007), whereby constant stress was applied for 120 seconds and the total strain at the end of this period was recorded. In the oscillatory shear experiments, we loaded the samples, pre-sheared them for 10 seconds at a strain rate of 1 s^{-1}, and then deformed them under oscillatory shear at fixed frequencies of 0.2, 1.0, and 10 Hz while controlling strain amplitude between 10^{-4} and 10^{-2}. These strain amplitudes and frequencies are comparable to those imposed by earthquakes, discussed later and shown in Figure 4.6. For each data point in the oscillatory shear experiments, the sample was pre-sheared for 3 cycles and then measure-

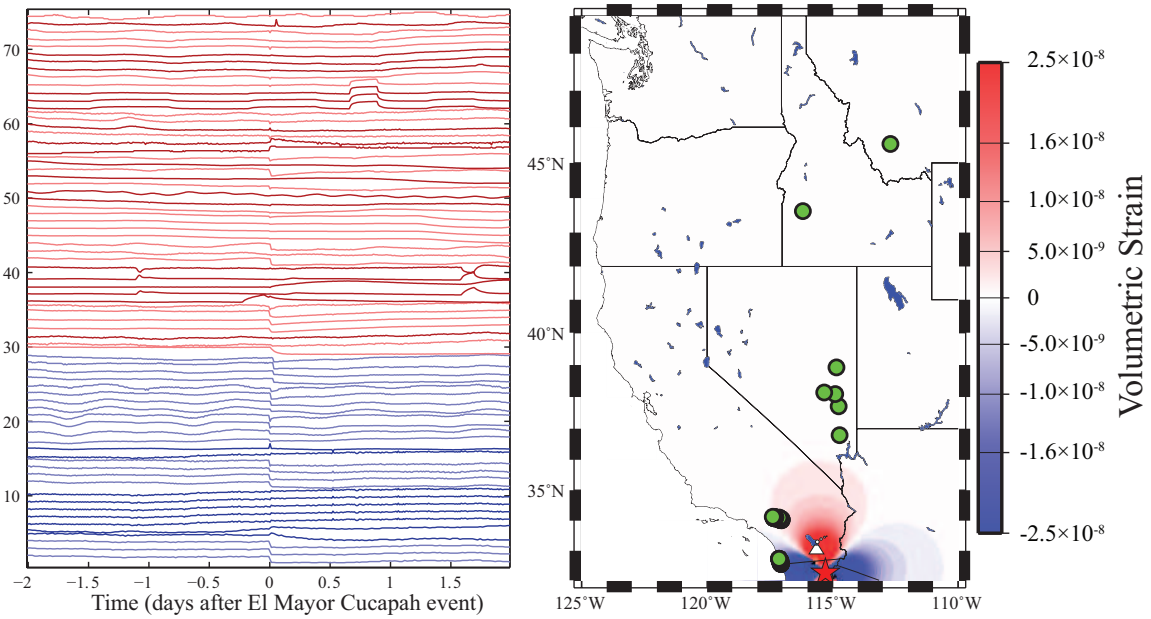

Figure 4.4: (right) Map indicating location of wells in the Western United States (green circles) that responded to the El Mayor-Cucapah earthquake (red star marks epicenter). Background field is dilatation: red and blue represent expansion and contraction, respectively. (left) Water level records (distance below surface) in wells that showed a response. Each well's record has been normalized with respect to its maximum absolute value in the time interval plotted. Zero time corresponds to time of El Mayor-Cucapah event. Water level records are sorted bottom to top in order of increasing epicentral distance, and color indicates whether the well experienced contraction (blue) or expansion (red). Darker colors indicate a record that showed a decrease in water level (increase in distance below surface), lighter colors indicate an increase in water level. There does not appear to be a correlation between the sign of the volumetric strain and the sign of the change in water level.

ments were averaged over 5 cycles. The oscillatory strain experiments allow us to measure the storage and loss moduli of the mud, assuming that it behaves as a Maxwell viscoelastic material. We also retained the raw data for stress and strain as a function of time, which allowed us to confirm that the Maxwell model was appropriate. The equipment and methodology used here is identical to that used in *Sumita and Manga* (2008) and was also used to characterize mud erupted from the Sidoarjo mud flow in Indonesia (*Manga et al.*, 2009).

We obtained waveforms for the El Mayor-Cucapah event at the Wildlife Liquefaction Array (WLA, location indicated by green triangle in Figure 4.1), which, at 12.3 km, is the closest strong motion seismometer to the Davis-Schrimpf location. Waveforms (Figure 4.6) were obtained from IRIS for two accelerometers at the WLA site - a borehole instrument at a depth of 100m and a surface instrument. We removed the mean from, de-trended, and then integrated the seismograms to obtain displacement time series. We applied a high-pass filter

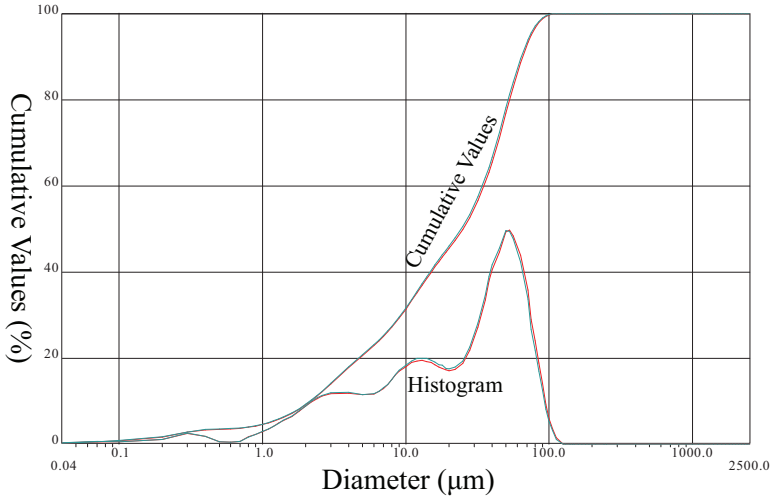

Figure 4.5: Measured particle size in mud from Davis-Schrimpf mud volcano 12. Blue and red curves show two measurement runs of the same sample. Particle diameters representing the 10th, 50th, and 90th percentiles of the cumulative particle size distribution are D_{10}=2.13 μm, D_{50}=24.31μm, D_{90}=63.81 μm.

with a pass band above 0.02 Hz to remove spurious long-period signals. Shear strain can be approximated from peak ground velocity using the empirical relationship $\gamma \sim (\mathrm{PGV})/V_S$ or from peak ground acceleration using $\gamma \sim 1.2z(\mathrm{PGA})/V_S^2$ (*Wang et al.*, 2003). Assuming V_S = 500 m/s (typical of unconsolidated sediments), both of these scaling relations yield estimates for γ on the order of 1%. We also computed displacement gradients ($\partial u_{Radial}/\partial z$ and $\partial u_{Tangential}/\partial z$) directly using the surface and 100 m-depth records and found a peak shear strain of 1.2% (Figure 4.6), in good agreement with the scaling relationships. Displacement gradients computed with this method place a lower bound on the true displacement gradient.

We used Coulomb version 3.1.09 (*Lin and Stein*, 2004; *Toda et al.*, 2005) to calculate volumetric strain associated with the earthquake using the moment tensor solution from the Global CMT Project's catalog (globalcmt.org, *Dziewonski et al.*, 1981) and fault geometry from the empirical scaling of *Wells and Coppersmith* (1994).

The United States Geological Survey (USGS) maintains monitoring stations for ground water table in several locations, mostly near major cities, in the western United States. We compiled all of the well water-level data for Arizona, California, Colorado, Idaho, Montana, Nevada, Oregon, Utah, and Washington and searched manually for a response coincident in time with the El Mayor-Cucapah event. Of the 154 records obtained, 63 showed a response (well locations and responses shown in Figure 4.4). Most of the wells have a sampling interval of 15 minutes except for several that record only twice per hour. The most distant well that showed a response was 1749 km from the epicenter.

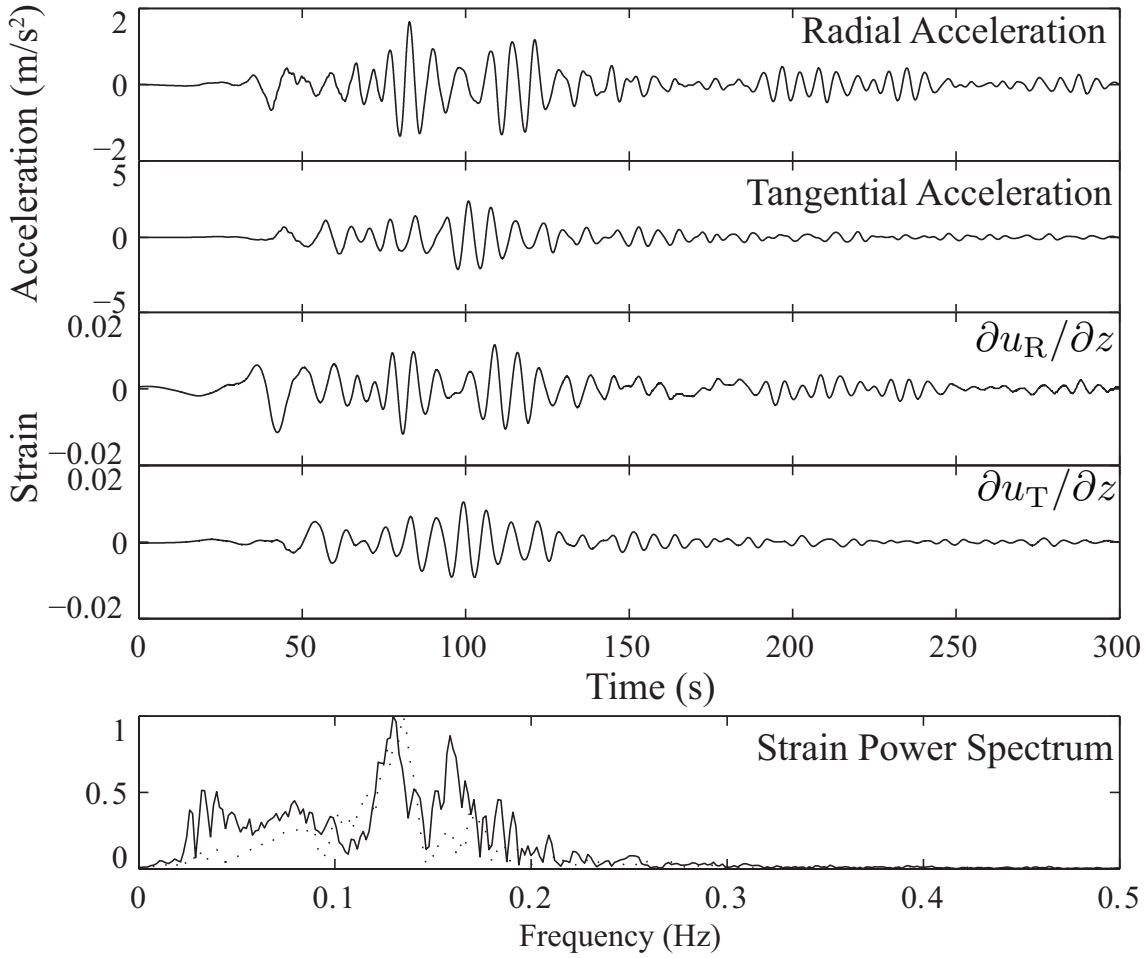

Figure 4.6: Waveforms from Wildlife Liquefaction Array (green triangle in Figure 4.1), 100 m depth, for El Mayor-Cucapah event. Shear strain in the uppermost 100 m reached a maximum value of 1.2%. Two strain power spectra are plotted: radial (solid line) and transverse (dashed line).

4.5 Results

Field measurements

We measured gas flow at 5 features on 3/13/2010, 8 features on 3/20/2010, 18 locations on 4/6/2010, and 12 locations on 5/12/2010. The average flow per measurement was 7.0 liters per minute (LPM), 7.6 LPM, 12.5 LPM, and 9.5 LPM, respectively with standard deviations of 2 LPM, 1.35 LPM, 5.3 LPM, and 3.3 LPM, respectively. Figure 4.7 is a compilation of our gas flux measurements (tabulated in the electronic supplement), showing increased gas flux on 4/6/2010. The increase in gas flux is the most robust evidence for a post-seismic response at the mud volcanoes. The pathways through which gas escapes appear to be stable over the time period of our study, although this is clearly not the case over year-to-decadal time scales (*Sturz et al.*, 1992). Estimating the total change in gas flux following the earthquake is difficult because some gas discharge locations became dangerous or otherwise inaccessible due to the changing depth of pools and re-configuration of crater rim material. Therefore, we believe that the change in average discharge per measurement site is the best proxy for increased gas flux.

We measured temperature at 14 mud volcano vents on 3/13/2010, 7 on 3/20/2010, 16 on 4/6/2010, and 12 on 5/12/2010. The average temperatures were 44.0°, 56°, 46.6°, and 56.9° with standard deviations of 11.0°, 5.6°, 11.8°, and 8.6°. Figure 4.7 is a compilation of all of the temperature measurements, which are also available in the electronic supplement. There is no discernible post-seismic temperature response and all of the values measured are within 3 degrees of the range documented by *Svensen et al.* (2009) and *Sturz et al.* (1992).

In addition to the quantitative measures of gas flux and temperature, we also noted the number of fresh flow features. We can roughly constrain the age of surface flows based on appearance; Flows that were active on 3/13/2010 and inactive on 3/20/2010 no longer had moist surfaces. We observed four fresh flows on 3/13/2010, four on 3/20/2010 eight on 4/6/2010, and five on 5/12/2010. The flows observed on 4/6/2010 included one that had erupted from a new vent, at which we also measured a gas flux of 22 LPM, more than twice the largest pre-earthquake value at any vent. This vent was extinct on 5/12/2010, with no measurable or audible gas flux.

Laboratory measurements

We had the grain size distribution in five of our samples measured using a CILAS 1190LD tri-laser particle size analyzer. We chose three samples from the same crater of mud volcano 12 (Figure 4.1), collected on 3/13/2010, 3/20/2010, and 4/6/2010 and two atypical samples, one from a very low viscosity pool on 4/6/2010 and a second from the interior of a large, fresh mud flow on 4/6/2010. The samples were placed in an ultrasonicator for 60 seconds prior to measurement and were ultrasonicated continuously during measurement to minimize agglomeration. The grain size distribution, shown in Figure 4.5, was very consistent among the mud volcanoes. The average 50th percentile particle diameter is 24.31 μm and the peak

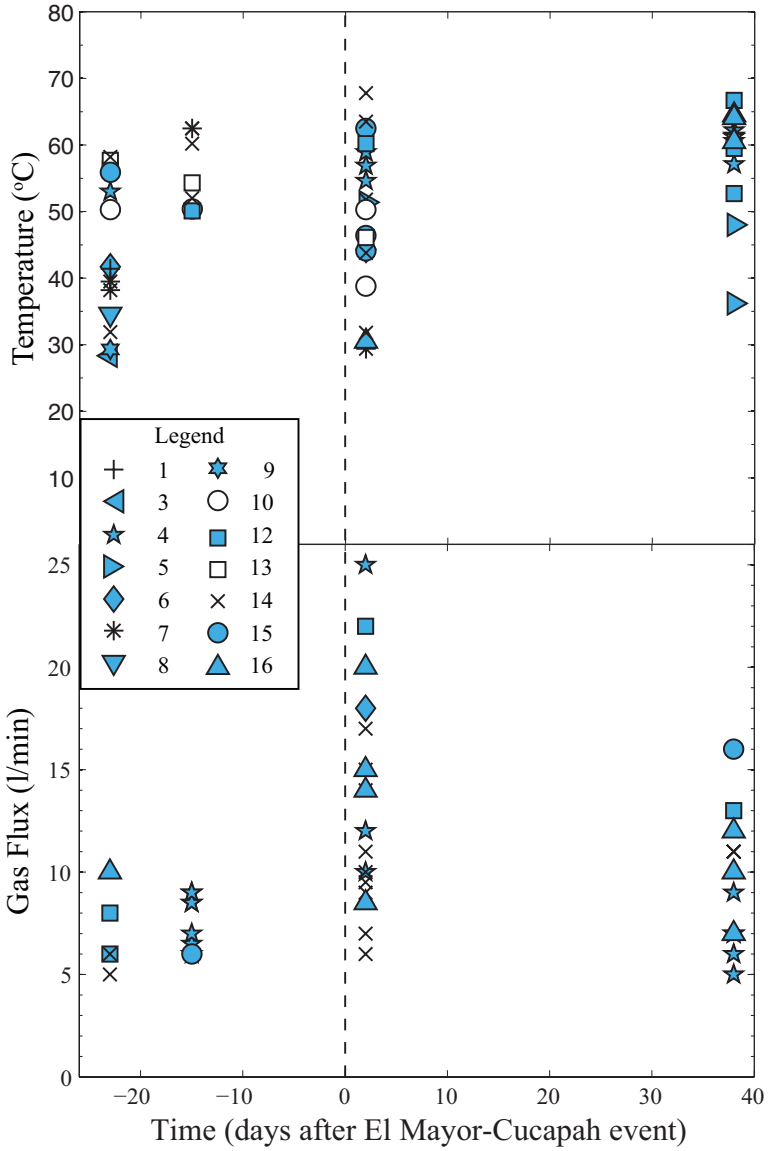

Figure 4.7: Compilation of temperature (top) and gas flux (bottom) measurements made at Davis-Schrimpf mud volcanoes as a function of time. Symbols correspond to individual mud volcanoes, as numbered in Figure 4.1. The vertical dashed line indicates the time at which the El Mayor-Cucapah event occurred. Repeated glyphs on a given day indicate that there were multiple active vents on the mud volcano and each glyph corresponds to a measurement made at one of the vents. The mean gas flux increased by about 70% and the maximum gas flux was 150% larger than any pre-earthquake value. We cannot discern any seismic response in the temperature data.

of the grain size distribution is consistently about 50 μm among all of the samples. We measured the water content of each of the samples for which we analyzed grain size. The large, fresh mud flow had the lowest water content, 33% by mass, the low-viscosity pool had the highest, 48%, and the mud in the craters was on average 40% water with a standard deviation of 1% among six samples.

Our analyses of the erupted muds from the Davis-Schrimpf mud volcanoes indicate that the mud has a yield strength of 52 Pa at 40 wt% H_2O and 294 Pa at 33 wt% H_2O and is shear thinning (Figure 4.8A). The unidirectional shear experiments produced measurements of effective viscosity that are well approximated by the empirical relationship:

$$\begin{aligned} \mu &= 10^{1.8}\dot{\epsilon}^{-0.82} \text{ (40 wt\% } H_2O\text{)} \\ \mu &= 10^{2.3}\dot{\epsilon}^{-0.83} \text{ (33 wt\% } H_2O\text{)} \end{aligned} \tag{4.1}$$

where μ has units of Pa-s and $\dot{\epsilon}$ has units s^{-1}. Figure 4.8B shows the viscosity measurements for both samples. Under oscillatory shear, the mud experiences a reduction of strength at shear strains between 10^{-3} and 10^{-2} irrespective of frequency (Figure 4.8C), similar to mud from the Sidoarjo mud flow (*Manga et al.*, 2009).

We used X-ray diffraction to measure the composition of two mud samples. We identified the minerals kaolinite, muscovite, montmorillonite, dolomite, calcite, and albite in both of the mud samples. One of the samples contained orthoclase. We were unable to measure the relative abundances of the various minerals present using this technique.

4.6 Discussion

The epicenter of the El Mayor-Cucapah earthquake was 96.6 km from the mud volcano location. Figure 4.9 shows that this earthquake was close enough that a mud volcano response is not unexpected based on empirical magnitude-distance-triggering relationships developed for mud volcanoes and other hydrologic features (*Wang and Manga*, 2010). Our field observations show that the mud volcanoes did respond to the El Mayor-Cucapah earthquake. To demonstrate statistically that a response occurred, we divide the gas flux measurements into two groups: (1) data from 4/6/2010 and (2) all other data. We wish to ascertain whether the mean or median of group 1 is significantly different from group 2. We used the Shapiro-Wilk test of normality (*Shapiro et al.*, 1968) and found that we could reject the null hypothesis that the data is normally distributed. Because both datasets are not normally distributed, we chose to use the Mann-Whitney U-test (*Hollander and Wolfe*, 1999, p. 125), the result of which allows us to reject the null hypothesis that the two groups are independent samples of identical distributions with equal medians at the $\alpha = 0.01$ significance level. We now turn our attention to the mechanism responsible for this response.

Manga et al. (2009) reviewed possible triggering mechanisms: (1) volumetric changes due to static stress transfer (*Walter and Amelung*, 2007), (2) dilatancy (*Wang et al.*, 2001), (3) liquefaction (*Wang*, 2007), (4) destabilization of gas hydrates (*Obzhirov et al.*, 2004;

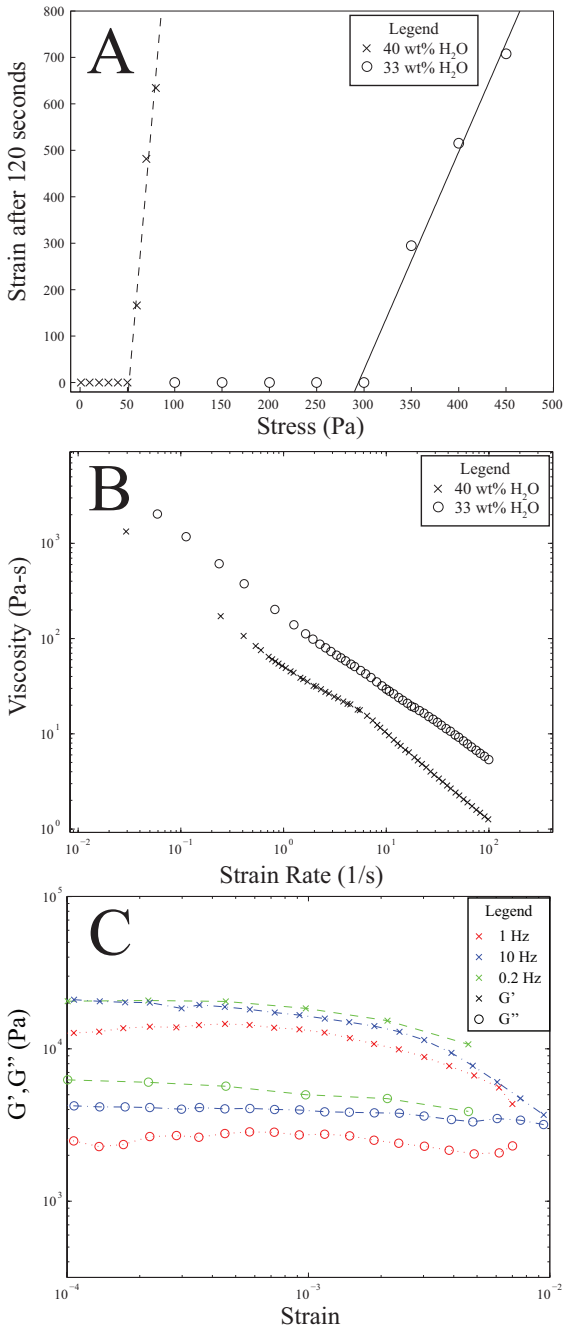

Figure 4.8: (A) Yielding behavior of mud from crater of Davis-Schrimpf mud volcano 12 (x symbol) and from the interior of a viscous mud flow sampled on 4/6/2010 (∘ symbol). The dashed and solid lines are fits to last three data points (x) and last four data points (o), respectively. The best fit lines intersect the x-axis at 52 Pa (x) and 294 Pa (∘), estimates of the yield strength of the muds. (B) Effective viscosity of the same mud samples used in (A), which depends on strain rate. Note that the mud with higher water content (x) is 3-4 times less viscous than the mud with lower water content (∘). (C) Storage modulus (G', 'x' marker) and loss modulus (G", 'o' marker) of mud (low viscosity sample from A and B) as a function of frequency and strain amplitude under oscillatory shear. The strain frequencies and amplitudes used here are representative of those experienced at the WLA site during the El Mayor-Cucapah event. We interpret the decrease in G' between strain amplitudes of 10^{-3} and 10^{-2} as representing the onset of fluid-like behavior.

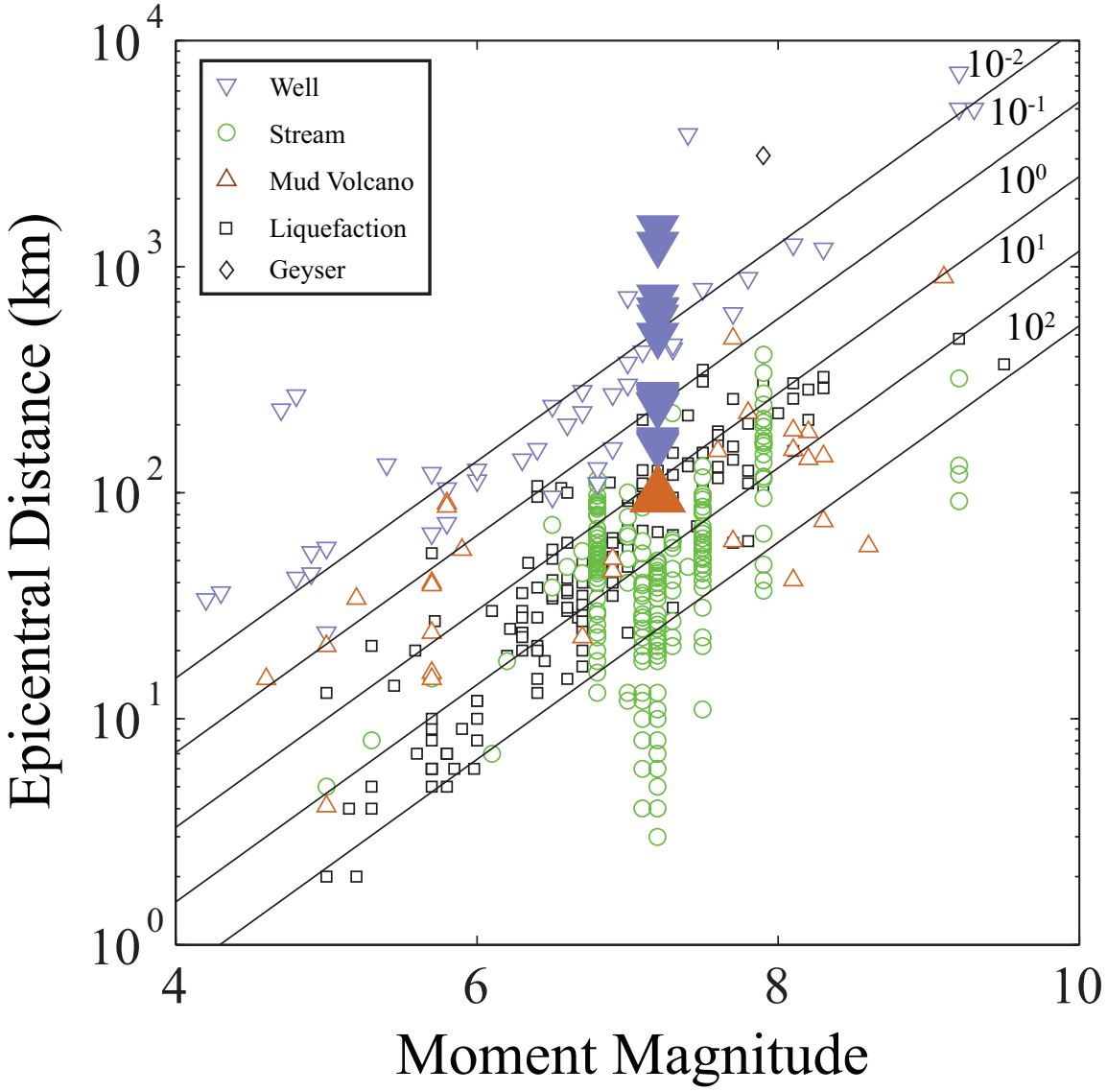

Figure 4.9: Documented occurrences of liquefaction, stream flow changes, mud volcano eruptions, and well water-level changes in response to earthquakes as a function of distance from epicenter and moment magnitude, as compiled by *Wang and Manga* (2010). Large filled symbols correspond to well (blue) and mud volcano (brown) responses to the El Mayor-Cucapah event. Diagonal lines are contours of constant seismic energy density in J/m^3 (*Wang and Manga*, 2010), which we expect to define the region in which triggering is possible. The Davis-Schrimpf mud volcanoes are within the range of parameter space where triggering of mud volcanoes has been previously documented.

Mau et al., 2007), (5) mobilization of pre-existing bubbles (*Steinberg et al.*, 1989; *Sahagian and Proussevitch*, 1992), (6) increasing permeability or opening fractures (*Rojstaczer et al.*, 1995; *Elkhoury et al.*, 2006; *Wang et al.*, 2004a,b; *Brodsky et al.*, 2003), and (7) enhanced gas production. We consider (1) unlikely because the Davis-Schrimpf mud volcanoes experienced volumetric expansion in the El Mayor-Cucapah event (Figure 4.4), which we do not expect to expel pore fluids, but could enhance permeability, in which case we would treat this mechanism concurrently with (6). Furthermore, we disfavor this mechanism because the amplitude of static volumetric strain (10^{-8}) is much smaller than the amplitude of dynamic shear strain (10^{-2}) at the Davis-Schrimpf site. Mechanism (2) is not applicable in this case because the Davis-Schrimpf location is not in the near-field of the El Mayor-Cucapah event. Mechanism (3) is unlikely to have occurred because liquefaction was not observed at the Wildlife Liquefaction Array (*Pridmore et al.*, 2010). Mechanism (4) may be immediately removed from further consideration because gas hydrates are not stable in this geologic setting.

Like their magmatic cousins, mud volcanoes are driven by gas escape. Therefore it is natural to consider triggering mechanisms involving gas bubbles such as nucleation (*Steinberg et al.*, 1982), bubble growth (*Hsieh*, 1961; *Sturtevant et al.*, 1996), and mobilization (*Sahagian and Proussevitch*, 1992). Gas bubbles trapped in a yield strength fluid may be mobilized if seismic shaking temporarily weakens the material. This mechanism was considered for earthquake triggering of the Sidoarjo mud flow but rejected due to very low strain amplitudes (*Manga et al.*, 2009). However, the El Mayor-Cucapah event produced dynamic strains larger than 1% in the Imperial Valley, large enough to weaken mud (Figure 4.8).

In general, a bubble may rise through a yield strength fluid only if the buoyancy force resulting from its density is sufficiently large to overcome the yield strength (τ_y). The measured yield strength of mud from the mud volcano craters is 52 Pa and the yield strength of mud from the low-water-content flow is 294 Pa. Because the mud is able to erupt and form flows of finite thickness, we expect the yield strength to limit flow thickness ($h \sim \tau_y/(\rho g) \sim 2.5$ mm to 1.5 cm). The measured yield strengths are qualitatively consistent with the thickness of flows that we observed in the field.

Dubash and Frigaard (2004) studied the conditions necessary to arrest bubbles in a Herschel-Bulkley (non-Newtonian, yield stress) fluid. The Herschel-Bulkley rheological model was chosen specifically for application to bubbles in drilling muds. For permanently immobilized, spherical bubbles, *Dubash and Frigaard* (2004) give the condition $\tau_y < \Delta\rho g R$ where $\Delta\rho \sim 2000$ kg m^{-3} is the density difference between the bubble and mud, g is gravitational acceleration, and R is a characteristic length scale for the bubble. We define a critical bubble as the largest bubble whose buoyancy is unable to overcome the mud's yield strength, and consider the possibility that a coseismic, transient reduction in yield strength mobilized critical bubbles. The critical bubble radius R_C is between ~ 2.5 mm (using the lowest measured yield strength) and 1.5 cm (assuming the highest measured yield strength). The radius of bubbles bursting in the mud volcano craters is about 10 cm. Assuming that a critical bubble conserves mass during ascent, the depth at which the critical bubble becomes mobilized can be calculated. Assuming that $V_{\text{surf}}/V_0 = P_0/P_{\text{surf}}$ where the subscript 0 refers to the depth

of mobilization, we obtain $4 \cdot 10^6$ Pa $< P_0 < 8 \cdot 10^8$ Pa, corresponding to depths between 200 m and 40 km if $\rho = 2000$ kg m^{-3}, implying expansion from a source region below the deltaic and lacustrine deposits (*Mazzini et al.*, 2011). Because the mud source is believed to be in the deltaic and lacustrine deposits, we interpret the large depth of mobilization as evidence that bubble coalescence occurs during ascent.

In order to quantify the time scale associated with a mud volcano response due to mobilization of bubbles, we must estimate bubble rise velocity. Mud is non-Newtonian and has a yield strength, but we can place an *upper bound* on the true bubble rise velocity by approximating mud as a Newtonian fluid. Bubble ascent velocity is limited not only by rheology but also by the finite width of the conduits through which bubbles rise. Bubble ascent rate through an unbounded Newtonian fluid is given by $U = R^2 \Delta\rho g/(3\mu)$ in the creeping (Stokes) flow regime. At Reynolds number (Re) > 0.1 it is necessary to adopt a parameterization that accounts for inertia. We use the parameterization given by *Clift et al.* (1978, p. 206) for terminal velocity of mm- to decimeter-sized bubbles in a Newtonian fluid:

$$2\mathrm{Re}^2 + 6\mathrm{Re}\left[(2+3\kappa)/(1+\kappa)\right] - \mathrm{Ar} = 0 \tag{4.2}$$

where $\kappa = \mu_{gas}/\mu_{liquid}$ is a viscosity ratio, $\mathrm{Ar} = g\rho_{liquid}\Delta\rho R^3/\mu^2$ is an Archimedes number, and R is bubble radius. We use the best-fit to our viscosity measurements (Figure 4.8), given by Equation 4.1. We approximate strain rate as $\dot{\epsilon} = U/R$, and assume that $\mu_{\mathrm{gas}} = 1.5 \cdot 10^{-5}$ Pa-s and $\rho_{liquid} = 2000$ kg m^{-3}. We solved Equation 4.2 numerically for various choices of R and both parameterizations of μ. Figure 4.10 shows that ascent velocities are vanishingly small ($10^{-5} - 10^{-8}$ m/s) for 1 cm bubbles but become large ($0.1 - 1$ m/s) for decimeter-sized bubbles.

The time scale associated with the bubble mobilization response mechanism is strongly dependent on the choice of bubble size and assumed depth of bubbles prior to the onset of shaking, but in general can be constrained using the maximum radius of bubbles bursting at the surface (0.1 m) and the thickness of the deltaic and lacustrine deposits (200 m). We calculated bubble ascent times as a function of initial bubble size and initial bubble depth using both viscosity parameterizations and using (1) constant bubble radius and (2) allowing bubble radius to change with pressure (depth) according to $V/V_0 = P_0/P$. For a given initial radius and depth, bubbles ascend most quickly when they expand and viscosity is low (Figure 4.10C) and most slowly when they do not expand and viscosity is high (Figure 4.10B). We use these two bounding scenarios to test the plausibility of the bubble mobilization mechanism. In Figure 4.10B-C, we have shaded in light grey the region corresponding to ascent times of 6 hours to 5 days, representing plausible response time scales and we have shaded dark grey the region corresponding to plausible critical bubble sizes. The lack of overlap between light and dark shaded regions indicates that the mobilization of critical bubbles cannot produce an increase in gas flux over the observed response time scale.

If critical bubbles become mobilized and subsequently coalesce, they will ascend more rapidly than the original critical bubbles. In Figure 4.10C, the dark line marked $R_{0,\mathrm{S}}$ indicates the initial radius of bubbles that expand to have a radius of 0.1 m at the surface. This

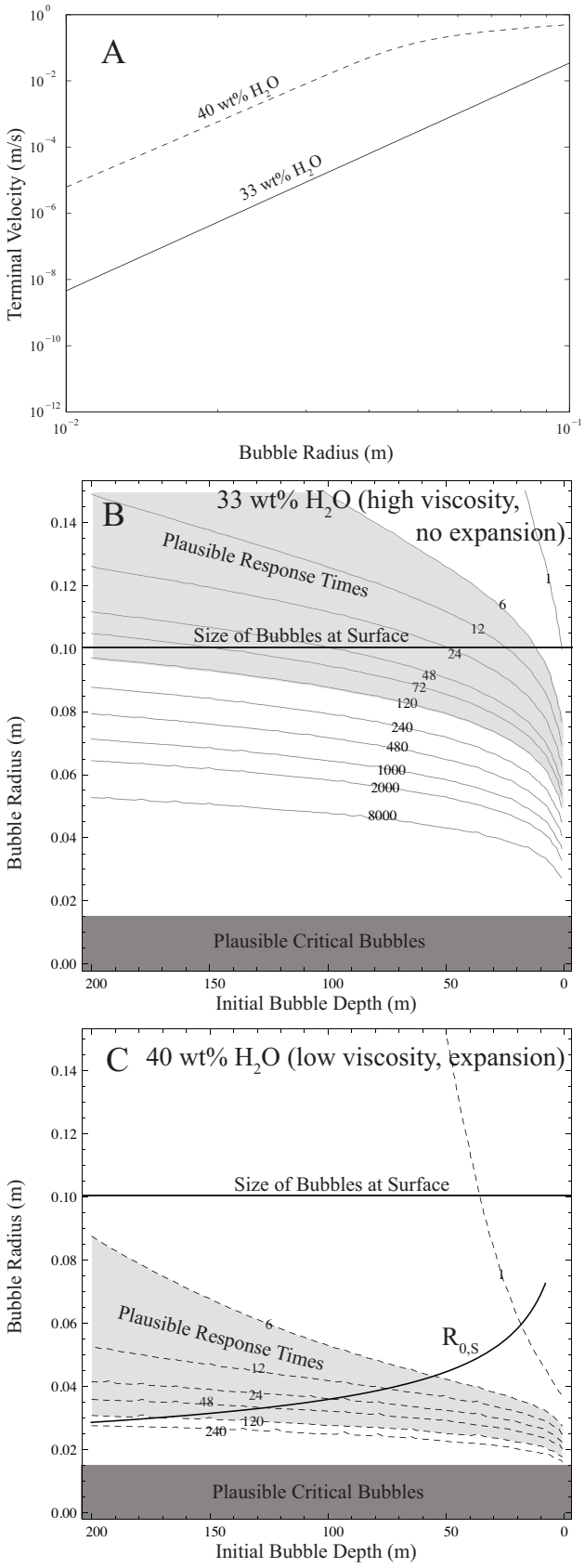

Figure 4.10: (A) Terminal velocity of bubbles in a Newtonian fluid, from numerical solution of Equation 4.2, using measured mud viscosity (shown in Figure 4.8B). Bubbles of decimeter size (comparable to those observed bursting in mud volcanoes) rise at 0.03-0.50 m/s. Bubbles smaller than a few centimeters are essentially immobile. The calculated velocity is an upper bound on the rise speed through mud. (B and C) Contour plots of bubble ascent time (hours) for different choices of initial bubble depth and bubble radius. Panel B assumes the most viscous, and panel C the least viscous, measured rheology. In panel B we assume that bubble size remains constant during ascent, and in panel C we assume that bubbles conserve mass and expand in response to changing pressure. Panels B and C should be interpreted as upper and lower bounds, respectively, on the response time. The dark shaded region at the bottom of B and C denotes the plausible size range of critical bubbles (defined in text), and its lack of overlap with the light shaded region disfavors the bubble mobilization response mechanism. The curve marked $R_{0,S}$ indicates the size of bubble at depth that expands to a radius of 0.1 m at the surface.

curve passes through the light grey region of plausible response times, which indicates that if coalescence happens quickly, the bubble mobilization mechanism may be viable. The rate of coalescence of cm-sized buoyancy-driven bubbles in the Stokes flow regime was studied by *Manga and Stone* (1995) by solving population dynamics equations and using a coalescence rate based on laboratory experiments. The rate of coalescence of cm-sized bubbles can be greatly enhanced over that of spherical bubbles owing to their interaction-induced deformation (*Manga and Stone*, 1994). The magnitude of deformation scales with the Bond number $\mathcal{B} = \Delta\rho g R^2/\sigma$, a measure of the relative importance of buoyancy and surface tension forces. Using a surface tension $\sigma = 7 \cdot 10^{-2}$ Pa·m^{-2} and the critical bubble radii previously introduced, we compute $1.8 < \mathcal{B} < 64$. Bubbles smaller than about 4 cm rise at Re< 0.1, so the Stokes flow assumption is valid for critical and near-critical bubbles. The characteristic timescale for bubble interactions is given by $t_c = \mu/(\Delta\rho g r_0 \phi_0)$ where r_0 is initial bubble radius and ϕ_0 is initial bubble volume fraction. We adopt a range of viscosities of $10^6 - 10^7$ Pa-s, characteristic of the effective viscosities of mud surrounding bubbles that are slightly larger than critical. Assuming $\phi_0 = 0.01$ (a guess), we find $2 \cdot 10^6$ s $< t_c < 3 \cdot 10^6$ s (11.5 days $< t_c <$ 35 days). The rate of coalescence scales linearly with $\mathcal{B}$. However, the mean bubble size does not increase significantly within the first t_c. It thus appears unlikely that coalescence of mobilized bubbles can act quickly enough to produce bubbles sufficiently large to produce the observed response. Furthermore, the bubble coalescence model assumes that the bubbles exist in an unbounded fluid medium. Conduit boundaries limit the interactions between bubbles and hence will tend to retard bubble coalescence, so our estimate of t_c should be interpreted as a lower bound.

In the above calculations, we assumed that the mud in the subsurface, where bubbles might be immobilized, has the same water content as the mud erupted at the surface. There is no reason for this to be true, and the effective viscosity and yield strength of the mud at depth might vary considerably depending on the water content. *Coussot and Piau* (1994) measured the rheology of water-kaolinite mixtures with varying water content and found order-of-magnitude increases in viscosity when solid fraction increased from 15.4% to 27%. We measured a 6-fold increase in yield strength when solid mass fraction increased from 60% to 67%. A higher viscosity at depth resulting from lower water content would increase the response time, reducing further the plausibility of the bubble mobilization response mechanism.

The exceptionally slow ascent rate of critical-sized bubbles makes it unlikely that mobilization of critical or near-critical bubbles is the triggering mechanism responsible for the observed change in gas flux. Coseismic strength reduction could also increase the ascent rate of larger-than-critical bubbles, but the ascent rate would only increase for a short time during and after shaking. We did not observe any hysteresis in the mud samples when we performed oscillatory strain runs in immediate succession. Each of the experimental runs required about 20 minutes, which, if used as an upper bound on the time scale of strength recovery, cannot explain the observed increase in gas flux two days after the El Mayor-Cucapah event.

Coseismic enhancement of fracture permeability by removal of blockage has been inferred

in bedrock aquifers (e.g. *Rojstaczer and Wolf*, 1992; *Rojstaczer et al.*, 1995; *Wang et al.*, 2004b; *Brodsky et al.*, 2003) and laboratory experiments (*Elkhoury et al.*, 2011; *Liu and Manga*, 2009). The El Mayor-Cucapah event triggered slip on nearby faults including the San Andreas and Superstition Hills faults as well as several faults in the Brawley Seismic Zone (*Treiman et al.*, 2010), and slip may increase fault zone permeability. If the increased gas flux was facilitated by increased fracture permeability, the permeability increase could have occurred in the SSGS reservoir, in the shallow lacustrine and deltaic deposits, or both. The time scale associated with the observed response (less than two days), together with permeability estimates and knowledge of local geology allows us to critically evaluate this mechanism. In the subsequent analysis, we assume that gas bubbles and water comprise the pore fluid in a porous aquifer, whereas when considering the bubble mobilization mechanism we assumed that gas bubbles were a discontinuous phase in a mud continuum. This assumption and the corresponding analysis are reasonable if the mud source is shallow (e.g. *Svensen et al.*, 2009) and the permeability enhancement occurs below the mud source depth.

Changes in permeability will result in a redistribution of pore pressure by fluid flow over a characteristic time scale $t \sim d^2/\kappa$ where d is a characteristic depth and κ is a vertically-averaged gas diffusivity in the depth interval [0,d]. The strata in the cap rock unit are essentially flat-lying, so vertical permeability will be dominated by the least permeable stratigraphic layer, or by fracture permeability. Ongoing gas escape implies that there is significant vertical permeability, which we attribute to fracture permeability. We place a lower bound of 10^{-6} to 10^{-4} m/s on the hydraulic conductivity using measured hydraulic conductivities in the shallow subsurface of the WLA site (*Youd et al.*, 2004), consistent with intrinsic permeabilities of the types of sediment present. These hydraulic conductivity values are given for water only, but in fact the SSGS is a multiphase system with both liquid and gas present. We assume that in this system, water comprises the continuous phase. In general, the relative permeability of each phase in the system is a function of the volume fractions of each phase, capillary number of the flow, viscosity ratio of the phases, and flow history (*Adler and Brenner*, 1988). In order to quantify the response time scale, we make use of the hydraulic diffusivity $\kappa = K/S_S$ where K is hydraulic conductivity and S_S is the specific storage. In multiphase systems, each of these parameters is phase-specific. The hydraulic conductivity (K) and permeability (k) are related by $K = k\rho g/\mu$. Noting that k represents only properties of the porous medium and not the fluid occupying its pores, we estimate the ratio of gas hydraulic conductivity to liquid hydraulic conductivity:

$$K_{gas}/K_{liq} \sim \frac{(10^0 \text{ kg/m}^3)/(10^{-5} \text{ Pa-s})}{(10^3 \text{ kg/m}^3)/(10^{-3} \text{ Pa-s})} = 10^{-1} \tag{4.3}$$

Specific storage is defined as $S_S = \rho_f g\,(\alpha + \phi_f \beta)$ where α is the matrix compressibility, β is the fluid compressibility, and ϕ is porosity. Because gases are much more compressible than liquids, we can neglect matrix compressibility and estimate the ratio of $S_{S,\text{gas}}/S_{S,\text{liq}}$ as:

$$S_{S,\text{gas}}/S_{S,\text{liq}} \sim \frac{(10^0 \text{ kg/m}^3) \cdot (10^{-5} \text{ Pa}^{-1})}{(10^3 \text{ kg/m}^3) \cdot (10^{-10} \text{ Pa}^{-1})} = 10^2 \tag{4.4}$$

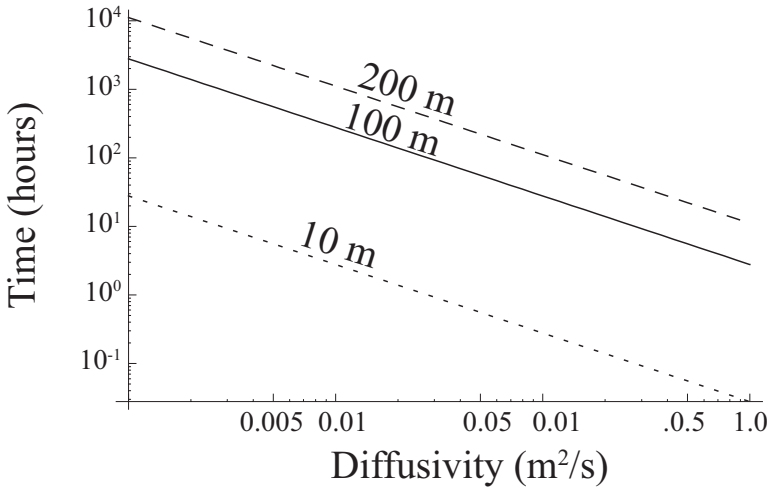

Figure 4.11: Diffusive time scale as a function of diffusion length scale and diffusivity. We estimate the gas diffusivity in the upper 200 m of the Davis-Schrimpf site as $10^{-3} - 10^{0}$ m^2/s. The time scale is at most 10^4 hours.

Therefore, we expect the ratio of diffusivities in identical single phase gas and liquid systems to be $\kappa_{gas}/\kappa_{liq} \sim (K_{gas}/K_{liq}) \,/\, (S_{S,\mathrm{gas}}/S_{S,\mathrm{liq}}) = 10^{-3}$. This ratio is an upper bound on the diffusivity ratio that we would expect in a system where two phases are present and gas is the dispersed phase, since the relative permeability of the gas phase will be smaller than the permeability in a gas-only system.

If we adopt standard values of $10^0 - 10^3$ m^2/s for the hydraulic diffusivity of water in unconsolidated sediments (*Roeloffs*, 1996), the corresponding gas diffusivities are $10^{-3} - 10^0$ m^2/s. The time scale associated with the post-seismic gas response could be almost instantaneous or more than a year, assuming a length scale representative of the thickness of the near-surface river and lacustrine deposits, 200 m (Figure 4.11). Because gas fluxes were significantly higher on 4/6/2010 than prior to the earthquake, and had returned to within one standard deviation of the pre-earthquake values by 5/12/2010, we disfavor response time scales longer than a few days, hence favoring hydraulic diffusivities greater than 10^{-1} m^2/s. The return of gas flux to the pre-earthquake values could be a result of (1) recovery of permeability, or (2) depletion of the gas source region. Our data do not allow us to discriminate between these mechanisms. Because of the large uncertainty in hydraulic diffusivity, we cannot constrain the depth at which the response occurred.

Lastly, we note that the mobilization of bubbles from an hypothetical bubble source region would deplete that region in bubbles, which might produce a period of lower-than-average gas discharge, depicted in Figure 4.12, while the source region was recharged, an effect that would allow us to discriminate between this mechanism and a permeability enhancement mechanism.

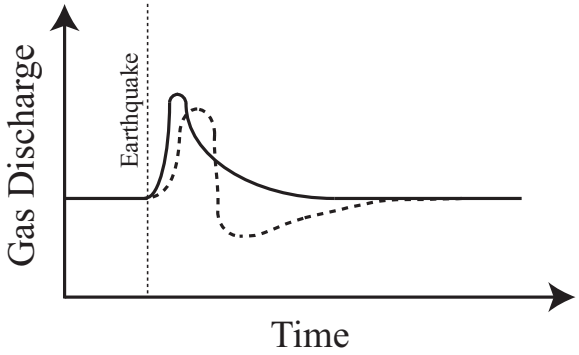

Figure 4.12: Two hypothetical gas hydrographs for the bubble mobilization mechanism (dashed curve) and permeability enhancement (solid curve) response mechanisms. The bubble mobilization mechanism may cause gas flux to fall below its pre-earthquake value due to depletion of the gas source region.

4.7 Conclusions

The measured gas flux at the Davis-Schrimpf mud volcanoes was higher two days after the April 4, 2010 El Mayor-Cucapah earthquake then either one month before or one month after the event. We interpret the observed increase in gas flux as a triggered change in activity. The triggered response is not unexpected based on magnitude-distance-triggering relationships (Figure 4.9). We considered two seemingly viable triggering mechanisms: bubble mobilization and permeability enhancement. Of these, the latter is more likely to be responsible for the observed response because (1) the time scale associated with the ascent of the small bubbles that would be mobilized by seismic shaking is too long and (2) the time scale associated with the response due to permeability enhancement is consistent with our observations. The rejection of the bubble mobilization mechanism is important because the strain at the Davis-Shrimp mud volcanoes during the El Mayor-Cucapah earthquake was large enough that this mechanism could conceivably have been important. We view the ineffectiveness of the bubble mobilization mechanism in this case study, where mud rheology and shear strain amplitude were favorable, as evidence for the rejection of this mechanism in general. The gas discharge had recovered to within one standard deviation of the pre-earthquake value by May 12, 2010, implying that permeability decreased or that the gas reservoir was depleted during the period of high gas discharge. It would be possible to discriminate between these mechanisms by measuring gas pressure at depth.

Future large earthquakes will provide further opportunities to study mud volcano and hydrologic responses to earthquakes. There have been at least 13 large ($M_W > 6$) earthquakes in the Imperial and Mexicali Valleys since 1852 (*Anderson and Bodin*, 1987). Following the next large earthquake, we will make more frequent gas flux measurements and also sample gas with a high temporal frequency with the aim of constraining the source of excess gas or location of increased permeability. We may be able to use the shape of the gas hydrograph

(Figure 4.12) to further constrain the nature of the response mechanism. In this study, we measured only localized gas emission, but there is almost certainly diffuse gas emission from the SSGS and it would be most interesting to see whether it too responds to earthquakes.

Acknowledgments

We extend our profuse thanks to David K. Lynch for his generosity in introducing us to the Davis-Schrimpf field site, assisting us with field work on March 13, 2010, and for stimulating conversations about this work and other work being done in this fascinating and beautiful part of California. Benjamin Andrews helped with field work on March 13, 2010. Tim Teague performed the XRD analysis. CILAS Laser Particle Size, Inc. provided us with the grain size measurements. Amanda Thomas assisted with the preparation of Figure 4.1. We thank Marco Bonini and an anonymous review for comments that improved the quality of the manuscript. This material is based upon work supported under a National Science Foundation Graduate Research Fellowship. This work was further supported by the National Science Foundation under Grant No. EAR-0909701.

Chapter 5

Frequency Dependence of Mud Volcano Responses to Earthquakes

5.1 Abstract

Distant earthquakes can trigger the eruption of mud volcanoes. We document the response of the Davis-Schrimpf mud volcanoes, California, to two earthquakes and non-response to four additional events. We show that the Davis-Schrimpf mud volcanoes are more sensitive to long period seismic waves than to shorter period waves of the same amplitude. Our observations are consistent with models for dislodging bubbles and particles by time varying flows produced by seismic waves. Mobilizing trapped bubbles or particles increases permeability or fluid mobility, increasing discharge.

5.2 Introduction

Changes in crustal stress generated by earthquakes affect geological and hydrological processes at distances that exceed several times the length of the ruptured fault. Examples of triggered phenomena include other earthquakes, the eruption of magmatic and mud volcanoes, the eruption of geysers, changes in permeability of the crust, and increased discharge at springs and in streams. A review of these phenomena and compilation of observations are presented in *Wang and Manga* (2010).

The eruption of mud volcanoes in response to earthquakes has a long history of being documented (e.g. *Pliny*, 79; *Chigira and Tanaka*, 1997; *Manga and Brodsky*, 2006; *Mellors et al.*, 2007; *Bonini*, 2009a; *Rudolph and Manga*, 2010). Figure 5.1 shows the relationship between earthquake magnitude and the distance of the triggered eruption from the earthquake. There is a clear pattern in that larger earthquakes can trigger eruptions at greater distances. Also shown in Figure 5.1 is an estimate of the energy dissipated by the seismic waves at the eruption location (*Wang*, 2007). Eruptions appear to be triggered for energy densities as small as 10^{-1} J/m^3. To put this number in perspective, sediments prone to liquefaction require energy densities > 30 J/m^3 (*Green and Mitchell*, 2004) to liquefy by undrained consolidation, the mechanism thought to be responsible for liquefaction in the near-field (*Wang*, 2007). Thus, the eruption of previously existing mud volcanoes is not likely to arise from the processes that create the small mud and sediment eruptions produced by liquefaction of shallow sediments by undrained consolidation. The mechanism or mechanisms responsible for mud volcano responses remain uncertain. Possible explanations include an increase in permeability or fluid mobility resulting from the mobilization of trapped colloidal particles (e.g. *Roberts and Abdel-Fattah*, 2009) or bubbles (e.g. *Beresnev*, 2006) by the time-varying flows produced by the passage of seismic waves.

Here we investigate whether the frequency of seismic waves, in addition to their amplitude, plays a role in triggering eruptions. Our interest in establishing the presence or absence of a frequency-dependence is that it may be used to distinguish between triggering mechanisms. With a better understanding of how earthquakes trigger eruptions, it should be possible to more reliably assess whether any given eruption is the result of an earthquake. A prominent application is the ongoing eruption of mud at the Lusi eruption in Indone-

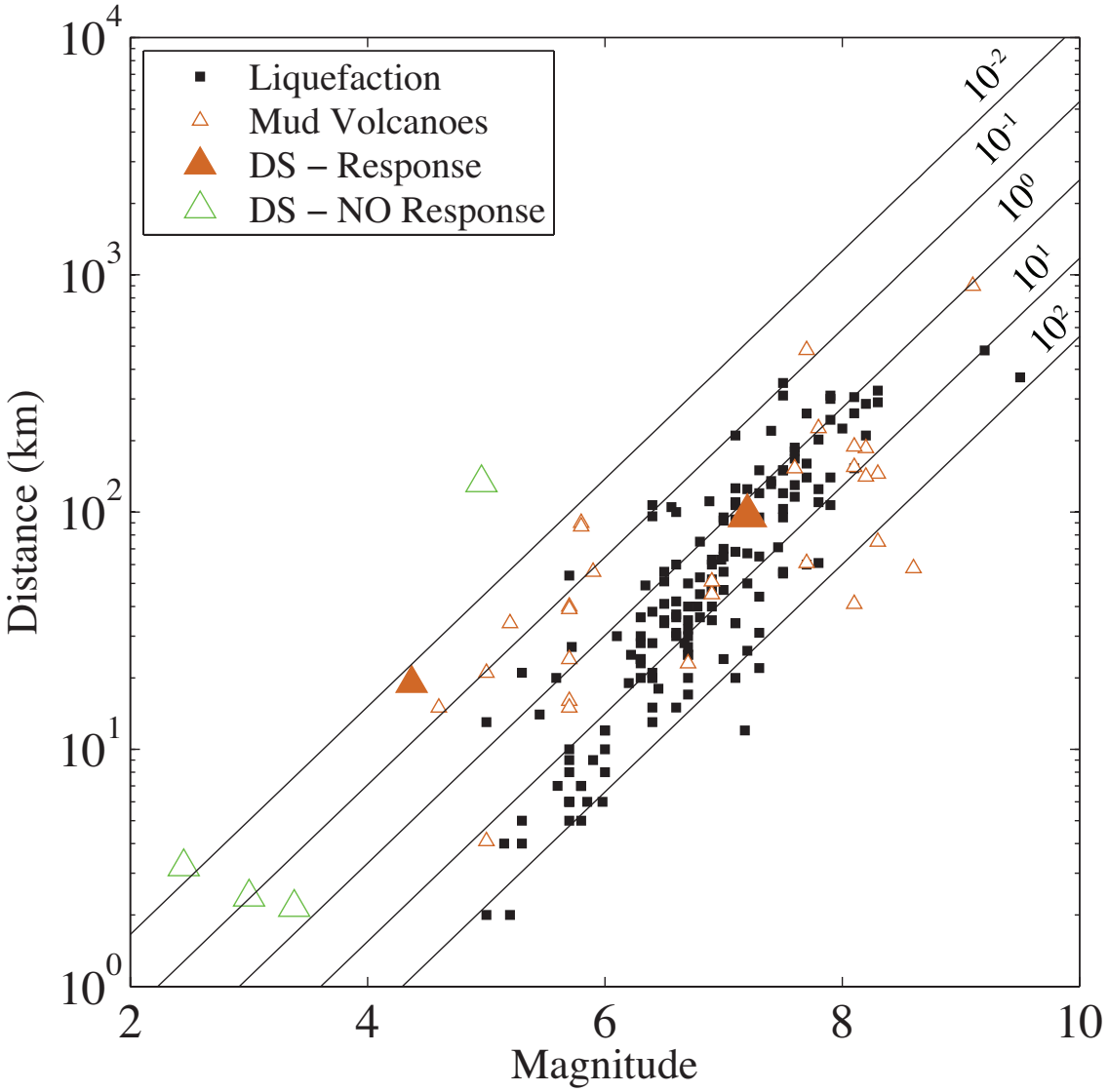

Figure 5.1: Occurrence of liquefaction and triggered eruption of mud volcanoes. Epicentral distance is the distance between the observation and earthquake epicenter. Magnitude is moment magnitude. Data tabulated in *Wang and Manga* (2010). The four open green triangles indicate the four documented non-responses of the Davis-Schrimpf mud volcanoes. Labeled contour lines show seismic energy density is units of J/m^3 based on the model of *Wang* (2007).

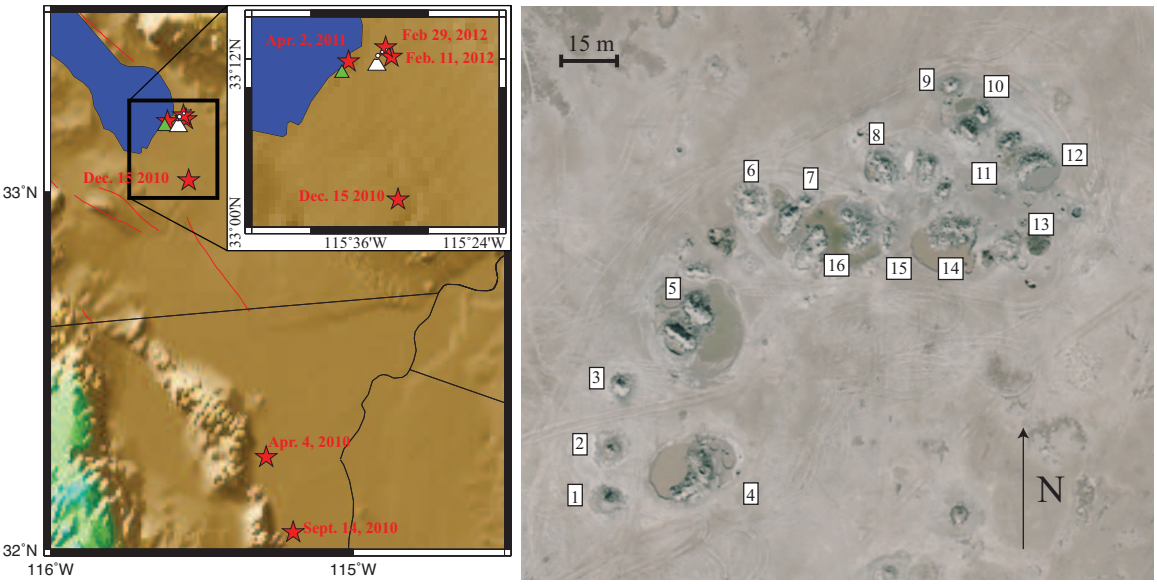

Figure 5.2: (left) Location of mud Davis-Schrimpf mud volcanoes (white volcano glyph), seismometer CI.RXH (green triangle), and the epicenters of earthquakes we consider (red stars). (right) Location and numbering convention of the mud volcanoes.

sia (*Davies et al.*, 2007) that has continued for > 5 years and caused billions of dollars of economic losses (*Richards*, 2011). In this case, the eruption has been attributed to an earthquake (e.g. *Mazzini et al.*, 2007, 2012), not an earthquake (e.g. *Manga*, 2007), or to drilling operations at a gas exploration well (e.g. *Davies et al.*, 2007, 2008).

5.3 Data

Since March 2010, we have been monitoring the eruption of mud and CO2 gas at subaerial hydrothermal vents in the Imperial Valley, California, at a set of features locally known as the Davis-Schrimpf mud volcanoes (*Lynch and Hudnut*, 2008). Figure 5.2 shows the location of the Davis-Schrimpf seep field and the numbering scheme we use to identify each mud volcano. Their tectonic context, geochemistry, and geomorphology are described by *Lynch and Hudnut* (2008), *Svensen et al.* (2009) and *Onderdonk et al.* (2011), respectively. *Rudolph and Manga* (2010) documented their response to the 4 April 2010 magnitude 7.2 El Mayor-Cucapah earthquake and described the grain size distribution and rheology of the erupting mud. Since then, we have continued to monitor responses to large regional and small local earthquakes. Table 5.1 lists the earthquakes following which we collected measurements.

We made campaign measurements several times per year and as soon as possible (always between 1 and 2 days) following local and regional earthquakes that may have produced shaking strong enough to trigger a response based on the empirical energy dissipation curves

Date	Time (UTC)	Magnitude	Epicentral distance	PGV (cm/s)
April 4, 2010	22:40:42	7.2	96.6 km	14.4
September 14, 2010	10:52:18	4.96	133 km	0.12
December 15, 2010	19:16:47	4.37	18.97 km	0.17
April 2, 2011	02:32:51	2.45	3.19 km	0.07
February 11, 2012	09:46:47	3.0	2.46 km	0.08
February 29, 2012	17:35:55	3.4	2.16 km	0.25

Table 5.1: Attributes of 6 earthquakes for which we document responses

in Figure 5.1 and strain records from the nearby Wildlife Liquefaction Array. During each visit we measured gas discharge, mud temperature, and counted the number of fresh flows on the flanks of the mounds of mud. We measured gas discharge using a funnel (diameter 22 cm) attached to a Cole-Parmer gas flowmeter with stated accuracy $\pm 5\%$ and repeatability $\pm 0.5\%$. The gas discharge was manually read from the flowmeter gauge, with uncertainty less than 10%. Temperature was measured using a thermistor inserted to depths of ~ 10 cm. Rudolph and Manga (2010) show pictures of the mud volcanoes and fresh flows, defined as being active or having a moist surface appearance, indicating activity within a few days prior to the field visit. The first two field visits occurred prior to any of the earthquakes; three visits occurred prior to the start of construction at the nearby Hudson Ranch I geothermal facility; all visits occurred prior to the plants commissioning on March 9, 2012 (*Cichon*, 2012).

In order to assess the ground motion, we used data recorded at station CI.RXH, maintained by the Southern California Seismic Network, sited 4.5 km ESE from the mud volcanoes. The instrument is a CMG-3T broadband seismometer with response from 120 s to 50 Hz. Figure 5.2 shows the location of the instrument relative to the mud volcanoes and the 6 earthquakes for which we have gas discharge data. Because the broadband seismometer at CI.RXH clipped during the El Mayor-Cucapah event, we integrated acceleration data recorded at station NP.5062, which has a FBA-D instrument, to assess ground motion for this event only.

5.4 Results

Figure 5.3 shows the measured gas flux and the number of fresh mud flows. We use vertical lines to indicate the time of earthquakes. At some volcanoes there are multiple data points as there are sometimes multiple vents. Responses to earthquakes are observed as increases in gas discharge. The mean discharge measured after the El Mayor-Cucapah and December 15, 2010 earthquakes was more than one standard deviation greater than the mean discharge computed from measurements collected on all other dates (Figure 5.3). There are no clear changes after the other four earthquakes. Mud temperature did not change following any of the earthquakes.

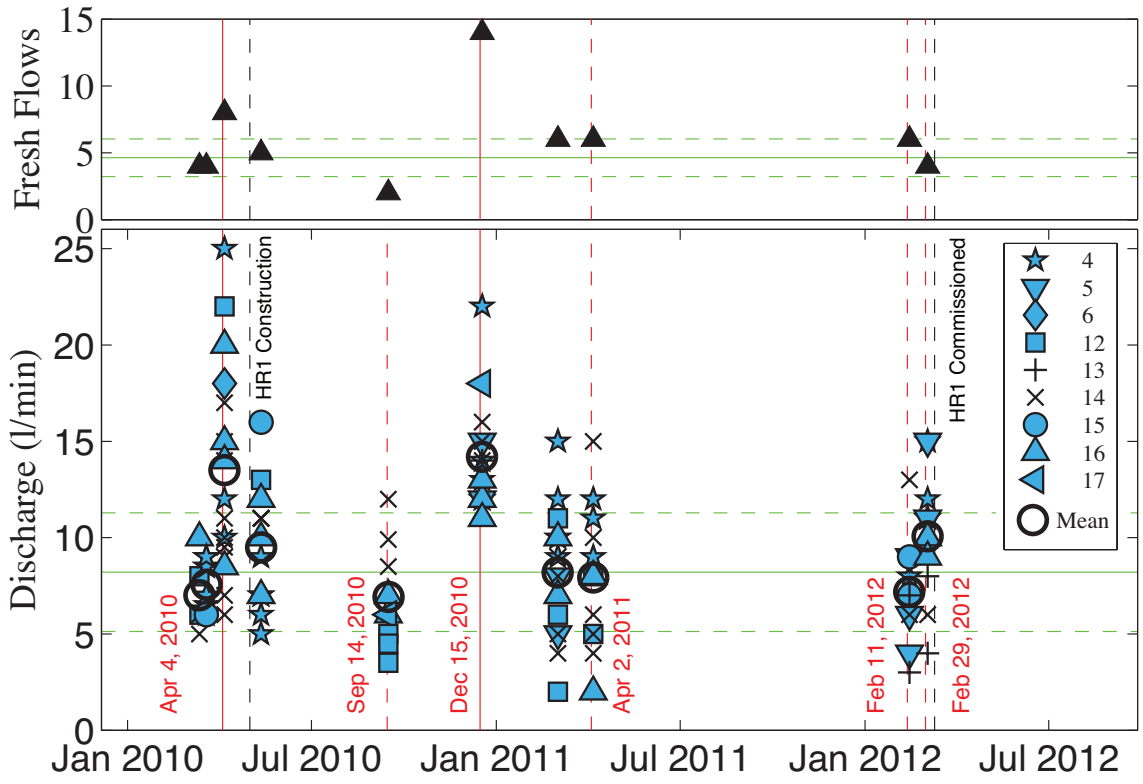

Figure 5.3: Number of fresh mud flows observed (top) and gas discharge (bottom) measured at mud volcanoes between March 2010 and March 2012. The legend associates symbols with individual mud volcanoes (locations shown in Figure 5.2). On a given day, there may be multiple data points at a given volcano if there are multiple active vents. Earthquakes that triggered a response are indicated by vertical solid lines and those that did not are indicated with vertical dashed lines. Dark circles indicate mean discharge on each date. The solid and dashed horizontal green lines indicate the mean and standard deviation of all data except those collected immediately following the April 4, 2010 and December 15, 2010 events. Vertical black dashed lines indicate start of construction and commissioning of the nearby Hudson Ranch I geothermal plant. Note that measurements were collected on two different dates prior to the 4 April, 2010 event.

5.5 Discussion

Larger earthquakes produce longer period seismic waves and the duration of shaking is longer as well. Thus the observation in Figure 5.1 that small earthquakes with large seismic energy densities do not increase eruption rate implies that short period waves or short shaking durations are less effective at influencing eruptions than long period waves. This is confirmed by spectrograms (Figure 5.4) of velocity waveform data. The key feature of the spectrograms in Figure 5.4 is that the two events to which the mud volcanoes responded have more power at low frequency than the four events that produced no response. The duration and amplitude of shaking during the September 14, 2010 event are greater than expected based on empiricisms (Figure 5.4), highlighting the importance of event-specific information.

The earthquakes that produced responses differ from those that did not in that they had greater power spectral density (PSD) at low frequencies (0-1.3 Hz). Figure 5.5a shows that, in general, mean discharge increases with increasing (PSD) in the 0-1.3 Hz band. Low-frequency PSD was greater for those earthquakes that produced a response than those that did not by at least 3.5 dB/Hz, corresponding to a difference in amplitude at these frequencies of 1.5 (Figure 5.5b). There is no correspondence between PSD at higher frequencies and mud volcano response (Figure 5.5b). Figure 5.5c shows the duration of shaking at low frequency with PSD greater than 10% of the maximum value. The duration of low frequency shaking during the September 14, 2010 event, which did not produce a response, was 3 times greater than the December 15, 2010 event that did produce a response. This argues for frequency, rather than duration, as the more important factor in determining whether a response occurs.

Our conclusion that long period seismic waves have a greater influence on mud eruptions is consistent with that reached in *Manga et al.* (2009) from an analysis of the reported responses of the Niikappu mud volcanoes in Japan to earthquakes (*Chigira and Tanaka*, 1997). The present study adds quantitative measurements about the nature of the responses and the triggering ground motions, which were not available at Niikappu.

Some other geological and hydrological responses to earthquakes also appear to be more sensitive to long period waves: triggered earthquakes in a geothermal setting (*Brodsky and Prejean*, 2005), non-volcanic tremor (*Guilhem et al.*, 2010), and field observations of liquefaction (e.g. *Wong and Wang*, 2007; *Holzer and Youd*, 2007). However, as concluded in a recent review, the data supporting this conclusion are still extremely sparse (*Manga et al.*, 2012).

Our primary objective in monitoring the Davis-Schrimpf mud volcanoes is to obtain observations that might provide insight into the mechanisms that trigger or modify eruptions. In this light we now assess which mechanisms are sensitive to the period of forcing. We consider only mechanisms that arise from time varying stress as these were 6 orders of magnitude larger than the static stress changes produced by the El Mayor-Cucapah earthquake (*Rudolph and Manga*, 2010). We do not consider the possibility of subcritical crack growth because the system is already erupting and we document increases in eruption rate, not new eruptions. We also do not consider bubble pressurization as a mechanism because *Ichihara and Brodsky* (2006) have shown that it is not effective, and further, this mechanism is not

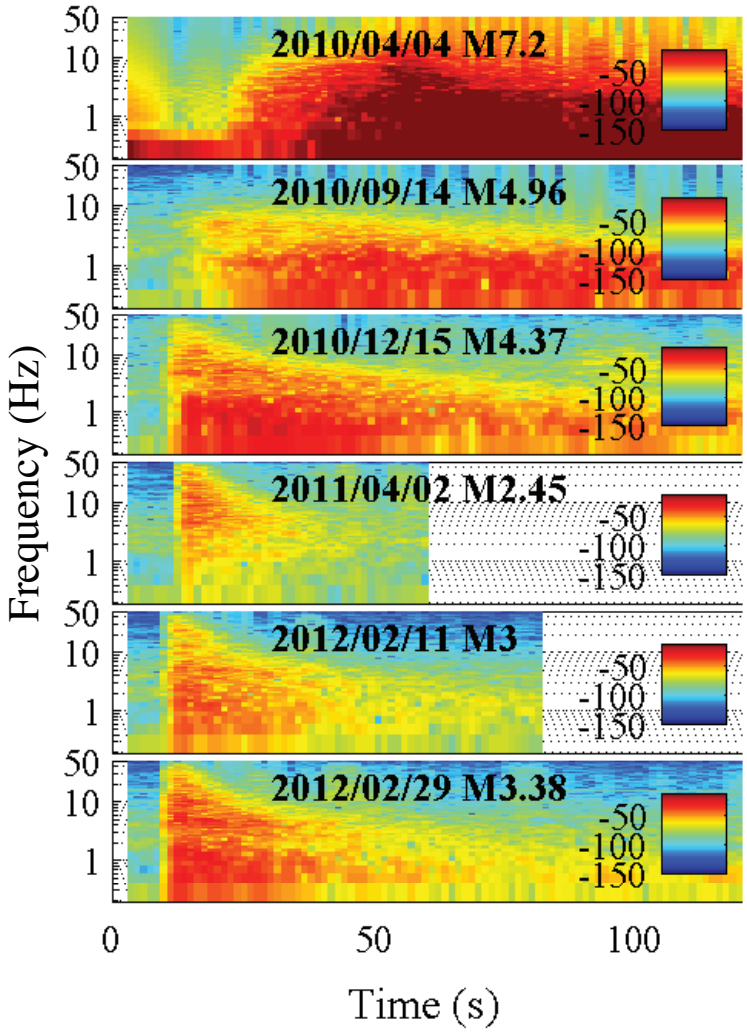

Figure 5.4: Spectrograms of East ground velocity for the 6 earthquakes listed in Table 5.1. Color scale represents power spectral density (dB/Hz). Spectrograms were calculated using a window length of 5.12 s, a Hamming mask, and window overlap of 384 samples.

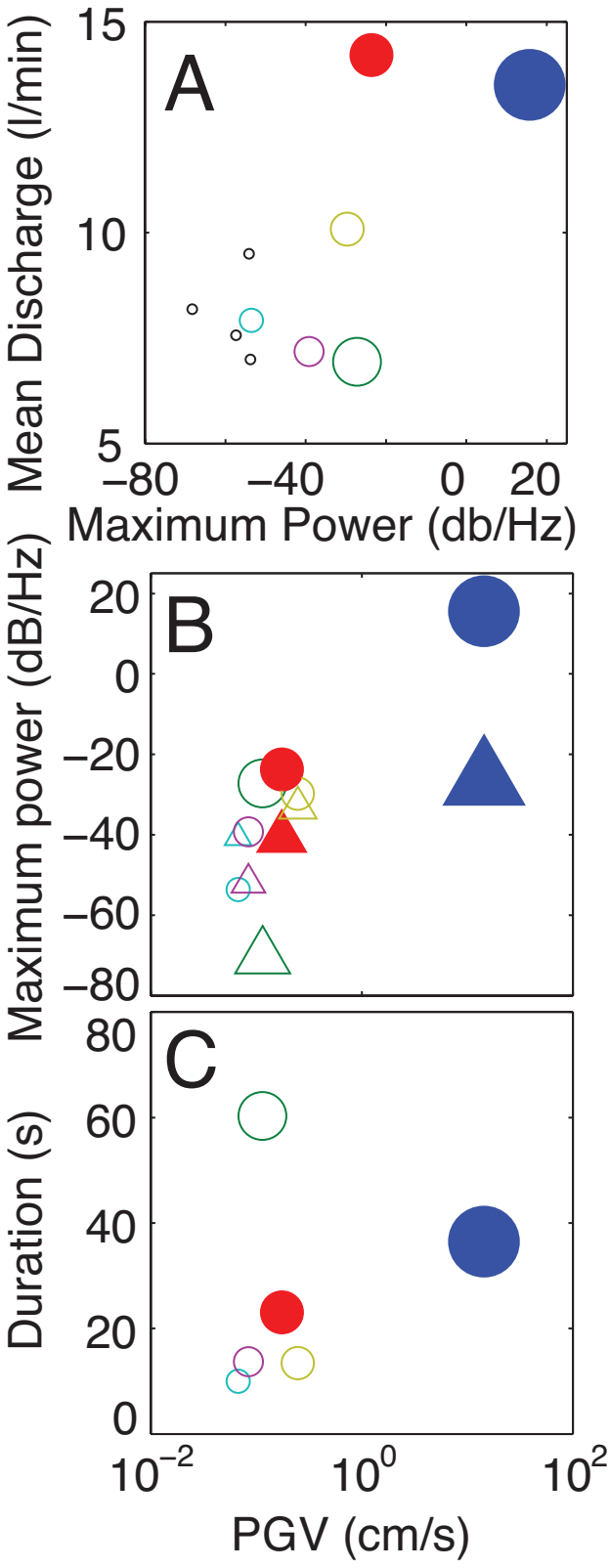

Figure 5.5: (a) Relationship between all mean discharge measurements and maximum PSD in the 0-1.3 Hz band. Size of symbols is proportional to earthquake magnitude. Filled symbols indicate earthquakes to which the mud volcanoes responded. Black circles indicate measurements that were not preceded by an earthquake. We used records from the two days preceding the measurement to compute PSD for these data. (b) Maximum PSD in the 0-1.3 Hz band (circles) and at 10 Hz (triangles). (c) Duration of shaking with power spectral density (PSD) in the 0-1.3 Hz band greater than 10% of the maximum recorded PSD, as a function of peak ground velocity (PGV).

frequency-dependent (*Brodsky and Prejean*, 2005).

Dislodging particles and bubbles by fluid flow induced by time-varying stresses are mechanisms that depend on the frequency of deformation (e.g. *Beresnev*, 2006). The pressure gradients created by inhomogenous poroelastic properties will be proportional to strain amplitude. The time available to mobilize particles or bubbles by the flow induced by these pressure gradients will be proportional to the period of the seismic waves. Thus long period waves with a given amplitude should be more effective at mobilizing trapped bubbles and particles that may be limiting permeability and the otherwise free flow of fluids and gas. Laboratory experiments confirm that oscillatory flows mobilize particles (e.g. *Beckham et al.*, 2012) and trapped droplets (e.g. *Beresnev et al.*, 2011).

Our observations do not provide new insight into the Lusi eruption in Indonesia. They are, however, consistent with previous compilations of observations that relate earthquake magnitude and distance over which triggered eruptions occur (*Mellors et al.*, 2007; *Manga et al.*, 2009; *Bonini*, 2009a). The magnitude-distance relationship shown in Figure 5.1 does not support an earthquake-trigger for the Lusi eruption.

5.6 Conclusion

The Davis-Shrimpf mud volcanoes, like other mud eruptions, appear to be more sensitive to long period waves than shorter period waves with similar amplitudes. Mobilization of particles or bubbles by oscillatory flows induced by seismic waves is consistent with this observation.

Acknowledgments

Acknowledgments: Supported by NSF EAR0909701. We thank D.K. Lynch for introducing us to the field site. We thank Chi-Yuen Wang and the reviewers for their comments.

Chapter 6

Probabilistic Longevity Estimate of the Lusi Mud Eruption

6.1 Abstract

A mud eruption, nicknamed Lusi, began near Sidoarjo, East Java, in May 2006. It has discharged $\sim 10^4 - 10^5$ m^3/day of mud ever since. In order to understand the nature of the eruption and its potential longevity, we develop a model for the coupled evolution of the mud source and ascent of mud through a conduit to the surface. The ascent of the mud is driven by overpressure in the mud source and by the exsolution and expansion of dissolved gases. We assume that erupted fluids originate in the mud source region. Mobilization of the mud is caused by elastic stresses induced by mud evacuation from the subsurface. We perform Monte Carlo simulations to explore model outcomes while perturbing the unknown material properties of the mud and surrounding medium. Using our preferred model, we calculate a 50% chance of the eruption lasting <41 years and a 33% chance that it lasts >84 years. Eruptions often end with the formation of a caldera, but longer eruptions are less likely to form a caldera. Model predictions can be refined with additional, but currently unavailable constraints: more precise estimates of mud discharge, the yielding behavior of the materials in the subsurface, total gas content in the mud source, and identification of any erupted fluids that do not originate in the mud source.

6.2 Introduction

On 29th May, 2006 an eruption of mud and fluids occurred in Sidoarjo, Indonesia, creating a mud eruption named Lusi (short for Lumpur Sidoarjo). Approximately $10^4 - 10^5$ m^3/day of mud has erupted ever since (*Mazzini et al.*, 2007), displacing >60,000 people (*Bayuni*, 2009). The large and active subsidence created by the eruption continues to damage transportation and communication infrastructure.

The birth and evolution of the Lusi eruption are well documented (*Istadi et al.*, 2009; *Mazzini et al.*, 2007) providing a special opportunity to study how and why large mud eruptions occur (*Davies et al.*, 2007). Because the eruption occurred next to a 3 km deep gas exploration well, we also have unique insight into the subsurface lithology and properties immediately prior to the eruption. Specifically, we can constrain the source of the mud, origin of erupted fluids, and the driving mechanism of the eruption.

In this study, we develop a mechanical model for the Lusi eruption that couples mud transport to the surface through a conduit with the evolution of the mud source at depth. The model is analogous to those used for magmatic volcanoes in that there is a mud chamber and a conduit, and dissolved gases play a key role in sustaining the eruption. It differs in that the volume of mobilized mud (analogous to eruptible magma at a volcano) increases over time, owing to progressive mobilization of mud in the source region. We begin by summarizing some of the key observations that guide model development. Next, we describe the model and governing equations. We end by predicting the longevity of the eruption and outline how to test and improve the model.

6.3 Observational Constraints

Microfossils imply a mud source in the upper Kalibeng formation, occurring at depths between 1220-1860 m, which consists of Pleistocene clay (*Sawolo et al.*, 2009). The observed clay mineralogy is most similar to mud from 1600-1800 m (*Mazzini et al.*, 2007). Kerogen compositions of erupted mud are also similar to those obtained from side-wall cores taken at a depth of 1707 m (*Sawolo et al.*, 2009). Drilling logs indicate that the Kalibeng formation is under-compacted and over-pressured, with porosity of about 30% (*Istadi et al.*, 2009; *Tanikawa et al.*, 2010). There is some controversy over the porosity of the Kalibeng formation. Based on density logs from the well Banjar Panji-1 (BJP1) *Davies et al.* (2011) estimate low porosities (10-13%), which would necessitate an external water source.

While there is no debate about the source of mud, there is considerable disagreement about the source of fluid. The water content of the mud during the earliest stages of eruption was 60-70% (*Mazzini et al.*, 2007; *Istadi et al.*, 2009). This is greater than the porosity of the Kalibeng formation, $\sim 30\%$, implying an additional source of fluid. *Davies et al.* (2007) suggest that water is sourced from a carbonate aquifer at depths of 3 km. *Mazzini et al.* (2007) suggest that the primary source of water is diagenesis and dehydration within the source region of the erupted mud. The lower concentrations of B, Li, and Cl, as well as the δ^{18}O enrichment of the water, can be explained by clay dehydration. Carbon isotope measurements of hydrocarbons and methane in the erupted mud indicate the presence of both biogenic methane, which could be produced in the source muds, and thermogenic methane, which, along with heavier hydrocarbons and H_2S, must have migrated from greater depths (*Mazzini et al.*, 2007). The migration could have preceded the eruption.

The reported water content of the erupting mud provides an additional constraint. While the initial water content was high, 60-70% (*Bayuaji et al.*, 2010), it gradually decreased to 30% over the first year (*Mazzini et al.*, 2007). As this value is similar to the porosity of the source layer, we assume there is no significant addition of fluids to the mud source during the bulk of the eruption.

The temperature of the erupting mud is 70-100 °C (*Sawolo et al.*, 2009). The geotherm measured in the BJP1 ($\sim$200 m from the site of the eruption) is 42°C/km and the mean annual air temperature is 27°C (*Bayuaji et al.*, 2010); temperatures of 100 °C are reached at depths of 1700 m (*Mazzini et al.*, 2007). The observed mud temperature does not require the addition of significant amounts of fluid hotter than the temperature at the source depth of the mud.

6.4 Model

We develop a model that is motivated and constrained by these observations. The fluids, mud and gas for the bulk of the eruption are sourced from the Kalibeng formation. Additional fluids may have played a key role in the initiation (*Davies et al.*, 2007; *Tingay et al.*, 2008)

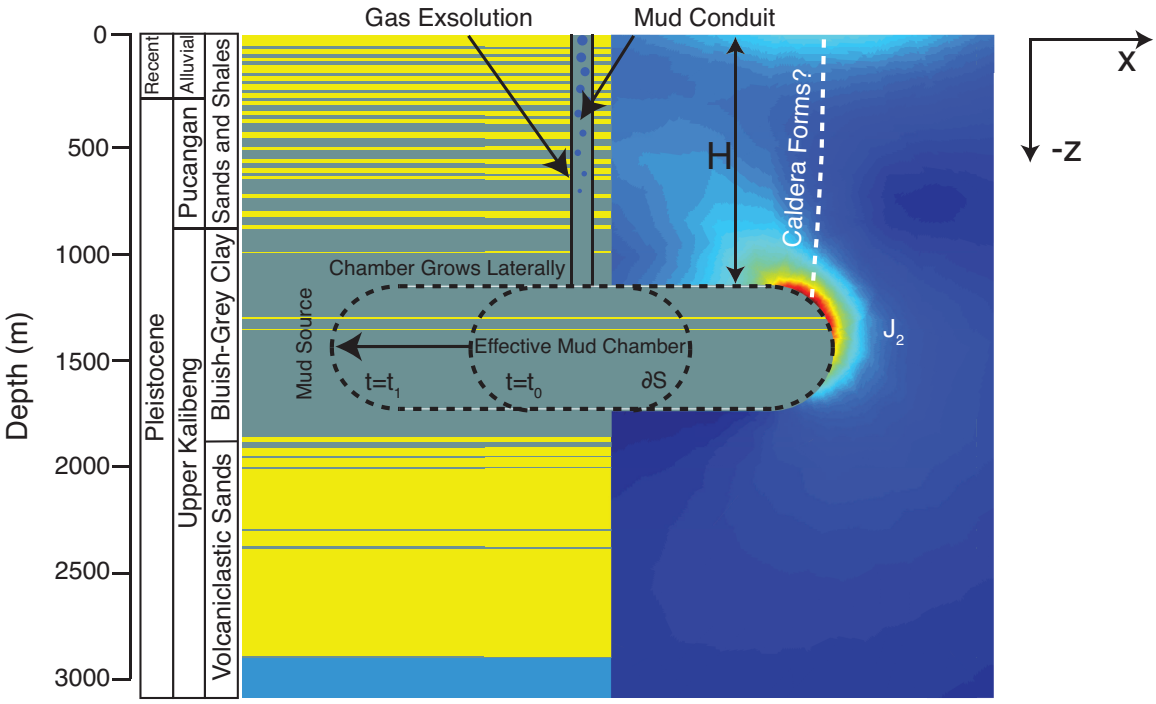

Figure 6.1: An illustration of model geometry and how it relates to subsurface lithology, (left of conduit) and our calculated J_2 (second deviatoric stress invariant), right of conduit. Warmer colors indicate larger values of J_2. Stratigraphy is adopted from (*Mazzini et al.*, 2007) and is based on logs of BJP1.

and during the early stages of the eruption, but will not influence subsequent dynamics, evolution, and longevity.

Our model is conceptually similar to typical models for magmatic volcanoes in that the system consists of a "chamber" coupled to a "conduit". It differs, however, in the nature and origin of the chamber component as well as the boundary condition imposed on the conduit at the surface. For magmatic volcanoes and some mud volcano models (*Zoporowski and Miller*, 2009), the chamber boundary is a material surface and the chamber volume changes owing to influx or outflux during the eruption. In our model, an initially spherical chamber consists of mobilized mud – mud with a rheology that allows it to flow and to erupt. This chamber is surrounded laterally by mud of the same composition that has not yet become mobilized. The lateral extent of the mud chamber is therefore defined by a rheological, rather than a compositional, transition and evolves over time (Figure 6.1). Mud erupts through a cylindrical conduit, driven by gas exsolution and expansion and by chamber overpressure.

Mud Chamber

We model the mud chamber as a cylindrical cavity of thickness 600 m centered at a depth of 1500 m. The edges of the cavity are rounded (Figure 6.1), and the radius of curvature remains constant as the chamber expands. The details of the assumed chamber geometry (e.g. radius of curvature of the edges) are less important than the aspect ratio, which exerts the dominant control on the stress concentration near the lateral boundary of the chamber. For the purposes of calculating stresses outside the chamber, we assume that the continuum surrounding the chamber is a linear elastic solid over the time scale of the eruption. Stresses are governed by

$$\nabla \cdot \underline{\sigma} = \underline{0}, \tag{6.1}$$

where $\underline{\sigma}$ is the Cauchy stress, related to strain ($\underline{\epsilon}$) through the constitutive equation

$$\sigma_{ij} = \lambda \epsilon_{kk} \delta_{ij} + 2\mu \epsilon_{ij}. \tag{6.2}$$

Here λ and μ are the Lamé constants. The model domain is subject to stress boundary conditions at the chamber wall (∂S) and free surface ($z = 0$):

$$\Delta\sigma_n|_{\partial S} = \Delta P_C \tag{6.3}$$

$$\Delta\sigma_n|_{z=0} = \Delta\sigma_t|_{z=0} = 0. \tag{6.4}$$

Here σ_n and σ_t are the normal and tangential stresses, respectively. ΔP_C is equal to the difference between the current pressure in the mud source layer $P_C(t)$ and the initial mud chamber pressure, $P_C(0)$, and obeys the equation of state of the material in the chamber, described later. We calculate elastic stresses and strains numerically, using the axisymmetric program mode in FEAP, version 8.3 (Taylor, 2008). We assume a zero initial stress state, neglecting any effects arising from tectonic stresses.

If we denote the undeformed volume of the cavity $V_{0,C}$ and the deformed volume of the cavity V_C, conservation of mass requires

$$\rho_0 V_{0,C} + \int_0^t \dot{M}(\tau) d\tau = V_C(P)/v_S(P) \tag{6.5}$$

where $\dot{M}$ is the time derivative of chamber mass, which is the opposite of the eruptive mass discharge, and ρ_0 is the in-situ density of the mud at the initial chamber pressure. The equation of state relates specific volume v_S (volume per unit mass) of the 3-phase mixture inside the chamber to pressure P. We perform Newton-Raphson iteration to obtain a chamber pressure that is consistent with the deformed volume of the cavity, the equation of state of the material inside the chamber, and the mass of material remaining in the chamber.

We adopt a von Mises yield stress (and equivalently, strain) criterion for mobilizing additional mud from the chamber's surroundings. The von Mises stress is

$$\sigma_v = \sqrt{3J_2}, \tag{6.6}$$

where J_2 is the second deviatoric stress invariant. As mud erupts from the chamber, the chamber deflates and its pressure decreases, producing stresses in the surrounding mud. Once the von Mises stress in the unmobilized part of the mud layer exceeds a critical value $\sigma_{y,chamber}$ we assume that additional mud is mobilized and becomes part of the chamber. We solve for the expanding chamber radius iteratively so that the von Mises stress at the perimeter of the chamber is everywhere less than the yield stress. The von Mises stress criterion has been used to model mud yielding in other studies (e.g. *Mazzini et al.*, 2009) and is the best higher-dimension analogue to the yielding criterion used to study mudflows in one dimension (e.g. *Marr et al.*, 2002).

Conduit

Mud rises through a conduit towards the surface. The driving force is provided by a combination of mud chamber overpressure, and exsolution of dissolved gas and expansion of vapor during decompression and ascent. We model conduit processes assuming steady one-dimensional multiphase flow through a cylinder, subject to conservation of mass and momentum (e.g. *Mastin*, 2002; *Dobran*, 2001):

$$\frac{\partial}{\partial z}\left(\rho_{mix} u\right) = 0 \tag{6.7}$$

$$\frac{\partial P}{\partial z} = \frac{-\rho_{mix}\left(g + \frac{8\mu u}{\rho_{mix} r^2}\right)}{1 - \frac{u^2}{c^2}}. \tag{6.8}$$

In equations 6.7-6.8, u is the mixture velocity of mud plus gas, P is the pressure, g is gravity, μ is mud viscosity, r is the conduit radius. We note that the term $(8\mu u)/(\rho_{mix} r^2)$ can be interpreted as a friction factor, and any change to conduit geometry (e.g. opening of multiple vents or widening/collapse of the main vent) would simply change the functional form of this term. ρ_{mix} is the mixture density, given by:

$$\rho_{mix} = \left(\frac{n}{\rho_g} + \frac{1-n}{\rho_l}\right)^{-1} \tag{6.9}$$

with n the mass fraction of gas, ρ_g and ρ_l the densities of gas and water plus particles respectively.

$$c = \left(\frac{\partial P}{\partial \rho_{mix}}\right)_S^{1/2} \tag{6.10}$$

is the sound speed of the mixture, calculated numerically to ensure mass conservation.

Equations 6.7-6.8 are solved with a bisection and shooting method and 4th order Runge-Kutta integration to satisfy two boundary conditions: a one-way coupling to the chamber pressure evolution at the base of the conduit

$$P(z = -H) = P_C \tag{6.11}$$

and an atmospheric pressure boundary condition at the surface

$$P(z = 0) = P_{atm} \tag{6.12}$$

We assume that gas bubbles are dynamically coupled to the flow until a critical porosity (gas volume fraction) of 0.3 is reached (*Blower*, 2001; *Saar et al.*, 2001), which we take as a threshold above which all gas is lost. This limits the acceleration of mud in the conduit and effectively ensures that velocities never approach the sound speed of the mixture. We also assume that the water and mud particles are dynamically coupled. *Tanikawa et al.* (2010) estimate permeabilities of 10^{-20} to 10^{-19} m^2 in the Upper Kalibeng Formation. Assuming a driving pressure gradient of 10 MPa/km (estimated from chamber overpressure and conduit length scale), we compute the pore fluid velocity using Darcy's equation as $v = -k/(\mu\phi)\nabla P = 10^{-12}$ m/s, many orders of magnitude smaller than the bulk velocity of the multiphase mixture.

The reservoir (chamber) enthalpy for a given initial temperature (T) and pressure (P) is calculated using the XSteam (www.x-eng.com) implementation of the International Association for the Properties of Water and Steam (IAPWS) IF-97 steam tables. We assume that the ascending mixture experiences isenthalpic decompression during transport (e.g. *Lu and Kieffer*, 2009), allowing us to calculate $T(z)$ from conservation of enthalpy and the steam tables. Once the P-T decompression path is known, we calculate the density and mass fraction of liquid and gas phases, which are functions of T and P, using the CH_4-H_2O equation of state developed by Duan et al. (1992a,b) and implemented in HCO-TERNARY (*Nieva and Barragán*, 2003) and the online calculator at geotherm.ucsd.edu. It is through this calculation that we account for changes in density due to gas exsolution and expansion, and we emphasize that the gas solubility is accounted for through the CH_4-H_2O equation of state and that the conversion of liquid water to vapor during ascent is limited by conservation of enthalpy.

6.5 Model Parameters

Our model contains a number of geometric and material properties, some that are well-constrained and others that are poorly constrained and treated as variables. The following have enough uncertainty to be treated as variables: failure strength of mud adjacent to the chamber ($\sigma_{y,chamber}$), failure strength of the near-surface material ($\sigma_{y,caldera}$), Young's modulus (E), and Poisson's ratio (ν).

Constants

Mud viscosity μ and conduit radius r affect mud ascent through the grouping μ/r^2. *Manga et al.* (2009) measured mud viscosity of 10^5 Pa·s on sample JV07-05 (*Mazzini et al.*, 2007) of Lusi mud with 43 wt.% water. Water content has a large effect on viscosity. Rifai (2008) measured viscosity of samples collected from Lusi and found an approximately 80% increase

in viscosity when water content decreased from 62.5 wt.% to 59.0 wt.%. *Rudolph and Manga* (2010) measured a fivefold increase in mud viscosity when water content decreased from 40 wt.% to 33 wt.%. The geometry of the conduit through which the mud rises cannot be observed directly. The initial fissure, observed within the first few days, was hundreds of meters long and tens of centimeters wide at the surface (*Mazzini et al.*, 2007). Its burial by erupted mud does not allow us to determine how the conduit subsequently evolved and whether discharge became localized, as it does for magmatic fissure eruptions. In March 2007, 10 months after the eruption began, 40 cm diameter concrete balls were able to reach depths of 1000 m (*Mazzini et al.*, 2007). As these balls had no effect on the eruption rate, their size provides a minimum estimate of conduit dimensions. For a given dissolved gas concentration, we choose a combined conduit dimension and viscosity that reproduces the observed 6×10^4 m^3/day mean discharge (Tingay, pers. comm. 2010), emphasizing again that viscosity and conduit radius enter the problem only through the grouping μ/r^2.

The volume ratio of erupted gases is spatially and temporally variable. *Mazzini et al.* (2007) measured gas composition at seeps near the crater and sampled steam clouds emanating from the crater. The seeps discharge 80-85% CH_4 and 10-19% CO_2. The gas samples from the steam cloud are more variable, with CO_2 comprising 28-74% and CH_4 comprising 24-72% of the gas among three samples. In general, the CO_2-enriched samples are also enriched in CX for $X > 1$. We interpret these measurements as indicating a methane-dominated gas composition, following two lines of reasoning. First, CO_2 (specific gravity 1.53) and CX, X$>$ 2 are denser than air while CH_4 is lighter than air (specific gravity 0.56). The steam samples were collected downwind of the crater, and some separation of gases by density may have occurred during transport. Second, we expect that the local gas seep chemistry, which is methane-rich, will be dominated by the composition of the erupting fluids. However, subsequent measurements may indicate that the erupting gas composition is CO_2-dominated (Mazzini, pers. comm. 2011). In our model, the gas composition is unimportant. As long as the discharge at initial chamber pressure fits the observational constraint, the relationship between chamber pressure and discharge is independent of gas composition. We show this graphically in Figure 6.2. The only discrepancy in cumulative mass removed (Figure 6.2) for the model using CO_2 and the model using CH_4 arises from a small mismatch in flux, less than 5%, the tolerance that we chose when calculating conduit velocities as a function of chamber pressure.

Unknowns

The value of $\sigma_{y,chamber}$ for the mud source is not known. *Kopf et al.* (2009) measured sediment shear strength *in situ* in the field (at the Dashgil mud volcano, Azerbaijan) using a Cone Penetration Test. They found strengths as low as 150 kPa in the conduit and 300-700 kPa at other locations. We thus consider values of $\sigma_{y,chamber}$ with a mean of 1 MPa for the pre-mobilized mud, and a standard deviation of an order of magnitude in log-space. Once the mud loses strength and enters the chamber or flows in the conduit, we treat it as a viscous fluid. The value of $\sigma_{y,caldera}$ is also unknown, and we assume that it is 10 times

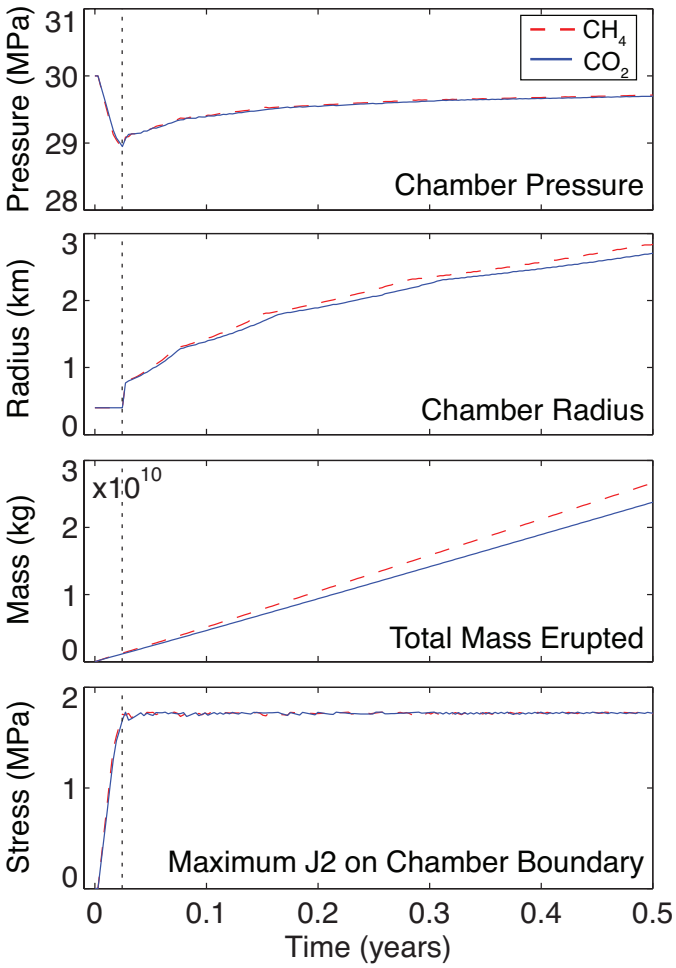

Figure 6.2: Temporal plots for one model realization showing chamber pressure, chamber (mobilized region) radius, cumulative mass erupted, and maximum J_2 on the chamber boundary (top to bottom). The red dashed lines are from a model in which we used 0.5 mol % CH_4 while the blue curves are for a model with 1 mol % CO_2. The two models are otherwise identical. The most important feature of the model results, illustrated here, is that once yielding begins (indicated by dashed vertical line), there is a drastic change in system behavior. Chamber radius begins to increase, and chamber pressure is buffered by the incorporation of material with higher pore pressure than that of the material filling the chamber prior to expansion. Like chamber pressure, mass flux is buffered and varies only by about 1% and J_2 remains constant at the value of the yield strength ($\sigma_{y,chamber}$).

Symbol	Value (or Mean)	Standard Deviation	Description
$\log_{10}$(E (Pa))	8	1	Young's modulus
ν	0.15	0.1	Poisson's ratio
$\log_{10}(\sigma_{y,chamber}$(Pa))	6	1	Yield strength of mud source layer
$\sigma_{y,caldera}$	10 $\sigma_{y,chamber}$	N/A	Yield strength of near-surface material
μ	10^4 Pa s	N/A	Viscosity in conduit
r	1.4 m	N/A	Conduit radius
$[CH_4]$	0.5 wt %	N/A	CH_4 mole fraction
$[CO_2]$	1 wt %	N/A	CO_2 mole fraction

Table 6.1: Summary of the values for model parameters. The means and standard deviations listed were used in our Monte Carlo simulations.

Prior PDF Shape	Gaussian	σ boxcar	2σ boxcar
33% Longevity (years)	21	27	14
50% Longevity (years)	40	50	25
75% Longevity (years)	84	>100	52

Table 6.2: Summary of model results for both choices of gas composition and different assumptions about the distribution of model unknowns. Models with gaussian pdfs use the means and standard deviations shown in Table 6.1. Models with σ-boxcar and 2σ-boxcar distributions use mean values and standard deviations (σ) from Table 6.1 and assume a flat pdf within σ or 2σ of the mean.

larger than $\sigma_{y,chamber}$. We experimented with values of $\sigma_{y,caldera}/\sigma_{y,chamber}$ as large as 100 but found it to be unimportant. We explore a range of values for E (Young's modulus) and ν (Poisson's ratio) for the surroundings centered about 10^8 Pa and 0.15, respectively, chosen to be consistent with the geodetic modeling of *Fukushima et al.* (2009).

The mean values and range of parameters used in the Monte Carlo simulations are summarized in Table 6.1. We considered three scenarios. In the first, our preferred model, we give more weight to values of unknown parameters near our preferred mean value by using gaussian distribution of random numbers. E and $\sigma_{y,chamber}$ have values that are normally distributed in log-space, i.e. $\log_{10}(\sigma_{y,chamber}\ (\text{Pa})) = 6 \pm 1$. We also performed the same suite of Monte Carlo simulations with probability density functions (pdfs) that are constant in the range $[mean - \sigma, mean + \sigma]$ or $[mean - 2\sigma, mean + 2\sigma]$ and zero elsewhere. We refer to these as σ-boxcar and 2σ-boxcar, respectively (Table 6.2).

6.6 Criteria to Terminate Eruption

The factors that cause eruptions to end are, in general, poorly understood. We consider two possible scenarios. First, the chamber pressure decreases (sometimes below lithostatic pressure) until there is insufficient potential energy available to drive the eruption. Alternatively, the eruption may end if the near-surface material fails, initiating caldera formation. The latter condition does not require that the eruption has ended, just that it has entered a regime in which our model is no longer applicable. Caldera formation occurs if continued removal of material induces failure of the overlying layers, and becomes more likely as the chamber grows and deviatoric stresses are concentrated between the surface and regions of high curvature at the chamber walls. We evaluate J_2 (second deviatoric stress invariant) along a trajectory that begins at the tip of the mud chamber and progresses upward always in the direction of greatest J_2. We then evaluate J_2 along this trajectory at half the chamber depth. If the value at this point is greater than $\sigma_{y,caldera}$, we assume that a caldera forms. This method produces a conservative criterion for caldera formation because J_2 is greatest at the free surface and decreases with increasing depth.

6.7 Results

To predict longevity, we performed Monte Carlo simulations in which we perturbed the four unknown model parameters. We illustrate the evolution of chamber pressure, chamber radius, total mass removed, and mass flux as a function of time during an individual Monte Carlo realization in Figure 6.2. Of 2584 simulations, 1223 eruptions ended due to chamber underpressure, 725 formed a caldera, 397 lasted longer than 100 years (the maximum time allowed for computational purposes), and 239 produced unbounded chamber growth (which is not geologically reasonable, as the mud source has finite lateral extent). In general terms, eruptions that ended due to insufficient chamber pressure never incorporated additional mud into the chamber because $\sigma_{y,chamber}$ was large; those that produced unbounded growth had the lowest $\sigma_{y,chamber}$. Caldera formation was favored by larger E and low $\sigma_{y,chamber}$. Our mean $E = 10^8$ Pa (*Fukushima et al.*, 2009) and $\sigma_{y,chamber}$ lie close to the line that divides model outcomes in E-$\sigma_{y,chamber}$ space (Figure 6.3). Poisson's ratio is unimportant.

Although short eruptions are the most frequent model outcome, the observation that Lusi has been erupting for more than 4.5 years provides an additional constraint. If we exclude all eruptions shorter than 4.5 years and give equal weight to all durations greater than 4.5 years, we obtain the cumulative probability distribution shown in Figure 6.4. The Gaussian model predicts that the eruption has a 33% chance of lasting <21 years, a 50% chance of lasting less than 40 years, and a 67% chance of lasting <84 years. The σ-boxcar and 2σ-boxcar model results are summarized in Table 6.2.

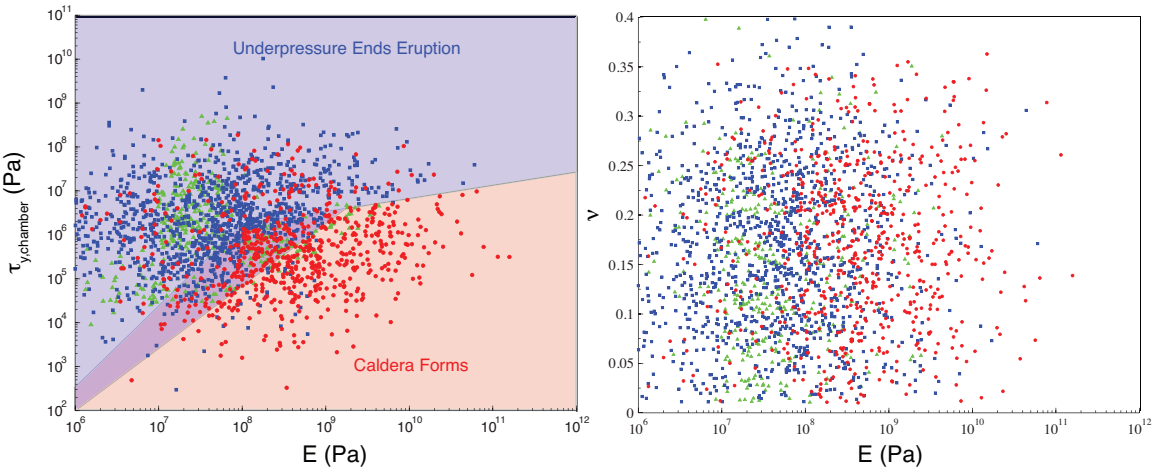

Figure 6.3: Regime diagram illustrating effect of variables on model outcome (gaussian model). Each glyph represents one model realization and colors/shapes correspond to outcomes: blue squares - insufficient chamber pressure ends eruption, red circles - caldera forms, green triangles - eruption lasts longer than 100 years.

6.8 Discussion

Eruptions driven by overpressure have approximately exponentially decaying discharge because the mass removal decreases overpressure (*Woods and Huppert*, 2003). In contrast, to date the Lusi eruption has displayed a remarkably uniform discharge, varying only by less than a factor of ten over the first few years. Eruption rates are difficult to determine accurately and the Lusi eruption is no exception. In the first few months discharge was about 50,000 m^3/day and increased to as much as 180,000 m^3/day over the next year (*Mazzini et al.*, 2009). Satellite observations are most consistent with average eruption rates of 90,000 m^3/day (*Istadi et al.*, 2009). Our model produces approximately constant eruption rates for a given conduit size because once the chamber begins expanding, the chamber pressure is buffered by incorporating additional material. Changes in observed eruption rates could reflect evolution of the conduit geometry or opening of new conduits, phenomena not captured by our model.

Mud volcanoes are known to form calderas (*Kopf*, 2008). *Evans et al.* (2008) describe mud calderas, both on land and submarine, with diameters of 1-2 km. Figure 6.3 shows that E and $\sigma_{y,chamber}$ are the key variables controlling caldera formation. Figure 6.5 is a histogram of eruption duration, also showing the breakdown between eruptions that end due to chamber underpressure and eruptions culminating in the formation of a caldera. Eruptions that last longer are more likely to end due to chamber underpressure and less likely to form a caldera. Figure 6.6a is a histogram of caldera radii, which we assume to be equal to the

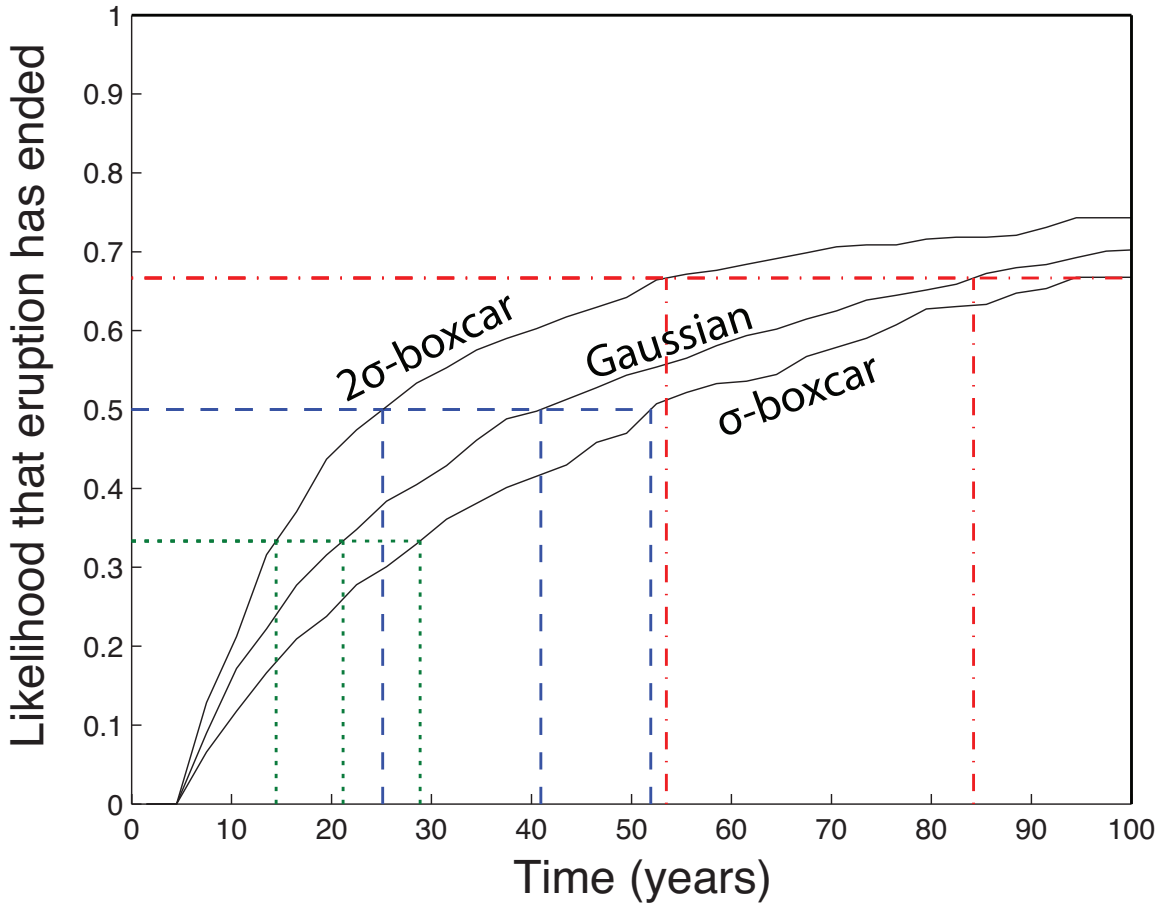

Figure 6.4: Cumulative probability that the eruption has ended for all three distributions of unkown variables. Horizontal axis is time since eruption started, vertical axis is likelihood that eruption will have ended or formed a caldera. Green dotted, blue dashed, and red dot-dashed lines indicate times at which likelihood is 1/3, 1/2, and 2/3, respectively.

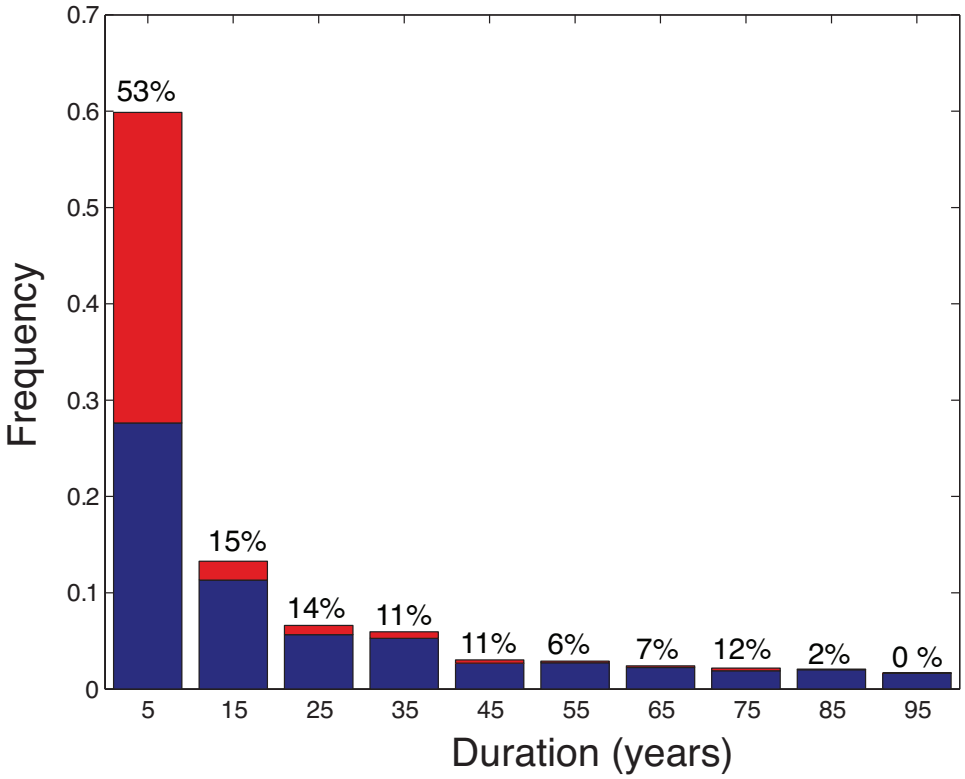

Figure 6.5: Histogram of eruption durations for gaussian model. Red bars indicate eruptions that formed a caldera and blue bars indicate eruptions that ended due to insufficient chamber pressure. We list the percentage of the eruptions in a given bin that ended due to caldera formation.

chamber radius at the time of caldera formation. The calderas formed by our model most frequently have radii less than 2 km, although larger calderas can form. Figure 6.6b is a scatter plot of caldera radius as a function of time of formation. The positive-sloping trend of this plot implies that longer-lasting eruptions tend to form larger calderas, as expected.

There are two other models for the future of the Lusi eruption. The first, by *Istadi et al.* (2009) assumes an eruption rate and uses a GIS approach to account for subsidence and ponding of mud on the surface. As it does not address the controls of eruption rate and processes driving the mud to the surface we do not discuss it further. This model does, however, address a feature of the eruption that we neglect, namely the emplacement and redistribution of the mud after eruption.

Davies et al. (2011) develop a model that is more similar in approach to our own in that they model the mechanics of the eruption process and mass transport. The model differs significantly, however, in the inferred source of the fluids that mix with the mud, the plumbing system for the fluids and mud, and the driving forces for the eruption. *Davies*

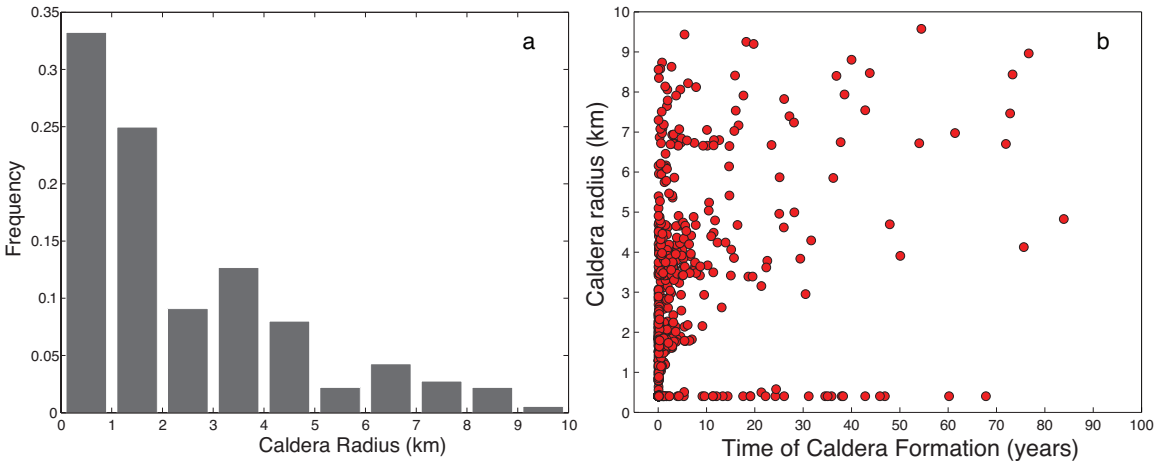

Figure 6.6: (a) Histogram of caldera radii for gaussian model. Frequency of radii of caldera formed in the model, normalized so that bins sum to 1. (b) Relationship between caldera radius and time of formation.

et al. (2011) assume that water from a deep artesian carbonate aquifer flows upwards into the 15 cm-diameter borehole created by drilling operations. At the depths of the mud source, 1.8-1.6 km, the water exits the conduit, mixes with mud in something analogous to our mud chamber, and then erupts. The driving mechanism is overpressure in the carbonate aquifer, and water from this aquifer entrains mud and carries it to the surface. Our model thus differs conceptually in two important respects: the importance of the deep carbonate aquifer, and the driving forces. We have argued that a source of extra fluid is not needed after the initial phases of the eruption. Without this additional source of overpressure, our eruption is sustained by exsolution and expansion of gases derived from the mud source region. We note that the 50th percentile eruption duration predicted by *Davies et al.* (2011) is 26 years, substantially less than we predict without invoking an external fluid source. We expect that the addition of an external source of fluids (and overpressure) to our model would increase the duration of our model eruptions.

6.9 Conclusions

In summary, we considered two possible scenarios under which the current eruption may end, either through the eventual inability of dissolved gases to sustain the eruption, or the formation of a caldera. We made some necessary simplifications in order to develop a tractable model, most importantly the assumption of constant conduit geometry and uniform material properties of the mud source and surroundings. There is also considerable uncertainty

in mechanical properties such as viscosity, failure strength of the mud, initial gas content, and origin of additional fluids. However, once we constrain the model to produce the observed eruption rate, uncertainty in viscosity and gas content have little effect on longevity predictions.

Validating our conceptual model is necessary for its predictions to be relevant and useful for planning. It should be possible to demonstrate the existence and amount of additional fluids (*Davies et al.*, 2007, 2011) by sampling fluids from the mud source and deeper aquifers, and comparing these with samples of the erupted mud. There is also some ambiguity in the measurements of gas composition, and the collection of gas samples directly from Lusi's crater would better inform our model parameters. We have also neglected to include aspects of regional tectonics that may influence the eruption, particularly if the mud source expands. Perhaps most important is the role of stresses from the reactivated Watukosek fault that passes through the eruption source (*Mazzini et al.*, 2009). The spatial correlation of mud volcano locations with the fault suggests that the fault influences at least the location of the eruptions. Our treatment of mud rheology and mobilization is simplified, as mud failure and flow are complicated. Finally, our treatment of the region surrounding the mud chamber as elastic cannot account for surface cracks and motion on nearby faults, features that suggest brittle failure or plastic deformation. Despite the uncertainties in material properties and the model approximations, our modeling framework allows us to make probabilistic estimates of longevity and to highlight how predictions can be improved in light of better observational constraints.

Acknowledgments

This work was supported by the National Science Foundation under Grant No. EAR-1114184. We thank A. Mazzini for providing mud samples and R. Swarbrick and R. Davies for discussions and for sharing their work. M.L.R. is supported by a Graduate Research Fellowship from the National Science Foundation. We thank Adriano Mazzini and two anonymous reviewers for comments that substantially improved the quality of the manuscript.

Chapter 7

Internal Dynamics and Longevity of Lusi Constrained by Ground Deformation

7.1 Introduction

The ongoing eruption of the Lusi mud volcano, East Java, Indonesia (Figure 7.1) offers the unprecedented opportunity to study a large eruption from its beginning to its eventual end. This eruption has devastated local communities, displacing more than 60,000 people and causing >$4B in economic losses (*Richards*, 2011). Despite significant efforts to understand the eruption and predict its longevity (*Istadi et al.*, 2009; *Davies et al.*, 2011; *Rudolph et al.*, 2011), the spatiotemporal evolution of the source feeding the eruption is not well understood. Here we combine new observations of ground deformation and a model relating subsurface dynamics to ground deformation to show that Lusi will stop erupting much sooner than previously anticipated (*Istadi et al.*, 2009; *Davies et al.*, 2011; *Rudolph et al.*, 2011), and that the evolution of mud chamber geometry and pressure reflect progressive mobilization of mud. Progressive mobilization has never been directly observed and is a process that may play an important role during large mud volcano eruptions (*Rudolph et al.*, 2011) as well as caldera-forming supervolcano eruptions (*Karlstrom et al.*, 2012). Previous assessments of the hazard posed by Lusi relied upon estimates of discharge during the first three years of the eruption (*Mazzini et al.*, 2007; *Tingay et al.*, 2008; *Istadi et al.*, 2009), concluding that the eruption will last 23-40 years (*Istadi et al.*, 2009; *Davies et al.*, 2011; *Rudolph et al.*, 2011). We find that the pressure driving the eruption is decreasing exponentially and that discharge will decrease to 10% of the present rate in 6 years.

Like magmatic volcanoes, Lusi erupts a three-phase mixture of solid particles, liquid, and gas. The three phases may all come from the location or multiple reservoirs may be involved in the eruption (*Davies et al.*, 2011; *Rudolph et al.*, 2011). Microfossils, temperature, mud composition, and kerogen compositions (*Mazzini et al.*, 2007; *Sawolo et al.*, 2009) indicate that the erupting mud comes from the Upper Kalibeng formation, between 1200 and 1800 m depth (Figure 7.2).

7.2 Methods

We measured ground deformation near Lusi using interferometric processing (*Berardino et al.*, 2002) of 46 L-band radar images acquired by the ALOS satellite between October 8, 2006 and April 21, 2011. We list the dates of acquisition in Table 7.1 and details of the processing procedure in Section 7.5. The cumulative displacements during the period of study are shown as contours in Figure 7.1 and intermediate displacements in Figure 7.3.

We calculated radial profiles of vertical displacement from the observations by averaging azimuthally between 1750 and 4000 m from the main vent location (Figure 7.1) with azimuths between 67.5° and 202.5° measured clockwise from North. Other azimuths are affected by gas extraction from a nearby well. Displacements at distances closer than 1750 m are complicated by disruption of the land surface and mud flow emplacement.

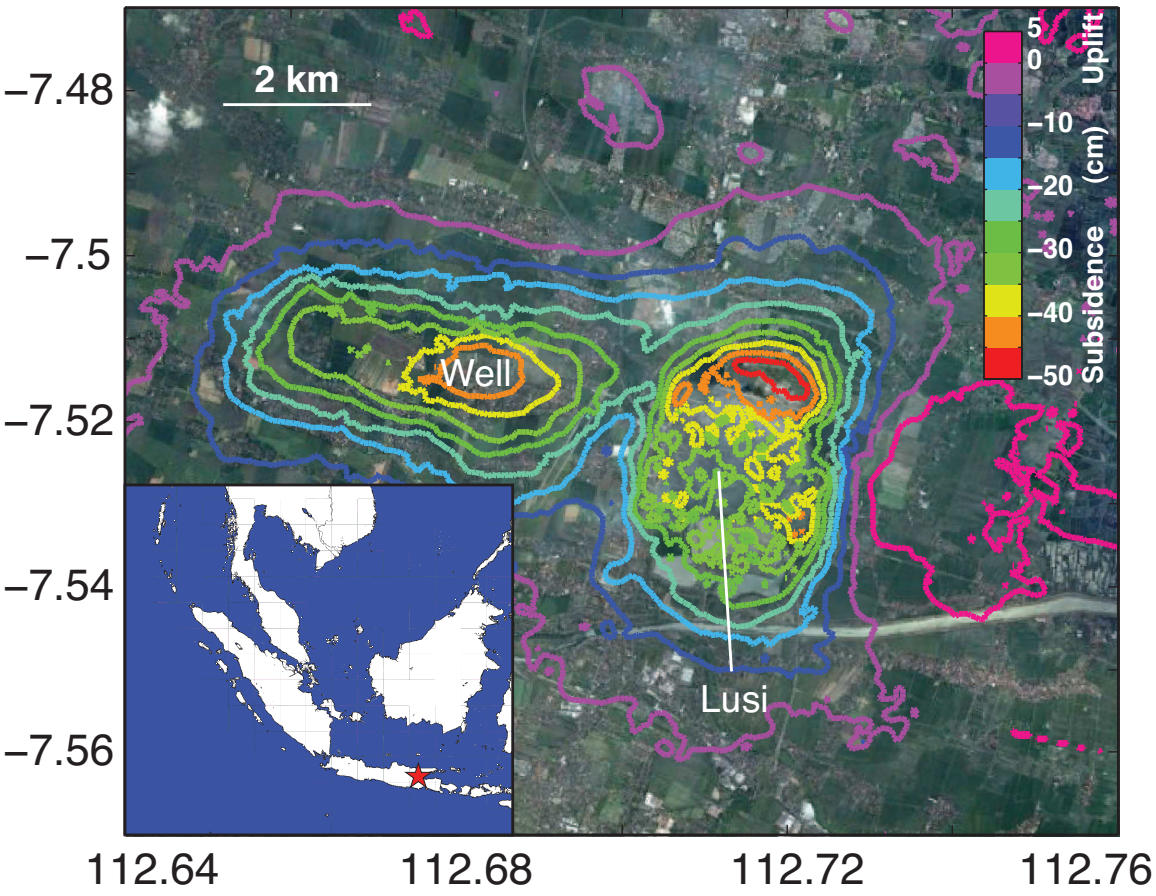

Figure 7.1: Contour plot of cumulative vertical displacement showing subsidence due to Lusi and a nearby well between October, 2006 and April, 2011. The inset shows Lusi's location in East Java.

7.3 Discussion

We attribute surface displacements to pressure changes in a disc-shaped mud chamber. Because the source of mud is unambiguous, we assume that the chamber is located between 1200 and 1800 m depth (geometry illustrated in Figure 7.2). The model is purely kinematic and makes no assumptions about the time evolution of any aspect of the eruption; the radius of the chamber and the pressure change are the only free parameters. At each of the 45 timesteps, we minimized the misfit between observed and modeled displacements to determine the best-fit chamber radius and pressure (Figure 7.5). We plot the misfit in Figure 7.4.

The best-fitting model has three phases (indicated in Figure 7.5). First, the chamber radius remained close to 0.7 km while pressure decreased. Second, chamber radius increased between March and June 2007 to 1.3 km. During the second phase, chamber pressure

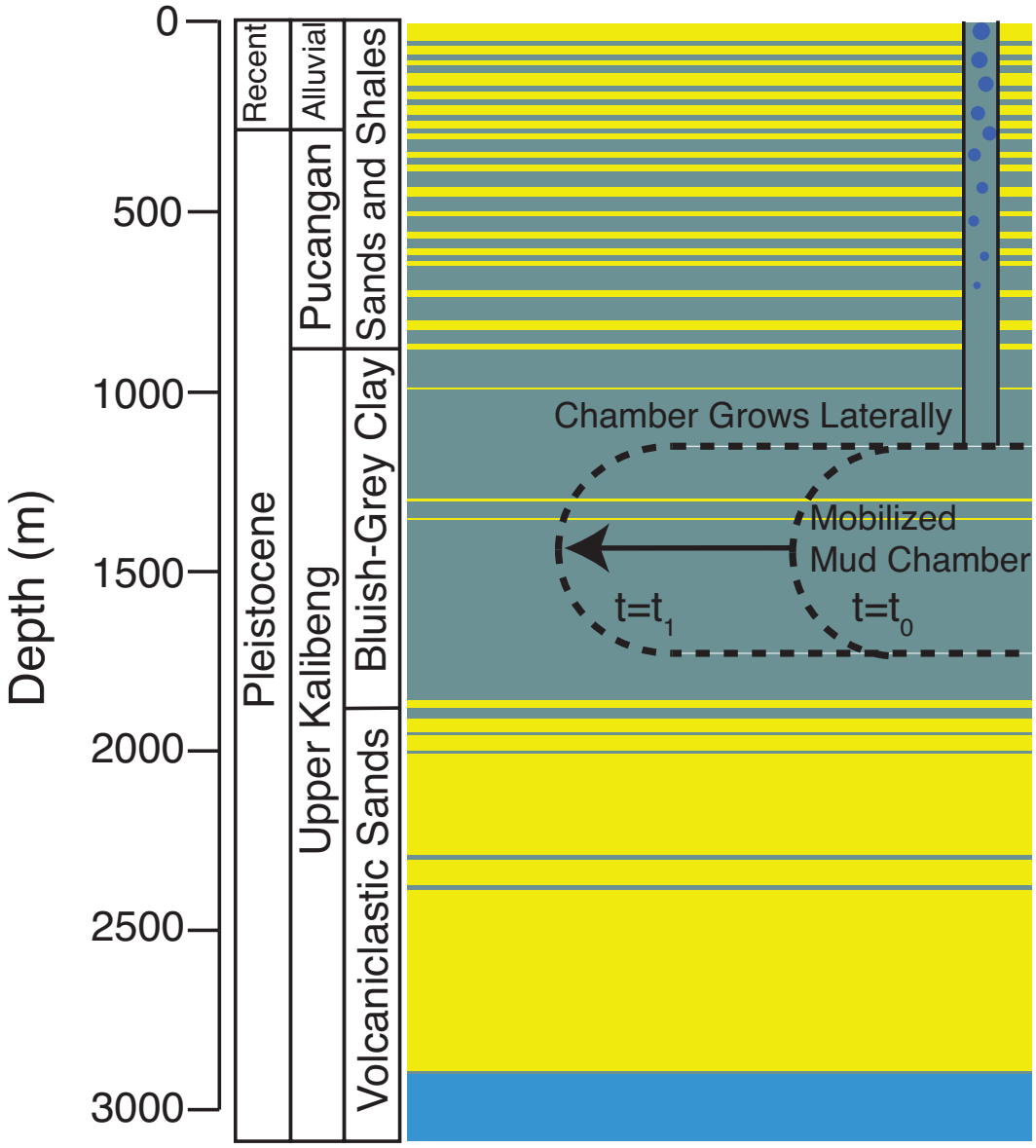

Figure 7.2: Model geometry superimposed on a stratigraphic section (*Mazzini et al.*, 2007).

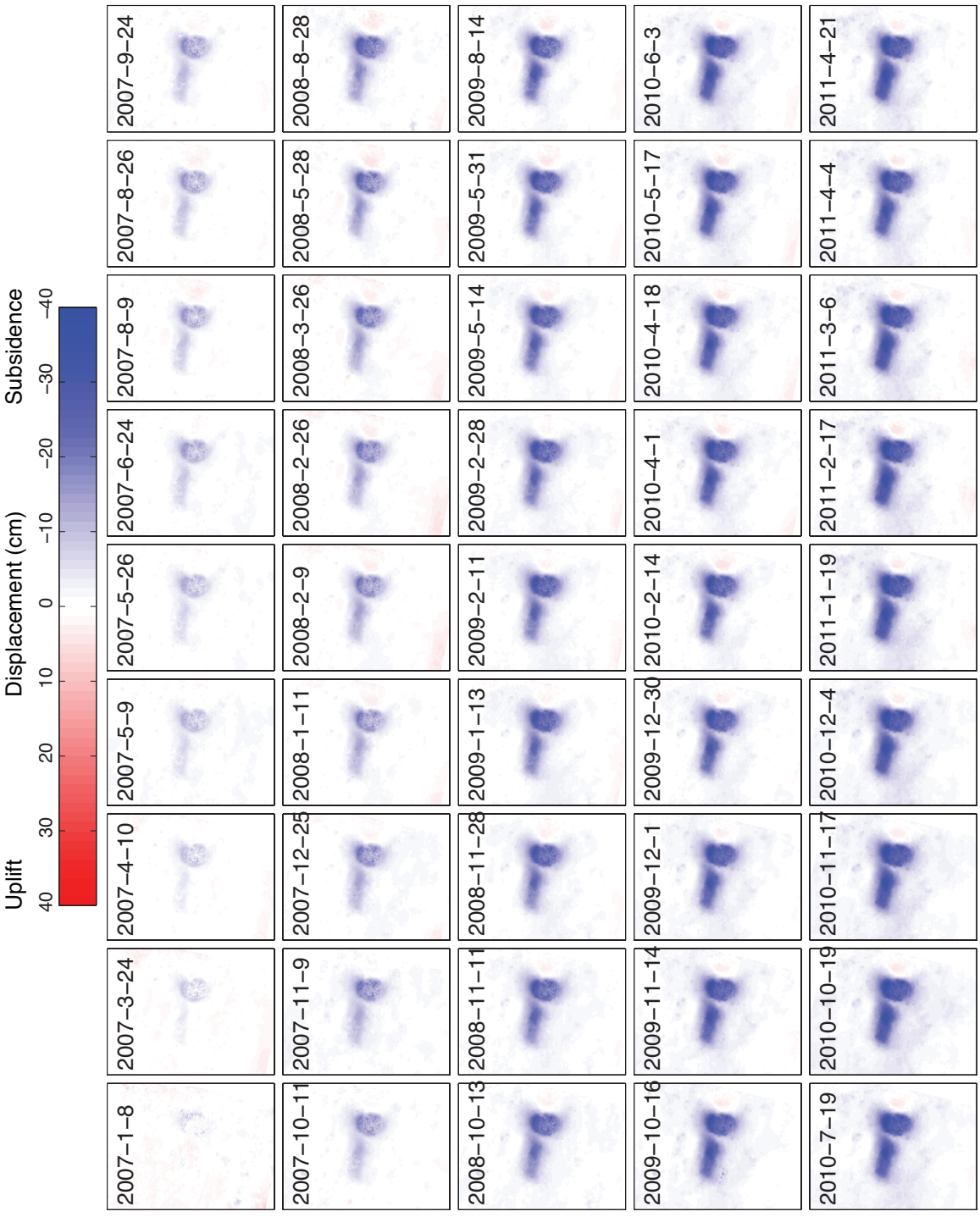

Figure 7.3: Cumulative vertical ground displacement since October 8, 2006.

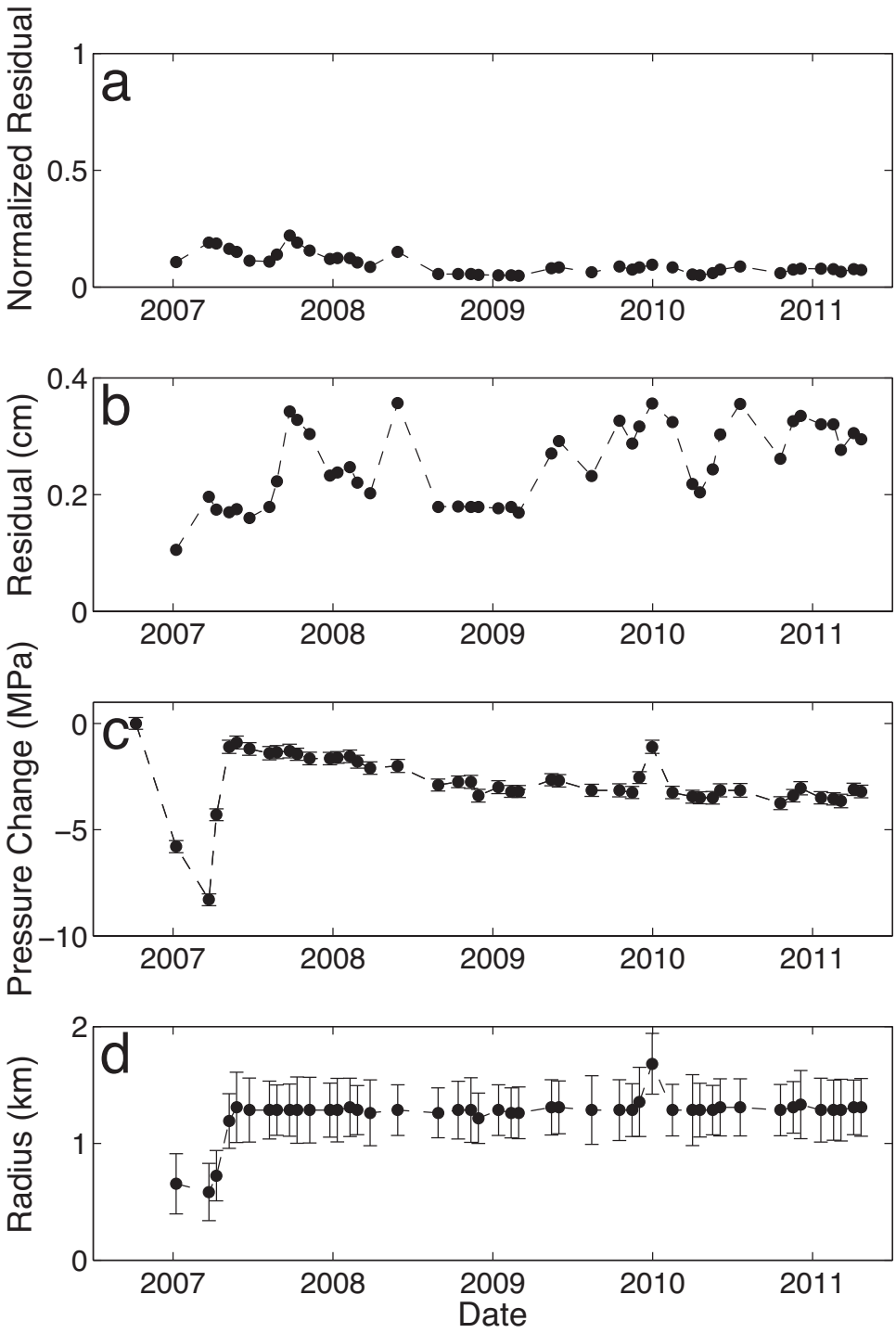

Figure 7.4: (a) Normalized residual and (b) residual, described in Section 7.5. (c) and (d) show pressure change and radius with 2-σ error bars.

Year	Month	Day	Path	Frame	Year	Month	Day	Path	Frame
2006	10	8	92	3770	2009	2	11	91	3770
2007	1	8	92	3770	2009	2	28	92	3770
2007	3	24	91	3770	2009	5	14	91	3770
2007	4	10	92	3770	2009	5	31	92	3770
2007	5	9	91	3770	2009	8	14	91	3770
2007	5	26	92	3770	2009	10	16	92	3770
2007	6	24	91	3770	2009	11	14	91	3770
2007	8	9	91	3770	2009	12	1	92	3770
2007	8	26	92	3770	2009	12	30	91	3770
2007	9	14	91	3770	2010	2	14	91	3770
2007	10	11	92	3770	2010	4	1	91	3770
2007	11	9	91	3770	2010	4	18	92	3770
2007	12	25	91	3770	2010	5	17	91	3770
2008	1	11	92	3770	2010	6	3	92	3770
2008	2	9	91	3770	2010	7	19	92	3770
2008	2	26	92	3770	2010	10	19	92	3770
2008	3	26	91	3770	2010	11	17	91	3770
2008	5	28	92	3770	2010	12	4	92	3770
2008	8	28	92	3770	2011	1	19	92	3770
2008	10	13	92	3770	2011	2	17	91	3770
2008	11	11	91	3770	2011	3	6	92	3770
2008	11	28	92	3770	2011	4	4	91	3770
2009	1	13	92	3770	2011	4	21	92	3770

Table 7.1: Acquisition dates, paths, and frames corresponding to the ALOS PALSAR data used in our study.

increased. Third, after reaching a radius of 1.3 km in June 2007, the mud chamber stopped expanding and pressure decreased exponentially with an e-folding time scale of 2.8 years.

We interpret the three phases of Lusi's eruption in the context of a conceptual model for mud volcanoes (*Rudolph et al.*, 2011) in which mud is drawn from a chamber whose lateral boundaries are defined by a yield surface (Figure 7.2) separating mobilized from unmobilized mud. When material is removed from the mud chamber, its surroundings deform elastically and stresses are produced in unmobilized mud adjacent to the chamber. When these stresses become sufficient to overcome the unmobilized muds yield stress, mobilization occurs and the yield surface expands outwards as new material is incorporated into the mud chamber. There is direct observational evidence for such a transition occurring at depth after Lusi began erupting. Prior to the eruption, the well Banjarpanji-1 was installed without casing in the Upper Kalibeng, indicating that the material had sufficient strength to prevent collapse (*Tingay et al.*, 2008). After the initiation of the eruption, relief wells were unable to penetrate

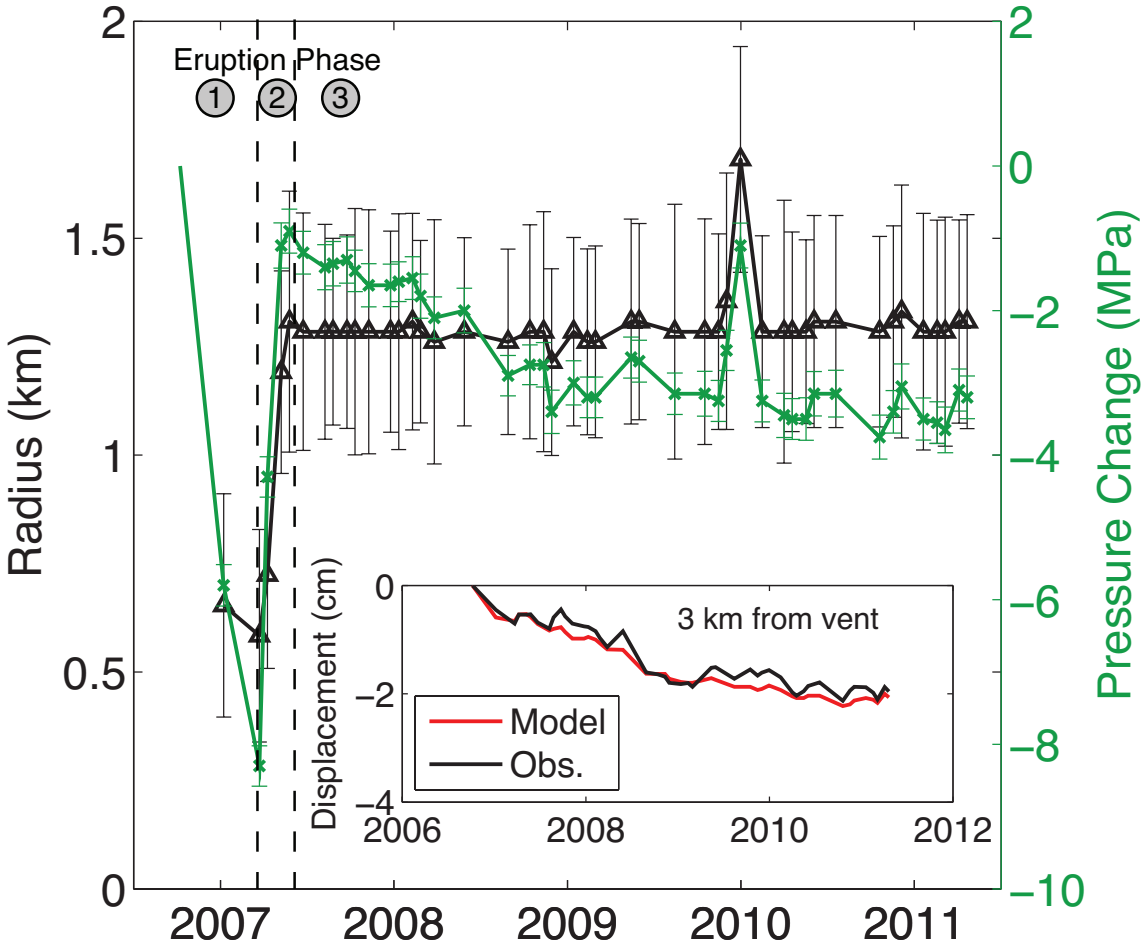

Figure 7.5: Best-fitting chamber radius (black) and pressure change (green) with 2-σ error bars. Deformation was measured relative to the first SAR acquisition, October 8 2006, resulting in zero pressure change and undefined radius for this first acquisition. The black vertical dashed lines separate the three phases of the eruption discussed in the text. Inset shows model and displacements and stacked observed displacements at one point.

the Upper Kalibeng due to sidewall collapse (*Sutrisna*, 2009), indicating that a rheological transition had taken place.

During the first phase of the eruption, between October 2006 and March 2007, pressure decreased, as is expected when material is removed from a chamber with fixed spatial boundaries (*Woods and Huppert*, 2003; *Zoporowski and Miller*, 2009). The mud chamber did not expand during this phase because stresses produced in the surrounding unmobilized mud were insufficient to overcome the materials yield stress.

The second phase of the eruption began when the yield stress of mud surrounding the chamber was exceeded. The mud chamber expanded spatially as mud was progressively mobilized and incorporated into the chamber. Chamber pressure increased during this phase, the expected behavior when material with pore pressure in excess of the chamber pressure becomes mobilized. Pore pressure in the unmobilized mud adjacent to the chamber is expected to remain very close to its pre-eruptive value owing to very small hydraulic conductivity (*Tanikawa et al.*, 2010).

The third phase of the eruption is characterized by stable chamber geometry and exponentially decreasing pressure. The maximum radius probably reflects structural control (*Roberts et al.*, 2011). Seismic reflection profiles (*Sawolo et al.*, 2009) reveal several faults that offset the Upper Kalibeng formation within 2 km of Lusi that could serve as physical barriers to expansion.

The evolution of radius and pressure bear striking resemblance to models of crystal-rich silicic magma chambers in which magma is progressively mobilized during the course of an eruption (*Karlstrom et al.*, 2012). Like mud, sufficiently crystal-rich magmas have a yield stress. The withdrawal of magma from a rheologically-locked magma chamber results in the same progressive mobilization and pressure-buffering that we infer to have occurred in Lusi (*Rudolph et al.*, 2011). Because this process is only likely to be important in the largest explosive volcanic eruptions in the geologic record, Lusi provides a unique opportunity to study progressive mobilization in an analogous mud volcano system.

7.4 Implications for Longevity

Discharge from Lusi was initially 10^5 m^3/day in 2006 (*Mazzini et al.*, 2007) and has subsequently decreased to 10^4 m^3/day (*Mazzini et al.*, 2012). Since reaching a steady radius, chamber pressure has been decreasing exponentially, implying a 10-fold decrease in discharge to $< 10^3$ m^3/day by 2018^{+7}_{-2} years, assuming that mud viscosity, gas content, and conduit geometry remain unchanged. The exponential pressure decay inferred from our model is corroborated by principle component analysis of the deformation data. The first principal component, whose spatial pattern is shown in Figure 7.6, accounts for 90% of the variance in the deformation time series. The temporal coefficient for this spatial pattern is well approximated by an exponential function with an e-folding time scale of $2.95^{+1.0}_{-0.6}$ years (Figure 7.6), in good agreement with the exponential fit to the pressure time series recovered from our kinematic model.

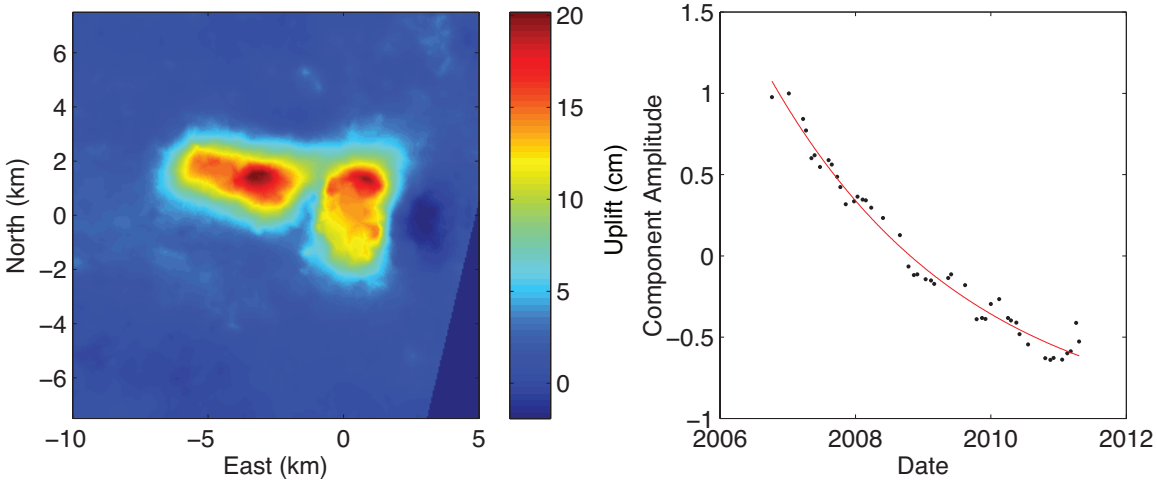

Figure 7.6: Results of principle component analysis of ground deformation data. (left) Spatial pattern associated with first principal component. (right) Temporal weighting coefficient (black) and a best fit exponential curve (red). Both positive and negative values are expected because the deformation described by PCA is measured relative to the temporal mean displacement. The first principle component accounts for 90% of the variance in the dataset.

The anticipated longevity based on geodesy presented here is much shorter than the prediction made in Chapter 7, based on a probabilistic model for Lusi. The ground deformation time series presented here constitutes an important observational constraint that was not available when the study presented in Chapter 7 was carried out. Hence, while we do find compelling evidence favoring the conceptual model presented in Chapter 7, the longevity prediction based on the probabilistic model is likely less reliable than the prediction presented here. The new geodetic observations allow us to rule out some proposed scenarios and imply a much shorter-lived eruption than previously anticipated (*Istadi et al.*, 2009; *Davies et al.*, 2011; *Rudolph et al.*, 2011).

7.5 Supplementary Methods

To generate a time series of the surface deformation field for over Lusi, we employ a multiple-master SAR interferometry approach following earlier works (*Berardino et al.*, 2002). Given 21 and 25 SAR scenes acquired during 2007-2011 in descending orbit mode (Azimuth = 188° and Incidence angle = 34.3°) of ALOS PALSAR satellite, we generated 400 interferograms. The geometrical phase is estimated and subtracted using satellite precise ephemeris data and a reference SRTM digital elevation model of 90 m resolution (*Franceschetti*, 1999). To obtain an unambiguous phase observation from modulo 2π phase change measured in each interferogram, we use a 2D phase unwrapping operator (*Chen and Zebker*, 2001) and apply

it to high quality pixels in the image (*Costantini and Rosen*, 1999). The algorithm for identifying high quality pixels is based on maps of coherence (*Costantini and Rosen*, 1999). Then, each data set is inverted using a linear unbiased estimation approach (*Bjerhammar*, 1973) to generate the time series of the displacement field. By applying a temporal high pass and spatial low pass filter we reduce the effect of atmospheric delay on the displacement time series (*Ferretti et al.*, 2001).

Our finite element model for ground deformation is axisymmetric and assumes homogenous and isotropic linear elastic behavior. We used elastic moduli $E = 10^{10}$ Pa and $\nu = 0.25$. Our model has a free surface and the mud chamber boundary has no shear traction and a normal traction equal to the chamber pressure. We performed the numerical calculations using FEAP (*Taylor*, 2011).

The residuals shown in Figure 7.4 are measures of the misfit between observed (o) and modeled (m) displacements. The modeled and observed displacements are represented as vectors whose entries are displacements at discrete points r_i between radii $r = r_{\min}$ and $r = r_{\max}$. We define the discrete displacement residual as the 2-norm of the misfit weighted by an area element dA_i

$$\mathrm{dA}_i = \pi(r_{i+1/2}^2 - r_{i-1/2}^2) \tag{7.1}$$

$$\text{residual} = \frac{\sqrt{\sum_i \left[(o_i - m_i)\mathrm{dA}_i\right]^2}}{\sqrt{\sum_i \mathrm{dA}_i^2}} \tag{7.2}$$

We also define a normalized residual representing the misfit normalized by the observed displacements:

$$\text{normalized residual} = \frac{\sqrt{\sum_i \left[(o_i - m_i)\mathrm{dA}_i\right]^2}}{\sqrt{\sum_i (o_i \mathrm{dA}_i)^2}} \tag{7.3}$$

Chapter 8

Mechanics of Calistoga Geyser from Ground Deformation

8.1 Abstract

In order to probe the subsurface dynamics and plumbing of geysers, we measured ground deformation at Old Faithful Geyser of Calistoga, CA. We present a physical model in which recharge during the period preceding an eruption is driven by pressure differences relative to the aquifer supplying the geyser. The model predicts that pressure and ground deformation are characterized by an exponential function of time, consistent with our observations. The geyser's conduit is connected to a reservoir at a depth of at least 42 m, and pressure changes in the reservoir can produce the observed ground deformations through either a poroelastic or elastic mechanical model.

8.2 Introduction

Geysers are features that episodically discharge water and steam. There are only about 10^3 such features on Earth, numbering far fewer than fumaroles and hot springs, features that continuously discharge steam and water, respectively. Geysers have attracted interest from geophysicists because of the improbability of circumstances necessary to achieve episodic discharge (*Ingebritsen and Rojstaczer*, 1996), their extreme sensitivity to the passage of seismic waves (e.g. *Husen et al.*, 2004; *Silver and Valette-Silver*, 1992), climatic forcing (*Hurwitz et al.*, 2008), and strains induced by solid earth tides (*Rinehart*, 1972) and for their potential as analogs to volcanic systems (*Kieffer*, 1984; *Kedar et al.*, 1996).

Despite significant interest, important aspects of the geyser process remain poorly understood. Eruptions involve decompression boiling of water initially close to the hydrostatic boiling curve, but opinions differ as to whether eruptions are triggered by a near-surface processes or by processes occurring deeper in the geyser system (*Steinberg and Merzhanov*, 1981; *Dowden et al.*, 1991). After erupting, a geyser's plumbing system fills with water which could come from a single source (*Ingebritsen and Rojstaczer*, 1993, 1996) or multiple reservoirs of hot and cold fluid (*Steinberg and Merzhanov*, 1981). The spatial and temporal evolution of pressure at depth during an eruption cycle depends on the processes that control recharge as well as the geometry and transport properties of the geyser's deep plumbing system. In turn, pressure changes at depth may produce observable ground deformations.

We present the results of a field campaign at Old Faithful Geyser of Calistoga, CA (Figure 8.1), subsequently referred to as Calistoga Geyser. During the field campaign, we measured ground deformation with a borehole tiltmeter. We present a physical model to interpret the observed ground deformation during the period preceding an eruption. Our model predicts that recharge and hence the interval between eruptions is controlled by hydraulic transmissivity in a zone around the base of the geyser conduit and that eruptions initiate from a shallow (near-vent) process. The insights gained from our model may be applicable to some natural geysers and highlight the potential gains in understanding that we can expect from future multi-instrument field studies of natural geysers.

Figure 8.1: (left) Aerial photo (USGS 6-inch orthophoto) showing geyser and instrument locations. (right) Picture of Calistoga Geyser erupting, looking to the SE.

8.3 Field Observations

Calistoga Geyser is an abandoned well, drilled in the late 1800s to an unknown depth, which at the time of our study erupted with a period of 4.6 minutes. Calistoga Geyser has been monitored previously, and its interval between eruptions is sometimes bimodal and appears to be affected by seasonality and by distant earthquakes (*Silver and Valette-Silver*, 1992). We carried out a multi-instrument geophysical study of Calistoga Geyser on May 6, 2010.

We measured ground deformation using a Pinnacle 5000 series borehole tiltmeter (1 nR resolution and 10 degree range) installed at a distance of 16.8 m from the geyser's vent (Figure 8.1). Figure 8.2 shows the radial tilt time series (filtered to remove diurnal and longer-preiod signals), as well as the stacked (Figure 8.2B) radial tilt record with standard deviations. Stacking was performed by identifying local minima in a smoothed tilt timeseries. The stack contains tilt records from 22 eruptions recorded between 19:14 and 22:13 (UTC) on May 6, 2010. The borehole tiltmeter was sampled once every 5 seconds.

We captured water flowing through a weir (the only outlet from the geyser's pool) and weighed the water using a portable scale during one eruption cycle to provide estimates of discharge. The discharge measured using this technique was nearly constant at $0.68 \pm .04$ l/s. Discharge was also estimated using Manning's equation, $V = R^{2/3}S^{1/2}/n$ where V is mean velocity in m/s, R is the hydraulic radius, and S is the channel slope, with $n = 0.02$, yielding discharge of 0.75 l/s. Based on the discharge estimates, the volume erupted is $1.9 - 2.1 \times 10^{-1}\mathrm{m}^3$.

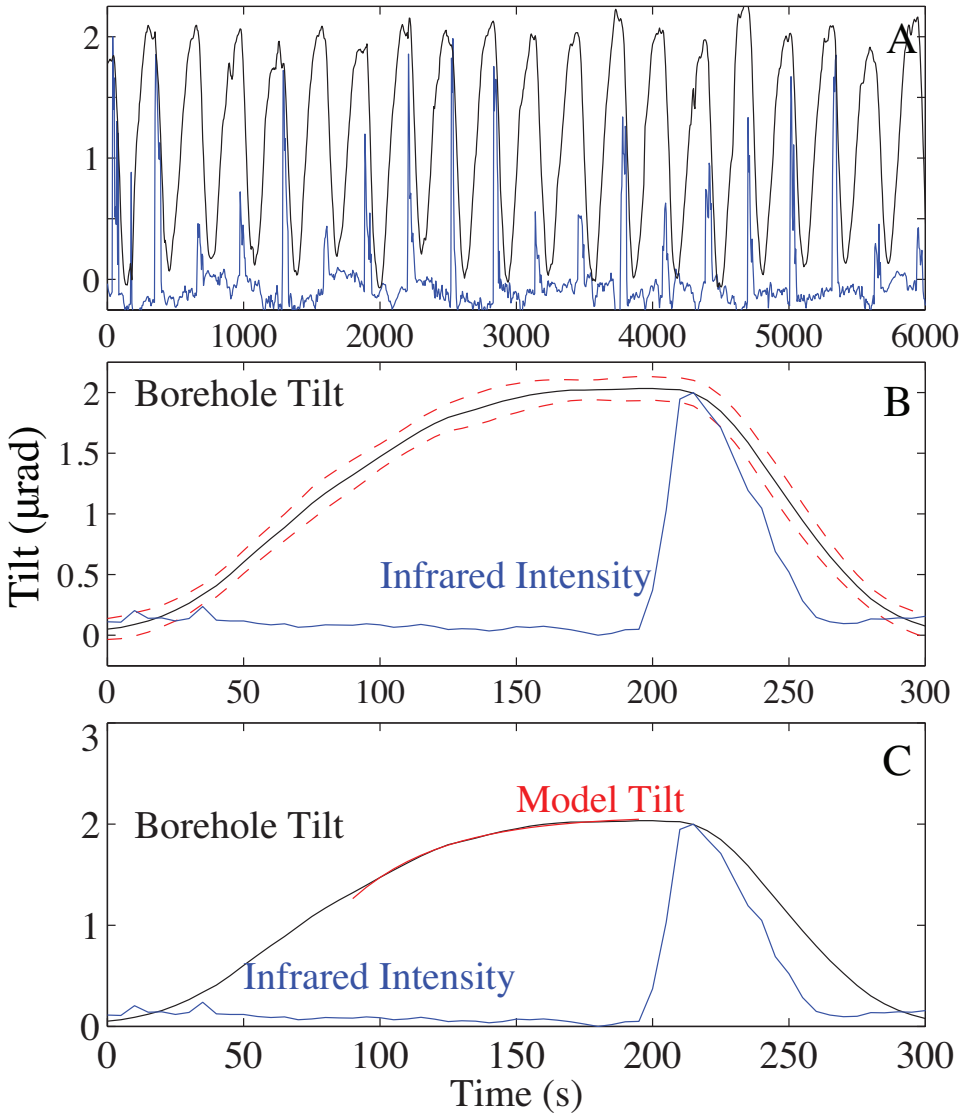

Figure 8.2: (A) Borehole tilt time series (black) and normalized single pixel infrared intensity (blue) for several eruptions beginning at 19:14:45 (UTC) on May 6, 2010. (B) Stacked borehole tilt record (black) and standard deviation (dashed red). Blue curve is stacked infrared intensity. (C) Same as (B) but showing model fit (red) to tilt data (black).

Eruption timing was measured using an (IR) sensor manufactured by ElectroOptical Systems connected to a simple Keplerian telescope (aperture 25.4 mm, f-ratio 1). The IR sensor operates at wavelengths of 7-18μ, with temporal sensitivity between DC and 10 Hz. The sensor's field of view (area 1.8 m^2) was positioned just above the geyser outlet. The IR sensor was sampled once every 5 seconds.

We filmed vent activity using an array of digital video cameras with 1080p resolution at 60 frames per second (fps) and with a FLIR A320 thermal imaging camera (320x240 pixels, 30 fps). Video recordings of vent activity were used for Particle Image Velocimetry (PIV) using the OpenPIV (www.openpiv.net) software package. The maximum exit velocity measured using PIV was 10-20 m/s, consistent with the sound speed in water-steam mixtures at 1 bar with 0.1-1% steam by mass (*Kieffer*, 1977), with corresponding specific enthalpy in the range 420-440 kJ/kg (*Wagner et al.*, 2000). The infrared video indicated that boiling temperatures are reached at the geyser vent during the initial, liquid-dominated, phase of the eruption.

8.4 Physical Model

We develop a physical model of the geyser motivated by the observational constraints, specifically 1) regular eruption interval, tilt pattern, and discharge and 2) decreasing rate of tilt leading up to eruption (Figure 8.2). We seek constraints on the size and location of the region in which pressure changes during an eruption cycle. Because we measured ground deformation at a single point, we assume homogenous, isotropic, and axisymmetric material properties and geometry.

We model the geyser conduit as a cylinder of radius r and length d (Figure 8.3A). We assume based on distant observations and photographs that the internal diameter of the conduit r is between 5 cm and 7.6 cm, though it may be somewhat narrower at depth owing to scale deposits. We assume that the conduit is connected at its base to a water-saturated porous medium. We use a pore pressure diffusion length scale $R = \sqrt{DT}$ to define a "reservoir" (Figure 8.3) where D is a hydraulic diffusivity and T is the interval between eruptions. The reservoir is the region in which pore pressure changes significantly during an eruption cycle. We assume that far from the geyser conduit, pore pressure P_∞ is uniform. Water flows into the reservoir at a rate given by:

$$Q(t) = \frac{2\pi k\delta}{\mu}\left[P_\infty - P(t)\right] \tag{8.1}$$

where k is an effective permeability, μ is fluid viscosity (assumed constant), δ is reservoir thickness, and P_∞ and $P(t)$ are far-field and reservoir pressures, respectively. We assume a single fluid phase in the reservoir and surroundings. We note that the far-field pressure is not known and may, in general, be in excess of hydrostatic. Equation 8.1 can be viewed as a zero-dimensional version of the groundwater flow equation. We have adopted a zero-dimensional model because we do not know how pressure changes as a function of space

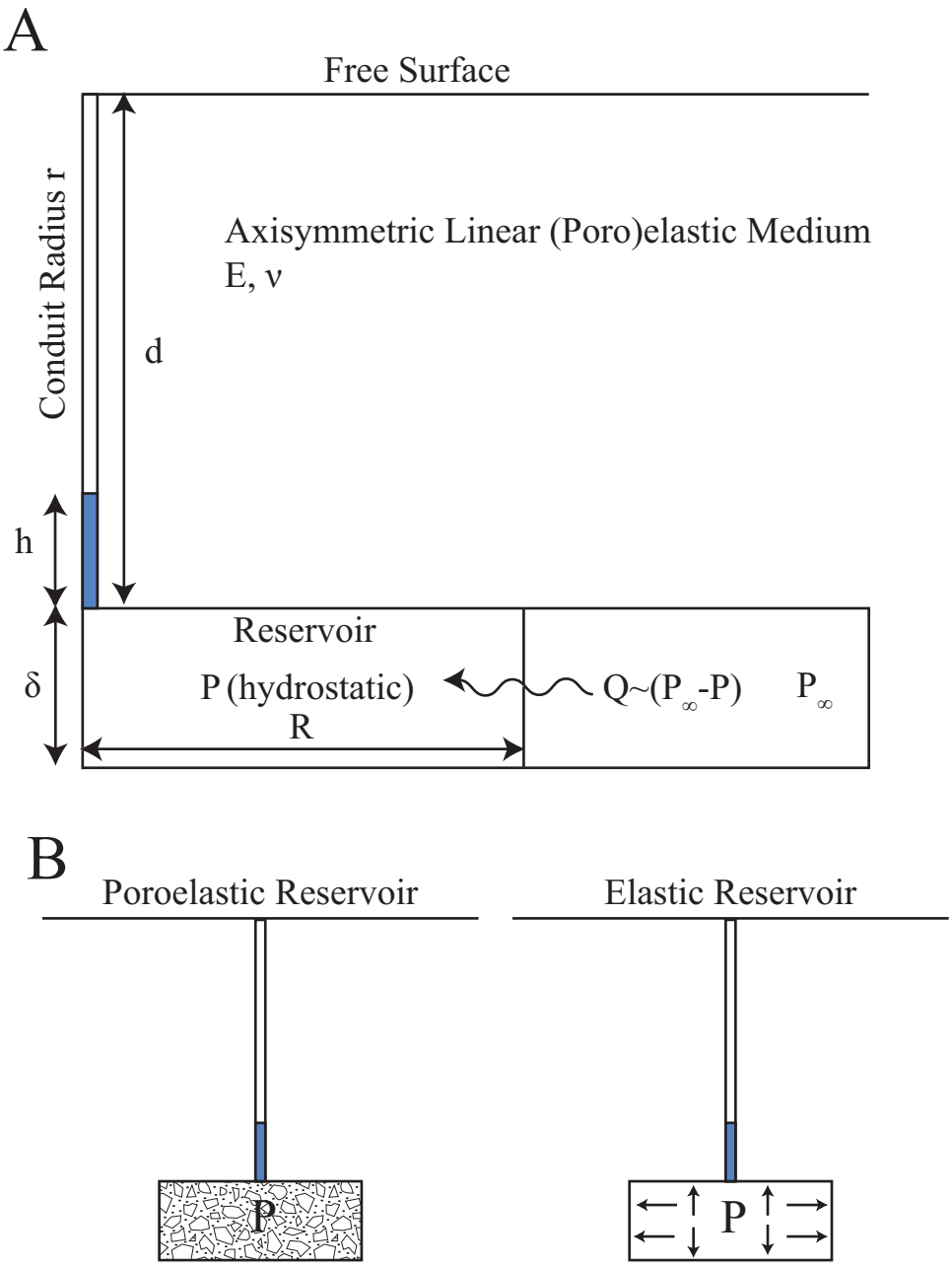

Figure 8.3: (A) Our conceptual model of Calistoga Geyser has three components: conduit, reservoir, and surroundings. The conduit fills during the interval between eruptions and the water at the base of the conduit is at the same pressure as the water in the reservoir. The far-field source of water constant pressure and temperature. The surroundings are treated as a linear elastic medium that deforms in response to pressure changes in the reservoir. (B) The reservoir is modeled as either part of a linear poroelastic medium (left) or as a cavity in an elastic medium (right).

and time during an eruption, a prerequisite to impose an initial condition when modeling the recharge phase. The pressure in the reservoir is assumed to be uniform and hydrostatic ($P(t) = \rho g h(t)$), where h is the conduit fill level (Figure 8.3A). The recharge rate into the reservoir Q is related to pressure P according to

$$dP/dt = \rho g Q/(\pi r^2), \tag{8.2}$$

where r is the conduit radius. We combine Equations 8.1-8.2 to obtain the temporal evolution of reservoir pressure

$$P(t) = (P_0 - P_\infty) \exp\left(-\frac{2k\rho g\delta}{\mu r^2} t\right) + P_\infty \tag{8.3}$$

where P_0 is the pressure in the reservoir at time $t = 0$. The form of Equation 8.3 is a common feature of geyser models in which recharge is driven by pressure differences (*Steinberg and Merzhanov*, 1981; *Kedar et al.*, 1998)

We model surface displacements resulting from pressure changes at depth using two models, chosen to be analogous to different conceptual models for geysers in which the reservoir is assumed to be either a cavity (e.g. *Steinberg and Merzhanov*, 1981) or a porous medium (e.g. *Ingebritsen and Rojstaczer*, 1993), as illustrated in Figure 8.3B. The first model considers the possibility that the reservoir and its surroundings behave as an homogenous isotropic linear poroelastic material. Pressure changes in the reservoir (Figure 8.3A) produce volumetric strains and deform the surroundings elastically. In the second model, we assume that there is a cavity at depth, conceptually similar to a magma chamber, and pressure changes within the cavity cause the elastic surroundings to deform.

The constitutive equation for the poroelastic model is

$$\sigma_{ij} = 2G\epsilon_{ij} + \frac{2G\nu}{1-2\nu}\epsilon_{ij}\delta ij - \alpha p \delta_{ij} \tag{8.4}$$

where G (measured in Pa) and ν (dimensionless) are the shear modulus and Poisson's ratio and α is the Biot coefficient. We solve the momentum equation $\nabla \cdot \underline{\sigma} = \underline{0}$ using an implementation of the finite element formulation described in *Zienkiewicz and Taylor* (2005, chapter 6). We used bilinear rectangular elements for both displacement and pressure on a non-uniformly spaced grid. We assume for the sake of simplicity that $\alpha = 1.0$, which is equivalent to assuming that the solid phase is incompressible (*Wang*, 2000). The domain has a free surface and we compute tilt (ψ) directly from the displacement field. We evaluate the computed tilt at the location x of the borehole tiltmeter and compare with the observed radial tilt. We note that in our model, tilt is linearly proportional to pressure change:

$$\psi(t) = k_\psi(\nu, \alpha, R, d, \delta, x)\frac{P(t)}{G} \tag{8.5}$$

where k_ψ is a coefficient relating changes in pressure to changes in tilt and R, d, δ are the effective reservoir radius, depth, and thickness. Values for the parameters are listed in

Table 8.1. Laboratory values of the shear modulus G for sedimentary and volcanic rocks are typically in the range $0.4 - 4 \times 10^{10}$ Pa and Poisson's ration ν is typically $0.2 - 0.25$ (*Turcotte and Schubert*, 2002). The effective value of the in-situ shear modulus may be at least an order of magnitude lower than the laboratory values (*Davis*, 1986). The modeled tilt is inversely proportional to the shear modulus G.

Parameter	Description	Value or Range Considered
r	Radius of geyser conduit	2.5-3.84 cm
d	Depth to reservoir	40-100 m
δ	Thickness of reservoir	0.5-10 m
R	Radius of reservoir	1-50 m
ρ	Fluid density	1000 kg/m^3
G	Shear modulus	4×10^9 Pa
α	Biot coefficient	1.0
ν	Poisson's ratio	0.25

Table 8.1: Summary of parameters entering the mathematical model

For the elastic model, we computed displacements using the axisymmetric program mode of FEAP v8.3 (*Taylor*, 2011). As for the poroelastic model, both displacement and tilt are linearly proportional to pressure change. The tilt-pressure coefficient k_ψ for the elastic case depends on the same variables as for the poroelastic case except for the absence of the Biot coefficient α.

Equation 8.3 predicts that tilt during the recharge phase is described by an exponential function of time. We fit an exponential curve to the stacked borehole radial tilt record (90-195 s in Figure 8.2). The length of the temporal window used for curve fitting was chosen by maximizing the coefficient of determination R^2 while varying the starting point of the window between 0 s (the time of minimum tilt) and 195 s (the time of eruption onset inferred from the IR sensor). The exponential fit of the form $\psi(t) = k_\psi \left[(P_0 - P_\infty) \exp(-K_1 t) + P_\infty\right]$ allows us to directly constrain only the exponential decay constant $K_1 = 2k\rho g\delta/(\mu r^2)$ (best-fit value $2.95 \pm 0.2 \times 10^{-2}$ s^{-1}).

8.5 Discussion

We can place some bounds on the range of permissible values of k_ψ and consequently on the range of the parameters R, d and δ that describe reservoir geometry. The removal of the volume erupted in a cycle (0.19 m^3) would lower the water level in the conduit by 42-97 m for the range of conduit radii considered. The corresponding pressure changes during an eruption cycle are 4.1×10^5-9.5×10^5 Pa. The range of tilt during an eruption cycle is 2.0 μrad, so the tilt coefficient k_ψ should have a value between 2.1×10^{-12} and 4.9×10^{-12} rad/Pa. We show isosurfaces for these values of the tilt pressure coefficient for both the poroelastic

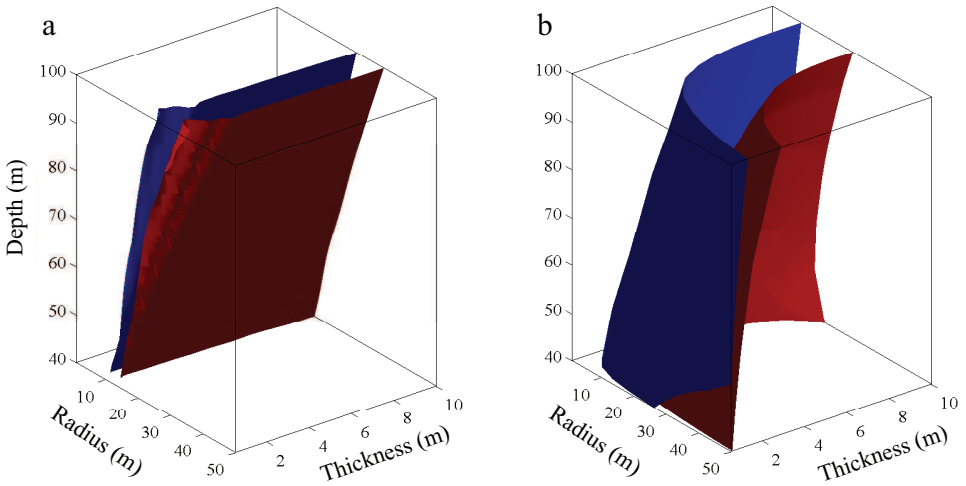

Figure 8.4: Isosurfaces of tilt coefficient k_ψ (Equation 8.5) calculated using (a) poroelastic and (b) elastic deformation source models (Section 8.4). Blue surface corresponds to $k_\psi = 2.1{\cdot}10^{-12}$ rad/Pa and red surface to $k_\psi = 1.4{\times}10^{-11}$ rad/Pa. k_ψ depends on tiltmeter position in addition to the quantities on the three axes shown, hence no axes can be eliminated through non-dimensionalization. The isosurfaces shown depend on E, ν, and α, with values given in Table 8.1

model and the elastic model in R, d, δ space in Figure 8.4. For any point lying between the blue and red isosurfaces in Figure 8.4, there exists a choice of the permeability k that will produce the observed tilt amplitude and exponential timescale. In other conceptual models of natural geysers, the component analogous to our reservoir is either a cavity (*Steinberg and Merzhanov*, 1981) or a porous medium (*Ingebritsen and Rojstaczer*, 1993). Because we can explain the observed tilt signal using either type of reservoir, we cannot distinguish between these two possibilities, but future studies using additional tiltmeters may allow us to distinguish between these two end-member options.

Despite the significant ambiguity in source location and transport properties, our model satisfies all of the available observational constraints. The surface deformations support a conceptual model for Calistoga geyser in which a vertical pipe is fed by recharge from a single hot liquid water reservoir at a rate that depends on the fill level in the pipe and the far-field pressure P_∞. Seasonal variations in groundwater recharge may lead to changes in P_∞, and hence affect the interval between eruptions (*Silver and Valette-Silver*, 1992). In the model of the geyser process proposed by *Steinberg and Merzhanov* (1981), water is drawn from the hot source at a constant rate irrespective of the geyser's chamber pressure whereas water is drawn from the cold reservoir at a rate proportional to the pressure difference between the cold water reservoir and the geyser chamber. If water flowed into Calistoga Geyser's reservoir and conduit at a constant rate irrespective of fill level h, we would expect h, P, and ψ to vary linearly in time during the recharge phase. We see no evidence for such behavior. Based

on the observed exit velocity and temperature, the fluid entering the base of the conduit has a specific enthalpy in excess of the boiling-curve enthalpy at atmospheric pressure. Hence, as the plumbing system is filled, the fluid in the upper portion of the conduit remains near the boiling curve and the removal of some overburden will lead to decompression boiling (*Kieffer*, 1989).

Acknowledgments

This paper emerged in part from ideas discussed and measurements performed by students in EPS 200 at UC Berkeley in collaboration with USGS Menlo Park. Jennifer Frederick helped make the discharge measurements. Ben Andrews operated the video cameras. Edwin Kite operated the FLIR camera. Zack Geballe and Ian Rose mapped the instrument locations. Fred Murphy and Doug Myren assisted with instrumentation and data loggers. This work could not have been carried out without the generosity and support of the owners of Old Faithful Geyser of Calistoga, CA. Shaul Hurwitz and Malcolm Johnston were supported by the USGS Volcano Hazards and Earthquake Hazards programs, respectively.

Chapter 9

Conclusion

In Chapters 2-3, we addressed questions pertaining to the thermal evolution of icy moons:

- How deep can downward-propagating fractures penetrate in planetary ice shells?
- Is it possible to detect active fracture formation using thermal emissions from fractures?
- Under what conditions does Crystallographic Preferred Orientation (CPO) develop in ice mantles?
- Does CPO affect heat transport or surface topography?
- Is CPO likely detectable by the proposed ESA JUICE spacecraft?

We found that fracture penetration depth is controlled to first order by a balance between hyrdostatic compression and tensile stresses, which are limited in magnitude by the tensile strength of ice. CPO development has a strong effect on the anisotropy of ice viscosity, and hence on heat transport within planetary ice shells. However, variations in grain size have a still larger influence on isotropic viscosity and hence exert the dominant control on heat transport by convection. Chapters 2 and 3 highlight the importance of understanding the physical and mechanical properties of planetary materials. Some useful constraints can be provided by laboratory experiments. For instance, recent ice fracture toughness experiments performed under Titan-like temperature conditions support high $O(10^6)$ Pa values of tensile strength and increasing strength with decreasing temperature (*Collins et al.*, 2012). Other advances in understanding can only come from improved constraints on the morphology of surface features, icy satellite internal structure, composition, and grain size, that can only be provided by new missions to the outer solar system.

In Chapters 4-5, we addressed several questions related to the mechanics of mud volcanoes, response of mud volcanoes to earthquakes, and remote sensing of mud volcano and geyser ground deformation:

- Why do mud volcanoes sometimes erupt in response to earthquakes?
- How does a large mud volcano like Lusi function?
- How long will Lusi continue to erupt?
- What can geyser ground deformation tell us about geyser source processes?

It is well known that mud volcanoes respond to earthquakes, though less is known about the mechanism or mechanisms by which responses occur. In Chapter 4, we showed that mobilizing bubbles trapped in mud (which has a yield strength) is unlikely to have been responsible for the triggering of the Davis-Schrimpf mud volcanoes during the El Mayor-Cucapah earthquake. We favor instead frequency-dependent mechanisms that enhance permeability, such as removal of bubbles trapped in pore throats. New observations of ground deformation near Lusi indicate that the rate of deformation is currently decreasing exponentially in time,

which is the expected behavior when material erupts from a reservoir of fixed size in an elastic medium at a rate set by overpressure. However, before pressure began decreasing exponentially in time, the evolution of radius and pressure indicate that the boundaries of the mud source region expanded in time. This expansion could have been due to progressive mobilization of mud that was initially solid prior to the initiation of the eruption. If the present exponentially decreasing trend continues, Lusi's discharge will fall below $10^3 m^3$/day by 2018.

Bibliography

Adler, P. M., and H. Brenner (1988), Multiphase Flow in Porous Media, *Annual Review of Fluid Mechanics*, *20*(1), 35–59.

Amestoy, P. R., I. S. Duff, J.-Y. L'Excellent, and J. Koster (2001), A Fully Asynchronous Multifrontal Solver Using Distributed Dynamic Scheduling, *SIAM J. Matrix Anal. Appl.*, *23*(1), 15–41.

Amestoy, P. R., A. Guermouche, J.-Y. L'Excellent, and S. Pralet (2006), Hybrid scheduling for the parallel solution of linear systems, *Parallel Comput.*, *32*(2), 136–156.

Anderson, J., and P. Bodin (1987), Earthquake recurrence models and historical seismicity in the Mexicali-Imperial Valley, *Bulletin of the Seismological Society of America*, *77*(2), 562–578.

Balay, S., J. Brown, K. Buschelman, V. Eijkhout, W. D. Gropp, D. Kaushik, M. G. Knepley, L. C. McInnes, B. F. Smith, and H. Zhang (2012), PETSc Users Manual, *Tech. Rep. ANL-95/11 - Revision 3.3*.

Balderman, M., C. Johnson, D. Miller, and D. Schmidt (1978), The 1852 Fort Yuma earthquake, *Bulletin of the Seismological Society of America*, *68*(3), 699–710.

Barr, A. C., and W. B. McKinnon (2007), Convection in Enceladus' ice shell: Conditions for initiation, *Geophysical Research Letters*, *34*(9), 09,202.

Barr, A. C., and D. E. Stillman (2011), Strain history of ice shells of the Galilean satellites from radar detection of crystal orientation fabric, *Geophys. Res. Lett*, *38*(6), 06,203.

Barr, A. C., R. T. Pappalardo, and S. Zhong (2004), Convective instability in ice I with non-Newtonian rheology: Application to the icy Galilean satellites, *J. Geophys. Res.*, *109*(E12), E12,008.

Bayuaji, L., H. Watanabe, H. Tonooka, J. Tetuko Sri Sumantyo, and H. Kuze (2010), STUDY ON LAND SURFACE TEMPERATURE CHARACTERISTICS OF HOT MUD ERUPTION IN EAST JAVA, INDONESIA, *International Journal of Remote Sensing and Earth Sciences (IJReSES)*, *6*(1).

Bayuni, E. M. (2009), 'Lusi' spurs geologists interest, *The Jakarta Post*.

Beal, C. (1915), The Earthquake in the Imperial Valley, California, June 22,1915, *Bulletin of the Seismological Society of America*, *5*(3), 130–149.

Beckham, R. E., A. I. Abdel-Fattah, P. M. Roberts, R. Ibrahim, and S. Tarimala (2012), Mobilization of Colloidal Particles by Low-Frequency Dynamic Stress Stimulation, *Langmuir*, *26*(1), 19–27.

Běhounková, M., G. Tobie, G. Choblet, and O. Čadek (2010), Coupling mantle convection and tidal dissipation: Applications to Enceladus and Earth-like planets, *J. Geophys. Res.*, *115*(E14), 09,011.

Berardino, P., G. Fornaro, R. Lanari, and E. Sansosti (2002), A new algorithm for surface deformation monitoring based on small baseline differential SAR interferograms, *IEEE Transactions on Geoscience and Remote Sensing*, *40*(11), 2375–2383.

Beresnev, I. (2006), Theory of vibratory mobilization on nonwetting fluids entrapped in pore constrictions, *Geophysics*, *71*(6), N47–N56.

Beresnev, I., W. Gaul, and R. D. Vigil (2011), Direct pore-level observation of permeability increase in two-phase flow by shaking, *Geophys. Res. Lett*, *38*(20), L20,302–.

Bertani, R. (2005), World geothermal power generation in the period 2001-2005, *Geothermics*, *34*(6), 651–690.

Bierhaus, E. B., K. Zahnle, and C. R. Chapman (2009), Europa's Crater Distributions and Surface Ages, in *Europa*, edited by K. Khurana, R. T. Pappalardo, and W. B. McKinnon, p. 161, University of Arizona Press.

Billings, S. E., and S. A. Kattenhorn (2005), The great thickness debate: Ice shell thickness models for Europa and comparisons with estimates based on flexure at ridges, *Icarus*, *177*, 397–412.

Bjerhammar, A. (1973), *Bjerhammar (1973) Theory of errors and generalized matrix inverses*, Elsevier, Amsterdam.

Blankenbach, B., F. Busse, U. Christensen, L. Cserepes, D. Gunkel, U. Hansen, H. Harder, G. Jarvis, M. Koch, G. Marquart, D. Moore, P. Olson, H. Schmeling, and T. Schnaubelt (1989), A benchmark comparison for mantle convection codes, *Geophysical Journal International*, *98*(1), 23–38.

Blower, J. B. (2001), Factors controlling permeability-porosity relationships in magma, *Bulletin of Volcanology*, *63*(7), 497–504.

Bonini, M. (2009a), Mud volcano eruptions and earthquakes in the Northern Apennines and Sicily, Italy, *Tectonophysics*, *474*(3-4), 723–735.

Bonini, M. (2009b), Structural controls on a carbon dioxide-driven mud volcano field in the Northern Apennines (Pieve Santo Stefano, Italy): Relations with pre-existing steep discontinuities and seismicity, *Journal of Structural Geology*, *31*(1), 44–54.

Brodsky, E., E. Roeloffs, D. Woodcock, I. Gall, and M. Manga (2003), A mechanism for sustained groundwater pressure changes induced by distant earthquakes, *Journal of Geophysical Research*, *108*(B8), 2390.

Brodsky, E. E., and S. G. Prejean (2005), New constraints on mechanisms of remotely triggered seismicity at Long Valley Caldera, *Journal of Geophysical Research*, *110*, B04,302.

Bunge, H. J. (1982), *Texture Analysis in Materials Science*, Butterworth, London.

Cammarano, F., V. Lekic, M. Manga, M. Panning, and B. Romanowicz (2006), Long-period seismology on Europa: 1. Physically consistent interior models, *Journal of Geophysical Research (Planets)*, *111*, E12,009.

Castelnau, O., P. Duval, R. A. Lebensohn, and G. R. Canova (1996), Viscoplastic modeling of texture development in polycrystalline ice with a self-consistent approach: Comparison with bound estimates, *Journal of Geophysical Research*, *101*, 13,851.

Castelnau, O., G. Canova, R. Lebensohn, and P. Duval (1997), Modelling viscoplastic behavior of anisotropic polycrystalline ice with a self-Consistent approach, *Acta Materialia*, *45*(11), 4823–4834.

Castelnau, O., D. Blackman, and T. Becker (2009), Numerical simulations of texture development and associated rheological anisotropy in regions of complex mantle flow, *Geophys. Res. Lett*, *36*(12), L12,304.

Chadwick, P. (1999), *Continuum Mechanics: Concise Theory and Problems*, 2 ed., Dover, Mineola, NY.

Chen, C. W., and H. A. Zebker (2001), Two-dimensional phase unwrapping with use of statistical models for cost functions in nonlinear optimization, *Journal of the Optical Society of America A: Optics*, *18*(2), 338–351.

Chigira, M., and K. Tanaka (1997), Structural features and the history of mud volcanoes in Southern Hokkaido, Northern Japan, *Journal of the Geological Society of Japan*, *103*(8), 781–791.

Chyba, C., and C. Phillips (2001), Possible ecosystems and the search for life on Europa., *Proc Natl Acad Sci U S A*, *98*(3), 801–804.

Cichon, M. (2012), 49.9-MW Hudson Ranch I Geothermal Plant Unveiled in California, *http://www renewableenergyworldcom/rea/news/article/2012/05/49-9- mw-hudson-ranch-i-geothermal-plant-unveiled-in-calif.*

Clark, K., T. Magner, R. Pappalardo, M. Blanc, R. Greeley, J.-P. Lebretron, C. Jones, and J. Sommerer (2009), Jupiter Europa Orbiter Mission Study 2008: Final Report, *Tech. rep.*, NASA.

Clift, R., J. Grace, and M. Weber (1978), *Bubbles, Drops, and Particles*, Academic Press.

Collins, G. C., L. S. Sklar, K. L. Litwin, and P. J. Polito (2012), Do Titan's river channels carve into ice bedrock or loose regolith?, in *Titan Through Time; Unlocking Titan's Past, Present and Future*, p. 30.

Consolmagno, G. J., and J. S. Lewis (1978), The Evolution of Icy Satellite Interiors and Surfaces, *Icarus*, *34*, 280–293.

Costantini, M., and P. A. Rosen (1999), A generalized phase unwrapping approach for sparse data, in *Proceedings IEEE 1999 International Geoscience and Remote Sensing Symposium*, pp. 267–269, IEEE.

Coussot, P., and J. M. Piau (1994), On the behavior of fine mud suspensions, *Rheologica Acta*, *33*(3), 175–184.

Crawford, G. D., and D. J. Stevenson (1988), Gas-driven water volcanism in the resurfacing of Europa, *Icarus*, *73*, 66–79.

Crouch, S., and A. Starfield (1983), *Boundary Element Methods in Solid Mechanics*, London.

Cuffey, K., and W. Paterson (2010), *The Physics of Glaciers*, 4 ed., Butterworth Heinemann, Burlington.

Davies, R., R. Swarbrick, and R. Evans (2007), Birth of a mud volcano: East Java, 29 May 2006, *GSA Today*, *17*(2), 4–9.

Davies, R. J., M. Brumm, M. Manga, R. Rubiandini, R. Swarbrick, and M. Tingay (2008), The East Java mud volcano (2006 to present): An earthquake or drilling trigger?, *Earth and Planetary Science Letters*, *272*(3), 627–638.

Davies, R. J., S. Mathias, R. E. Swarbrick, and M. Tingay (2011), Probabilistic longevity estimate for the LUSI mud volcano, East Java, *Journal of the Geological Society*, *168*(2), 517–523.

Davis, P. M. (1986), Surface Deformation Due to Inflation of an Arbitrarily Oriented Triaxial Ellipsoidal Cavity in an Elastic Half-Space, With Reference to Kilauea Volcano, Hawaii, *J. Geophys. Res.*, *91*(B7), 7429–7438.

Dempsey, J. P., R. M. Adamson, and S. V. Mulmule (1999), Scale effects on the in-situ tensile strength and fracture of ice. Part II: First-year sea ice at Resolute, N.W.T., *International Journal of Fracture*, *95*(1), 347–366.

Dobran, F. (2001), *Volcanic processes: mechanisms in material transport*, Kluwer Academic, New York.

Dowden, J., P. Kapadia, G. Brown, and H. Rymer (1991), Dynamics of a geyser eruption, *Journal of Geophysical Research*, *96*(B), 18,059–18,071.

Dubash, N., and I. Frigaard (2004), Conditions for static bubbles in viscoplastic fluids, *Physics of Fluids*, *16*, 4319–4330.

Dubash, N., and I. Frigaard (2007), Propagation and stopping of air bubbles in Carbopol solutions, *Journal of Non-Newtonian Fluid Mechanics*, *142*(1-3), 123–134.

Dziewonski, A., T.-A. Chou, and J. Woodhouse (1981), Determination of Earthquake Source Parameters From Waveform Data for Studies of Global and Regional Seismicity, *Journal of Geophysical Research*, *86*(B4), 2825–2852.

Elders, W., and J. Sass (1988), The Salton Sea Scientific Drilling Project, *Journal of Geophysical Research*, *93*(B11), 12,953–12,968.

Elkhoury, J., E. Brodsky, and D. Agnew (2006), Seismic waves increase permeability, *Nature*, *441*(7097), 1135–1138.

Elkhoury, J., A. Niemeijer, E. Brodsky, and C. Marone (2011), Laboratory observations of permeability enhancement by fluid pressure oscillation of in situ fractured rock, *Journal of Geophysical Research*, *116*, B02,311.

Eluszkiewicz, J. (2004), Dim prospects for radar detection of Europa's ocean, *Icarus*, *170*(1), 234–236.

Evans, R. J., S. A. Stewart, and R. J. Davies (2008), The structure and formation of mud volcano summit calderas, *Journal of the Geological Society*, *165*(4), 769–780.

Fagents, S. A. (2003), Considerations for effusive cryovolcanism on Europa: The post-Galileo perspective, *J. Geophys. Res.*, *108*(E12), 5139.

Fagents, S. A., R. Greeley, R. J. Sullivan, R. T. Pappalardo, L. M. Prockter, and T. G. S. Team (2000), Cryomagmatic Mechanisms for the Formation of Rhadamanthys Linea, Triple Band Margins, and Other Low-Albedo Features on Europa, *Icarus*, *144*(1), 54–88.

Ferretti, A., C. Prati, and F. Rocca (2001), Permanent scatterers in SAR interferometry, *Geoscience and Remote Sensing, IEEE Transactions on*, *39*(1), 8–20.

Franceschetti, G. (1999), *Synthetic aperture radar processing*, CRC Press, Boca Raton.

Freeman, J., L. Moresi, and D. A. May (2006), Thermal convection with a water ice I rheology: Implications for icy satellite evolution, *Icarus*, *180*(1), 251–264.

Fukushima, Y., J. Mori, M. Hashimoto, and Y. Kano (2009), Subsidence associated with the LUSI mud eruption, East Java, investigated by SAR interferometry, *Marine and Petroleum Geology*, *26*(9), 1740–1750.

Gerya, T., and D. Yuen (2003), Characteristics-based marker-in-cell method with conservative finite-differences schemes for modeling geological flows with strongly variable transport properties, *Physics of the Earth and Planetary Interiors*, *140*(4), 293–318.

Goldsby, D. L., and D. L. Kohlstedt (2001), Superplastic deformation of ice: Experimental observations, *J. Geophys. Res.*, *106*(B6), 11,017–11,030.

Green, R. A., and J. K. Mitchell (2004), Energy-based evaluation and remediation of liquefiable soils, in *Geotechnical Engineering for Transportation Projects*, edited by M. Yegian and E. Kavazanjian, pp. 1961–1970, Am. Soc. Civ. Eng., Reston, VA.

Grundy, W. M., M. W. Buie, J. A. Stansberry, J. R. Spencer, and B. Schmitt (1999), Near-Infrared Spectra of Icy Outer Solar System Surfaces: Remote Determination of H2O Ice Temperatures, *Icarus*, *142*, 536–549.

Guilhem, A., Z. Peng, and R. M. Nadeau (2010), High-frequency identification of non-volcanic tremor triggered by regional earthquakes, *Geophysical Research Letters*, *37*(1), 16,309.

Han, L., and A. P. Showman (2005), Thermo-compositional convection in Europa's icy shell with salinity, *Geophysical Research Letters*, *32*(2), 20,201.

Han, L., and A. P. Showman (2008), Implications of shear heating and fracture zones for ridge formation on Europa, *Geophysical Research Letters*, *35*, 3202.

Han, L., and A. P. Showman (2010), Coupled convection and tidal dissipation in Europa's ice shell, *Icarus*, *207*(2), 834–844.

Hansen, C. J., L. Esposito, A. I. F. Stewart, J. Colwell, A. Hendrix, W. Pryor, D. Shemansky, and R. West (2006), Enceladus' Water Vapor Plume, *Science*, *311*, 1422–1425.

Helgeson, H. C. (1968), Geologic and thermodynamic characteristics of the Salton Sea geothermal system, *American Journal of Science*, *266*(3), 129–166.

Hill, D. P., P. A. Reasenberg, A. Michael, W. J. Arabaz, G. Beroza, D. Brumbaugh, J. N. Brune, R. Castro, S. Davis, D. dePolo, W. L. Ellsworth, J. Gomberg, S. Harmsen, L. House, S. M. Jackson, M. J. S. Johnston, L. Jones, R. Keller, S. Malone, L. Munguia, S. Nava, J. C. Pechmann, A. Sanford, R. W. Simpson, R. B. Smith, M. Stark, M. Stickney, A. Vidal, S. Walter, V. Wong, and J. Zollweg (1993), Seismicity Remotely Triggered by the Magnitude 7.3 Landers, California, Earthquake, *Science*, *260*(5114), 1617–1623.

Hollander, M., and D. Wolfe (1999), *Nonparametric statistical methods*.

Holzer, T. L., and T. L. Youd (2007), Liquefaction, Ground Oscillation, and Soil Deformation at the Wildlife Array, California, *Bulletin of the Seismological Society of America*, *97*(3), 961–976.

Holzer, T. L., T. C. Hanks, and T. L. Youd (1989), Dynamics of Liquefaction During the 1987 Superstition Hills, California, Earthquake, *Science*, *244*(4900), 56–59.

Hsieh, D.-Y. (1961), Theory of Rectified Diffusion of Mass into Gas Bubbles, *Acoustical Society of America Journal*, *33*, 206.

Hudnut, K., E. Hauksson, D. Given, A. Guarino, S. Hough, K. Hutton, L. Jones, K. Felzer, and B. Dollar (2010), Mw 7.2 El Mayor-Cucapah Earthquake, *Tech. rep.*, CISN/SCSN.

Hurford, T. A., P. Helfenstein, G. V. Hoppa, R. Greenberg, and B. G. Bills (2007a), Eruptions arising from tidally controlled periodic openings of rifts on Enceladus, *Nature*, *447*, 292–294.

Hurford, T. A., A. R. Sarid, and R. Greenberg (2007b), Cycloidal cracks on Europa: Improved modeling and non-synchronous rotation implications, *Icarus*, *186*, 218–233.

Hurwitz, S., L. Christiansen, and P. Hsieh (2007), Hydrothermal fluid flow and deformation in large calderas: Inferences from numerical simulations, *Journal of Geohysical Research*, *112*, B02,206.

Hurwitz, S., A. Kumar, R. Taylor, and H. Heasler (2008), Climate-induced variations of geyser periodicity in Yellowstone National Park, USA, *Geology*, *36*(6), 451.

Husen, S., R. Taylor, R. Smith, and H. Healser (2004), Changes in geyser eruption behavior and remotely triggered seismicity in Yellowstone National Park produced by the 2002 M 7.9 Denali fault earthquake, Alaska, *Geology*, *32*(6), 537–540.

Hussmann, H., T. Spohn, and K. Wieczerkowski (2002), Thermal Equilibrium States of Europa's Ice Shell: Implications for Internal Ocean Thickness and Surface Heat Flow, *Icarus*, *156*(1), 143–151.

Ichihara, M., and E. E. Brodsky (2006), A limit on the effect of rectified diffusion in volcanic systems, *Geophysical Research Letters*, *33*(2), L02,316.

Ingebritsen, S. E., and S. A. Rojstaczer (1993), Controls on Geyser Periodicity, *Science*, *262*(5135), 889–892.

Ingebritsen, S. E., and S. A. Rojstaczer (1996), Geyser periodicity and the response of geysers to deformation, *Journal of Geophysical Research*, *101*(B), 21,891–21,906.

Irwin, G. (1957), Analysis of stresses and strains near the end of a crack traversing a plate, *Journal of Applied Mechanics*, *24*(4), 361–364.

Istadi, B., G. Pramono, and P. Sumintadireja (2009), Modeling study of growth and potential geohazard for LUSI mud volcano: East Java, Indonesia, *Marine and Petroleum Geology*, *26*, 1724–1739.

Karlstrom, L., M. L. Rudolph, and M. Manga (2012), Caldera size modulated by the yield stress within a crystal-rich magma reservoir, *Nature Geoscience*, *5*(6), 402–405.

Kedar, S., B. Sturtevant, and H. Kanamori (1996), The origin of harmonic tremor at Old Faithful geyser, *Nature*.

Kedar, S., H. Kanamori, and B. Sturtevant (1998), Bubble collapse as the source of tremor at Old Faithful Geyser, *Journal of Geophysical Research*, *103*(B), 24,283–24,300.

Keeper, D. K. (1984), Landslides caused by earthquakes, *Geological Society of America Bulletin*, *95*(4), 406–421.

Kelley, V. C., and J. L. Soske (1936), Origin of the Salton Volcanic Domes, Salton Sea, California, *The Journal of Geology*, *44*(4), 496–509.

Kieffer, S. W. (1977), Sound speed in liquid-gas mixtures: water-air and water-steam, *J. Geophys. Res.*, *82*(20), 2895–2904.

Kieffer, S. W. (1984), Seismicity at Old Faithful Geyser: an isolated source of geothermal noise and possible analogue of volcanic seismicity, *Journal of Volcanology and Geothermal Research*, *22*(1-2), 59–95.

Kieffer, S. W. (1989), Geologic nozzles, *Rev. Geophys.*, *27*(1), 3–38.

Kieffer, S. W., and B. M. Jakosky (2008), PLANETARY SCIENCE: Enceladus–Oasis or Ice Ball?, *Science*, *320*(5882), 1432–1433.

King, N., L. Blair, K. Hudnut, and H. Stenner (2010), Report of USGS Activities El Mayor-Cucapah Earthquake of Sunday, April 4, 2010, *Tech. rep.*, USGS.

Kopf, A., S. Stegmann, G. Delisle, B. Panahi, C. S. Aliyev, and I. Guliyev (2009), In situ cone penetration tests at the active Dashgil mud volcano, Azerbaijan: Evidence for excess fluid pressure, updoming, and possible future violent eruption, *Marine and Petroleum Geology*, *26*(9), 1716–1723.

Kopf, A. J. (2002), Significance of mud volcanism, *Rev. Geophys.*, *40*(2).

Kopf, A. J. (2008), Volcanoes: Making calderas from mud, *Nature Geosci*, *1*(8), 500–501.

Kuskov, O. L., and V. A. Kronrod (2005), Internal structure of Europa and Callisto, *Icarus*, *177*(2), 550–569.

Lachenbruch, A. (1961), Depth and Spacing of Tension Cracks, *Journal of Geophysical Research*, *66*(12), 4273–4292.

Lebensohn, R., and C. Tome (1993), A self-consistent anisotropic approach for the simulation of plastic deformation and texture development of polycrystals: Application to zirconium alloys, *Acta Metallurgica et Materialia*, *41*(9), 2611–2624.

Lee, K. L., and H. B. Seed (1967), Cyclic stress conditions causing liquefaction of sand, *Journal of Soil Mechanics & Foundations Div*, *93*(SM1), 47–70.

Lee, S., R. T. Pappalardo, and N. C. Makris (2005), Mechanics of tidally driven fractures in Europa's ice shell, *Icarus*, *177*, 367–379.

Lee, S., R. T. Pappalardo, and N. C. Makris (2007), Reply to "Comment on 'Mechanics of tidally driven fractures in Europa's ice shell'", *Icarus*, *189*(2), 598–599.

Leith, A. C., and W. B. McKinnon (1996), Is There Evidence for Polar Wander on Europa?, *Icarus*, *120*, 387–398.

Leng, W., and S. Zhong (2011), Implementation and application of adaptive mesh refinement for thermochemical mantle convection studies, *Geochemistry, Geophysics, Geosystems*, *12*(4), Q04,006.

Lin, J., and R. Stein (2004), Stress triggering in thrust and subduction earthquakes, and stress interaction between the southern San Andreas and nearby thrust and strike-slip faults, *Journal of Geophysical Research*, *109*(B02303).

Liu, W., and M. Manga (2009), Changes in permeability caused by dynamic stresses in fractured sandstone, *Geophysical Research Letters*, *36*(L20307).

Lu, X., and S. W. Kieffer (2009), Thermodynamics and Mass Transport in Multicomponent, Multiphase H2O Systems of Planetary Interest, *Annu. Rev. Earth Planet. Sci.*, *37*(1), 449–477.

Lynch, D. K., and K. W. Hudnut (2008), The Wister Mud Pot Lineament: Southeastward Extension or Abandoned Strand of the San Andreas Fault?, *Bulletin of the Seismological Society of America*, *98*(4), 1720–1729.

Manga, M. (2007), Did an earthquake trigger the May 2006 eruption of the Lusi Mud volcano?, *Eos, Transactions American Geophysical Union*, *88*(18), 201.

Manga, M., and E. Brodsky (2006), Seismic Triggering of Eruptions in the Far Field: Volcanoes and Geysers, *Annual Review of Earth and Planetary Sciences*, *34*, 263–291.

Manga, M., and H. Stone (1994), Interactions between bubbles in magmas and lavas: effects of bubble deformation, *Journal of Volcanology and Geothermal Research*, *63*(3-4), 267–279.

Manga, M., and H. Stone (1995), Collective hydrodynamics of deformable drops and bubbles in dilute low Reynolds number suspensions, *Journal of Fluid Mechanics*, *300*, 231–263.

Manga, M., and C.-Y. Wang (2007), Pressurized oceans and the eruption of liquid water on Europa and Enceladus, *Geophysical Research Letters*, *34*, L07,202.

Manga, M., M. Brumm, and M. L. Rudolph (2009), Earthquake triggering of mud volcanoes, *Marine and Petroleum Geology*, *26*(9), 1785–1798.

Manga, M., I. Beresnev, E. E. Brodsky, J. E. Elkhoury, D. Elsworth, S. E. Ingebritsen, D. C. Mays, and C.-Y. Wang (2012), Changes in permeability caused by transient stresses: Field observations, experiments, and mechanisms, *Reviews of Geophysics*, *50*(2), 2004.

Mangeney, A., F. Califano, and O. Castelnau (1996), Isothermal flow of an anisotropic ice sheet in the vicinity of an ice divide, *J. Geophys. Res.*, *101*(B12), 28,189–28,204.

Marr, J. G., A. Elverhøi, C. Harbitz, J. Imran, and P. Harff (2002), Numerical simulation of mud-rich subaqueous debris flows on the glacially active margins of the Svalbard-Barents Sea, *Marine Geology*, *188*(3-4), 351–364.

Mastin, L. (2002), Insights into volcanic conduit flow from an open-source numerical model, *Geochem. Geophys. Geosyst.*

Mau, S., G. Rehder, I. G. Arroyo, J. Gossler, and E. Suess (2007), Indications of a link between seismotectonics and CH$_4$ release from seeps off Costa Rica, *Geochemistry, Geophysics, Geosystems*, *8*, 4003.

Mazzini, A., H. Svensen, G. Akhmanov, G. Aloisi, S. Planke, A. Malthe-Sørenssen, and B. Istadi (2007), Triggering and dynamic evolution of Lusi mud volcano, Indonesia, *Earth and Planetary Science Letters*, *261*, 375–388.

Mazzini, A., A. Nermoen, M. Krotkiewski, Y. Podladchikov, S. Planke, and H. Svensen (2009), Strike-slip faulting as a trigger mechanism for overpressure release through piercement structures. Implications for the Lusi mud volcano, Indonesia, *Marine and Petroleum Geology*, *26*(9), 1751–1765.

Mazzini, A., H. Svensen, G. Etiope, N. Onderdonk, and D. Banks (2011), Fluid origin, gas fluxes and plumbing system in the sediment-hosted Salton Sea Geothermal System (California, USA), *Journal of Volcanology and Geothermal Research*.

Mazzini, A., G. Etiope, and H. Svensen (2012), A new hydrothermal scenario for the 2006 Lusi eruption, Indonesia. Insights from gas geochemistry, *Earth and Planetary Science Letters*, *317–318*(0), 305–318.

McKinnon, W. B. (1999), Convective instability in Europa's floating ice shell, *Geophysical Research Letters*, *26*(7), 951–954.

Mellors, R., D. Kilb, A. Aliyev, A. Gasanov, and G. Yetirmishli (2007), Correlations between earthquakes and large mud volcano eruptions, *J. Geophys. Res.*, *112*(B4), B04,304.

Mitri, G., and A. P. Showman (2005), Convective-conductive transitions and sensitivity of a convecting ice shell to perturbations in heat flux and tidal-heating rate: Implications for Europa, *Icarus*, *177*(2), 447–460.

Mitri, G., and A. P. Showman (2008), A model for the temperature-dependence of tidal dissipation in convective plumes on icy satellites: Implications for Europa and Enceladus, *Icarus*, *195*(2), 758–764.

Miyamoto, H., G. Mitri, A. P. Showman, and J. M. Dohm (2005), Putative ice flows on Europa: Geometric patterns and relation to topography collectively constrain material properties and effusion rates, *Icarus*, *177*, 413–424.

Moore, W. B. (2006), Thermal equilibrium in Europa's ice shell, *Icarus*, *180*(1), 141–146.

Muffler, L., and D. White (1969), Active Metamorphism of Upper Cenozoic Sediments in the Salton Sea Geothermal Field and the Salton Trough, Southeastern California, *Geological Society of America Bulletin*, *80*(157-182).

Muir-Wood, R., and G. C. P. King (1993), Hydrological Signatures of Earthquake Strain, *J. Geophys. Res.*, *98*(B12), 22,035–22,068.

Nieva, D., and R. M. Barragán (2003), HCO-TERNARY: a FORTRAN code for calculating P-V-T-X properties and liquid vapor equilibria of fluids in the system H 2 O-CO 2 -CH 4 , *Computers & geosciences*, *29*(4), 469–485.

Nimmo, F. (2002), Strike-slip motion and double ridge formation on Europa, *J. Geophys. Res.*, *107*(E4), 5021.

Nimmo, F. (2004), Stresses generated in cooling viscoelastic ice shells: Application to Europa, *Journal of Geophysical Research (Planets)*, *109*, E12,001.

Nimmo, F., and M. Manga (2002), Causes, characteristics and consequences of convective diapirism on Europa, *Geophysical Research Letters*, *29*(23), 2109.

Nimmo, F., and R. T. Pappalardo (2006), Diapir-induced reorientation of Saturn's moon Enceladus, *Nature*, *441*, 614–616.

Nimmo, F., J. R. Spencer, R. T. Pappalardo, and M. E. Mullen (2007), Shear heating as the origin of the plumes and heat flux on Enceladus, *Nature*, *447*(7142), 289–291.

Obzhirov, A., R. Shakirov, A. Salyuk, E. Suess, N. Biebow, and A. Salomatin (2004), Relations between methane venting, geological structure and seismo-tectonics in the Okhotsk Sea, *Geo-Marine Letters*, *24*(3), 135–139.

Ojakangas, G. W., and D. J. Stevenson (1989a), Polar wander of an ice shell on Europa, *Icarus*, *81*, 242–270.

Ojakangas, G. W., and D. J. Stevenson (1989b), Thermal state of an ice shell on Europa, *Icarus*, *81*, 220–241.

Onderdonk, N., A. Mazzini, L. Shafer, and H. Svensen (2011), Controls on the geomorphic expression and evolution of gryphons, pools, and caldera features at hydrothermal seeps in the Salton Sea Geothermal Field, southern California, *Geomorphology*, *130*(3–4), 327–342.

Pappalardo, R. T., and A. C. Barr (2004), The origin of domes on Europa: The role of thermally induced compositional diapirism, *Geophysical Research Letters*, *31*, L01,701.

Pappalardo, R. T., J. W. Head, R. Greeley, R. J. Sullivan, C. Pilcher, G. Schubert, W. B. Moore, M. H. Carr, J. M. Moore, M. J. S. Belton, and D. L. Goldsby (1998), Geological evidence for solid-state convection in Europa's ice shell, *Nature*, *391*, 365–368.

Paterson, W. (1994), *The Physics of Glaciers*, 3 ed., Butterworth Heinemann.

Phillips, C. B., A. S. McEwen, G. V. Hoppa, S. A. Fagents, R. Greeley, J. E. Klemaszewski, R. T. Pappalardo, K. P. Klaasen, and H. H. Breneman (2000), The search for current geologic activity on Europa, *J. Geophys. Res.*, *105*(E9), 22,579–22,597.

Plafker, G., G. E. Ericksen, and J. Fernández Concha (1971), Geological aspects of the May 31, 1970, Perú earthquake, *Bulletin of the Seismological Society of America*, *61*(3), 543–578.

Pliny (79), *Naturalis Historia*, H. G. Bohn, London.

Porco, C. C., P. Helfenstein, P. C. Thomas, A. P. Ingersoll, J. Wisdom, R. West, G. Neukum, T. Denk, R. Wagner, T. Roatsch, S. Kieffer, E. Turtle, A. McEwen, T. V. Johnson, J. Rathbun, J. Veverka, D. Wilson, J. Perry, J. Spitale, A. Brahic, J. A. Burns, A. D. Del Genio, L. Dones, C. D. Murray, and S. Squyres (2006), Cassini Observes the Active South Pole of Enceladus, *Science*, *311*(5), 1393–1401.

Postberg, F., S. Kempf, J. Schmidt, N. Brilliantov, A. Beinsen, B. Abel, U. Buck, and R. Srama (2009), Sodium salts in E-ring ice grains from an ocean below the surface of Enceladus, *Nature*, *459*(7250), 1098–1101.

Pridmore, C., S. Brandenburg, T. McCrink, R. Sickler, J. Stewart, and J. Tinsley (2010), Liquefaction and related ground failures in Imperial County, California, caused by the April 4, 2010 El Mayor-Cucapah earthquake, in *Conference*, Cordilleran Section - 106th Annual Meeting, and Pacific Section, American Association of Petroleum Geologists.

Prockter, L., and P. Schenk (2005), Origin and evolution of Castalia Macula, an anomalous young depression on Europa, *Icarus*, *177*, 305–326.

Qin, R., W. R. Buck, and L. Germanovich (2007), Comment on "Mechanics of tidally driven fractures in Europa's ice shell" by S. Lee, R.T. Pappalardo, and N.C. Makris [2005. Icarus 177, 367–379], *Icarus*, *189*(2), 595–597.

Randall, W. (1974), An analysis of the subsurface structure and stratigraphy of the Salton Sea Geothermal Anomaly, Imperial Valley, California, Ph.D. thesis, University of California, Riverside.

Rathbun, J. A., G. S. Musser Jr, and S. W. Squyres (1998), Ice diapirs on Europa: Implications for liquid water, *Geophys. Res. Lett*, *25*(22), 4157–4160.

Richards, J. R. (2011), Report into the Past, Present, and Future Social Impacts of Lumpur Sidoarjo, *Tech. rep.*, Humanitus Sidoarjo Fund.

Rinehart, J. S. (1972), Fluctuations in Geyser Activity Caused by Variations in Earth Tidal Forces, Barometric Pressure, and Tectonic Stresses, *J. Geophys. Res.*, *77*(2), 342–350.

Roberts, J. H., and F. Nimmo (2008), Tidal heating and the long-term stability of a subsurface ocean on Enceladus, *Icarus*, *194*(2), 675–689.

Roberts, K. S., R. J. Davies, S. A. Stewart, and M. Tingay (2011), Structural controls on mud volcano vent distributions: examples from Azerbaijan and Lusi, East Java, *Journal of the Geological Society*, *168*(4), 1013–1030.

Roberts, P. M., and A. I. Abdel-Fattah (2009), Seismic stress stimulation mobilizes colloids trapped in a porous rock, *Earth and Planetary Science Letters*, *284*(3–4), 538–543.

Robinson, P., W. Elders, and L. Muffler (1976), Quaternary volcanism in the Salton Sea geothermal field, Imperial Valley, California, *Geological Society of America Bulletin*, *87*, 347–360.

Roeloffs, E. (1996), Poroelastic techniques in the study of earthquake-related hydrologic phenomena, *Advances in Geophysics*, *37*, 136–195.

Rojstaczer, S., and S. Wolf (1992), Permeability changes associated with large earthquakes: An example from Loma Prieta, California, *Geology*, *20*(3), 211–214.

Rojstaczer, S., S. Wolf, and R. Michel (1995), Permeability enhancement in the shallow crust as a cause of earthquake-induced hydrological changes, *Nature*, *373*, 237–239.

Rudolph, M., and M. Manga (2009a), Ocean pressurization, stress evolution, and tensile fracture within icy moons, in *Lunar and Planetary Institute Science Conference Abstracts*, p. 2436.

Rudolph, M. L., and M. Manga (2009b), Fracture penetration in planetary ice shells, *Icarus*, *199*(2), 536–541.

Rudolph, M. L., and M. Manga (2010), Mud volcano response to the 4 April 2010 El Mayor-Cucapah earthquake, *J. Geophys. Res.*, *115*(B12), B12,211.

Rudolph, M. L., and M. Manga (2012), Frequency dependence of mud volcano response to earthquakes, *Geophys. Res. Lett*, *39*(14), L14,303.

Rudolph, M. L., L. Karlstrom, and M. Manga (2011), A prediction of the longevity of the Lusi mud eruption, Indonesia, *Earth and Planetary Science Letters*, *308*(1-2), 124–130.

Ruiz, J. (2010), Equilibrium Convection on a Tidally Heated and Stressed Icy Shell of Europa for a Composite Water Ice Rheology, *Earth, Moon, and Planets*, *107*(2-4), 157–167.

Ruiz, J., and R. Tejero (2003), Heat flow, lenticulae spacing, and possibility of convection in the ice shell of europa, *Icarus*, *162*(2), 362–373.

Ruiz, J., J. A. Alvarez-Gómez, R. Tejero, and N. Sánchez (2007), Heat flow and thickness of a convective ice shell on Europa for grain size-dependent rheologies, *Icarus*, *190*(1), 145–154.

Saar, M. O., M. Manga, K. V. Cashman, and S. Fremouw (2001), Numerical models of the onset of yield strength in crystal–melt suspensions, *Earth and Planetary Science Letters*, *187*(3-4), 367–379.

Sahagian, D. L., and A. A. Proussevitch (1992), Bubbles in volcanic systems, *Nature*, *359*(6395), 485–485.

Sandwell, D., P. Rosen, W. Moore, and E. Gurrola (2004), Radar interferometry for measuring tidal strain across cracks on Europa, *Journal of Geophysical Research (Planets)*, p. E11003.

Sawolo, N., E. Sutriono, B. P. Istadi, and A. B. Darmoyo (2009), The LUSI mud volcano triggering controversy: Was it caused by drilling?, *Marine and Petroleum Geology*, *26*(9), 1766–1784.

Schenk, P., I. Matsuyama, and F. Nimmo (2008), True polar wander on Europa from global-scale small-circle depressions, *Nature*, *453*, 368–371.

Schenk, P. M., and R. T. Pappalardo (2004), Topographic variations in chaos on Europa: Implications for diapiric formation, *Geophys. Res. Lett*, *31*(16), L16,703–.

Schubert, G., J. D. Anderson, B. J. Travis, and J. Palguta (2007), Enceladus: Present internal structure and differentiation by early and long-term radiogenic heating, *Icarus*, *188*(2), 345–355.

Schulson, E. M. (2001), Brittle failure of ice, *Engineering Fracture Mechanics*, *68*(17-18), 1839–1887.

Schulson, E. M. (2006), The fracture of water ice Ih: A short overview, *Meteoritics and Planetary Science*, *41*, 1497–1508.

Seiferlin, K., N. I. Kömle, G. Kargl, and T. Spohn (1996), Line heat-source measurements of the thermal conductivity of porous H2O ice, CO2 ice and mineral powders under space conditions, *Planetary and Space Science*, *44*(7), 691–704.

Shapiro, S. S., M. B. Wilk, and H. J. Chen (1968), A Comparative Study of Various Tests for Normality, *Journal of the American Statistical Association*, *63*(324), 1343–1372.

Showman, A. P., and L. Han (2004), Numerical simulations of convection in Europa's ice shell: Implications for surface features, *J. Geophys. Res.*, *109*(E01010).

Showman, A. P., and L. Han (2005), Effects of plasticity on convection in an ice shell: Implications for Europa, *Icarus*, *177*(2), 425–437.

Silver, P. G., and N. J. Valette-Silver (1992), Detection of Hydrothermal Precursors to Large Northern California Earthquakes, *Science*, *257*(5075), 1363–1368.

Solomatov, V. (1995), Scaling of temperature- and stress-dependent viscosity convection, *Phys Fluids*, *7*(2), 266–274.

Solomatov, V. S., and L. N. Moresi (2000), Scaling of time-dependent stagnant lid convection: Application to small-scale convection on Earth and other terrestrial planets, *Journal of Geophysical Research*, *105*(B), 21,795–21,818.

Sotin, C., J. Head III, and G. Tobie (2002), Europa- Tidal heating of upwelling thermal plumes and the origin of lenticulae and chaos melting, *Geophysical Research Letters*, *29*(8), 74.

Spencer, J. R., L. K. Tamppari, T. Z. Martin, and L. D. Travis (1999), Temperatures on Europa from Galileo PPR: Nighttime Thermal Anomalies, *Science*, *284*, 1514–1516.

Steinberg, G., and A. Merzhanov (1981), *Geyser process: its theory, modeling, and field experiment. Part 1. Theory of the geyser process*, Modern Geology.

Steinberg, G., A. Merzhanov, and A. Steinberg (1982), Geyser process: its theory, modeling, and field experiment. Part 4. On seismic influence on geyser regime, *Modern Geology*, *8*, 79–86.

Steinberg, G., A. Steinberg, and A. Merzhanov (1989), Fluid mechanism of pressure growth in volcanic (magmatic) systems, *Modern Geology*, *13*, 257–266.

Sturtevant, B., H. Kanamori, and E. E. Brodsky (1996), Seismic triggering by rectified diffusion in geothermal systems, *Journal of Geophysical Research*, *101*, 25,269–25,282.

Sturz, A., R. Kamps, and P. Earley (1992), Temporal changes in mud volcanos, Salton Sea Geothermal Area, in *Water-Rock Interactions*, edited by Y. K. Kharaka and A. S. Maest, pp. 1363–1366, A.A. Balkema, Brookfield, VT.

Sumita, I., and M. Manga (2008), Suspension rheology under oscillatory shear and its geophysical implications, *Earth and Planetary Science Letters*, *269*(3-4), 468–477.

Sutrisna, E. (2009), "Can LUSI be stopped? - A case study and lessons learned from the relief wells", *AGU Fall Meeting Abstracts*, p. A1053.

Svensen, H., D. Karlsen, A. Sturz, K. Backer-Owe, D. Banks, and S. Planke (2007), Processes controlling water and hydrocarbon composition in seeps from the Salton Sea geothermal system, California, USA, *Geology*, *35*(1), 85–88.

Svensen, H., Ø. Hammer, A. Mazzini, N. Onderdonk, S. Polteau, S. Planke, and Y. Podladchikov (2009), Dynamics of hydrothermal seeps from the Salton Sea geothermal system (California, USA) constrained by temperature monitoring and time series analysis, *Journal of Geophysical Research*, *B09201*.

Tanikawa, W., M. Sakaguchi, H. T. Wibowo, T. Shimamoto, and O. Tadai (2010), Fluid transport properties and estimation of overpressure at the Lusi mud volcano, East Java Basin, *Engineering Geology*, *116*(1-2), 73–85.

Taylor, G. I. (1938), Plastic strain in metals, *J. Inst. Metals*, *62*, 307.

Taylor, R. L. (2011), *FEAP: A Finite Element Analysis Program*.

Thorsteinsson, T. (2002), Fabric development with nearest-neighbor interaction and dynamic recrystallization, *Journal of Geophysical Research (Solid Earth)*, *107*(B), 2014.

Tingay, M., O. Heidbach, R. Davies, and R. Swarbrick (2008), Triggering of the Lusi mud eruption: Earthquake versus drilling initiation, *Geology*, *36*(8), 639–642.

Tobie, G., G. Choblet, and C. Sotin (2003), Tidally heated convection: Constraints on Europa's ice shell thickness, *Journal of Geophysical Research*, *108*(E11), 5124.

Toda, S., R. S. Stein, K. Richards-Dinger, and S. Bozkurt (2005), Forecasting the evolution of seismicity in southern California: Animations built on earthquake stress transfer, *Journal of Geophysical Research*, *110*(B05S16).

Townley, S., and M. Allen (1939), Descriptive catalog of Earthquakes of the Pacific Coast of the United States 1769 to 1928, *Bulletin of the Seismological Society of America*, *29*(1), 1–297.

Travis, B. J., J. Palguta, and G. Schubert (2012), A whole-moon thermal history model of Europa: Impact of hydrothermal circulation and salt transport, *Icarus*, *218*(2), 1006–1019.

Treiman, J., M. Rymer, K. Kendrick, J. Lienkaemper, R. I. Weldon, J. Hernandez, P. Irvine, N. Knepprath, B. Olson, and R. Sickler (2010), TRIGGERED SLIP IN SOUTHERN CALIFORNIA AS A RESULT OF THE APRIL 5, 2010 EL MAYOR-CUCAPAH EARTHQUAKE, in *Proceedings*, Cordilleran Section - 106th Annual Meeting, and Pacific Section, American Association of Petroleum Geologists.

Turcotte, D. L., and G. Schubert (2002), *Geodynamics*, 2 ed., Cambridge University Press, New York.

Wagner, W., J. R. Cooper, A. Dittmann, J. Kijima, H. J. Kretzschmar, A. Kruse, R. Mareš, K. Oguchi, H. Sato, I. Stöcker, O. Šifner, Y. Takaishi, I. Tanishita, J. Trübenbach, and T. Willkommen (2000), The IAPWS Industrial Formulation 1997 for the Thermodynamic Properties of Water and Steam, *Journal of Engineering for Gas Turbines and Power*, *122*(1), 150–184.

Walter, T. R., and F. Amelung (2007), Volcanic eruptions following M 9 megathrust earthquakes: Implications for the Sumatra-Andaman volcanoes, *Geology*, *35*, 539.

Wang, C.-Y. (2007), Liquefaction beyond the Near Field, *Seismological Research Letters*, *78*(5), 512–517.

Wang, C.-Y., and M. Manga (2010), Hydrologic responses to earthquakes and a general metric, *Geofluids*, *10*(1-2), 206–216.

Wang, C.-Y., L.-H. Cheng, C.-V. Chin, and S.-B. Yu (2001), Coseismic hydrologic response of an alluvial fan to the 1999 Chi-Chi earthquake, Taiwan, *Geology*, *29*(9), 831–834.

Wang, C.-Y., D. S. Dreger, C.-H. Wang, D. Mayeri, and J. G. Berryman (2003), Field relations among coseismic ground motion, water level change and liquefaction for the 1999 Chi-Chi (Mw = 7.5) earthquake, Taiwan, *Geophysical Research Letters*, *30*(1), 1.

Wang, C.-Y., M. Manga, D. Dreger, and A. Wong (2004a), Streamflow increase due to rupturing of hydrothermal reservoirs: Evidence from the 2003 San Simeon, California, Earthquake, *Geophysical Research Letters*, *31*, 10,502.

Wang, C.-Y., C.-H. Wang, and M. Manga (2004b), Coseismic release of water from mountains: Evidence from the 1999 (Mw = 7.5) Chi-Chi, Taiwan, earthquake, *Geology*, *32*(9), 769–772.

Wang, H. (2000), *Theory of linear poroelasticity: with applications to geomechanics and hydrogeology*, Princeton series in geophysics, Princeton University Press.

Wells, D. L., and K. J. Coppersmith (1994), New empirical relationships among magnitude, rupture length, rupture width, rupture area, and surface displacement, *Bulletin of the Seismological Society of America*, *84*(4), 974–1002.

Williams, A. E., and M. A. McKibben (1989), A brine interface in the Salton Sea Geothermal System, California: Fluid geochemical and isotopic characteristics, *Geochimica et Cosmochimica Acta*, *53*(8), 1905–1920.

Wong, A., and C.-Y. Wang (2007), Field relations between the spectral composition of ground motion and hydrological effects during the 1999 Chi-Chi (Taiwan) earthquake, *J. Geophys. Res.*, *112*(B10), B10,305.

Woods, A. W., and H. E. Huppert (2003), On magma chamber evolution during slow effusive eruptions, *J. Geophys. Res.*, *108*(B8), 2403.

Youd, T., B. HAJ, and J. Proctor (2004), GEOTECHNICAL LOGS AND DATA FROM PERMANENTLY INSTRUMENTED FIELD SITES: GARNER VALLEY DOWN HOLE ARRAY(GVDA) AND WILDLIFE LIQUEFACTION ARRAY (WLA), *Tech. rep.*, The Network for Earthquake Engineering Simulation (NEES) Colaboratories.

Younker, L. W., P. W. Kasameyer, and J. D. Tewhey (1982), Geological, geophysical, and thermal characteristics of the Salton Sea Geothermal Field, California, *Journal of Volcanology and Geothermal Research*, *12*(3-4), 221–258.

Zienkiewicz, O., and R. Taylor (2005), *The finite element method: its basis and fundamentals*, 6 ed., Elsevier Butterworth-Heinemann.

Zoporowski, A., and S. A. Miller (2009), Modelling eruption cycles and decay of mud volcanoes, *Marine and Petroleum Geology*, *26*(9), 1879–1887.